博士論文

論文題目　**Imaging intraorganellar Ca^{2+} dynamics at subcellular resolution using genetically encoded fluorescent Ca^{2+} indicators**

（タンパク質型 Ca^{2+} インジケーターを用いた細胞小器官 Ca^{2+} 動態の可視化と機能解析）

氏名　鈴木　純二

Imaging intraorganellar Ca^{2+} dynamics at subcellular resolution using genetically encoded fluorescent Ca^{2+} indicators

（タンパク質型 Ca^{2+}インジケーターを用いた細胞小器官 Ca^{2+}動態の可視化と機能解析）

東京大学大学院医学系研究科　機能生物学専攻

細胞分子薬理学

鈴木　純二

Contents

Summary

The endoplasmic reticulum (ER) and mitochondria accumulate Ca^{2+} within their lumens to regulate numerous cell functions. However, determining the dynamics of intraorganellar Ca^{2+} has proven to be difficult. Here, I describe a family of genetically-encoded Ca^{2+} indicators, named calcium-measuring organelle-entrapped protein indicators (CEPIA), which can be utilized for intra-organellar Ca^{2+} imaging. CEPIA, which emit green, red or blue/green fluorescence, are engineered to bind Ca^{2+} at intra-organellar Ca^{2+} concentrations. They can be targeted to different organelles and may be used alongside other fluorescent molecular markers, expanding the range of cell functions that can be simultaneously analyzed. The spatiotemporal resolution of CEPIA makes it possible to resolve Ca^{2+} import into individual mitochondria while simultaneously measuring ER and cytosolic Ca^{2+}. These imaging capabilities were used to reveal differential Ca^{2+} handling in individual mitochondria. CEPIA imaging is a useful new tool to further the understanding of organellar functions.

Introduction

Ca^{2+} is an important second messenger that regulates numerous cellular functions including contraction, fertilization, proliferation and synaptic plasticity (1). The versatility of Ca^{2+} signals principally relies on the capacity of various types of cells to control spatiotemporal distribution of cytosolic Ca^{2+} levels to fit their physiology (2). In the resting state, Ca^{2+} concentration in the cytosol is kept below 100 nM, which is three to four orders of magnitude lower than that in the extracellular space or intracellular Ca^{2+} stores. In response to Ca^{2+}-mobilizing stimulation, the cytosolic Ca^{2+} concentration rises up to 1000 nM or higher and may fluctuate in a time dependent manner. Cytosolic Ca^{2+} signals are generated by two distinct pathways; Ca^{2+} influx from the extracellular space and Ca^{2+} release from the intracellular Ca^{2+} store, and there is a complex crosstalk between these two pathways. Furthermore, in response to cytosolic Ca^{2+} signaling, Ca^{2+} concentrations in the intracellular organelles such as mitochondria and nuclei also increase (3,4). To understand these complex signaling processes, optical Ca^{2+} imaging using Ca^{2+} indicators, which alter their spectral properties depending on their surrounding Ca^{2+} concentration, is a powerful and useful method. Indeed, optical Ca^{2+} imaging techniques have been successfully used to decipher spatiotemporal dynamics and physiological functions of cytosolic Ca^{2+} signals in cells in culture, in ex vivo samples and in living animals (5). In contrast to the success of cytosolic Ca^{2+} imaging techniques, there are several limitations in the existing methods available for

monitoring Ca^{2+} dynamics in the organelles such as the endoplasmic reticulum (ER) and mitochondria.

The ER and mitochondria are membrane-bound intracellular organelles in eukaryotic cells that carry out vital functions. Both ER and mitochondrial membranes display Ca^{2+}-transporting molecules whose function is to import Ca^{2+} into the lumen against the concentration gradient. This uphill Ca^{2+} transport is mediated in the ER membrane by sarco(endo)plasmic reticulum Ca^{2+} ATPase (SERCA) (6) and in the inner mitochondrial membrane by the mitochondrial Ca^{2+} uniporter (MCU) (3). The organellar membranes also feature molecules that allow Ca^{2+} to exit from the organelles to the cytosol: inositol 1,4,5-trisphosphate receptor (IP_3R) and ryanodine receptor (RyR) in the ER, and the Na^+/Ca^{2+} and H^+/Ca^{2+} exchanger in mitochondria (3,7). Thus, the intraluminal Ca^{2+} concentration in the organelles is tightly regulated, and may exceed that of cytosol by a large factor. Ca^{2+} levels within the ER profoundly affect organelle functions, and overload or depletion causes ER stress (8). Within the mitochondrial matrix, Ca^{2+} concentration regulates the rate of ATP production, and abnormal concentrations can lead to cell death or autophagic degradation of the mitochondria (3).

ER and mitochondrial structures are constantly being reorganized and close contacts form between the two types of organelles. These contact sites have recently been shown to be involved in diverse functions, including lipid biosynthesis, mitochondrial biogenesis and the transfer of Ca^{2+} (9-12). Both types of organelle are also involved in the regulation of cytosolic

Ca^{2+} concentration. Release of Ca^{2+} from the ER regulates contraction, fertilization, development, secretion, and synaptic plasticity (7). In addition, the ER luminal Ca^{2+} concentration regulates Ca^{2+} influx across the plasma membrane. Following a release of Ca^{2+} from the ER, stromal interaction molecule 1 (STIM1), which is present in the ER membrane, functions as a Ca^{2+} transducer; it signals to the plasma membrane to activate the store-operated Ca^{2+} entry mechanism (SOCE) (13,14). SOCE is mediated by the molecular complex that includes Orai1, a Ca^{2+} channel on the plasma membrane, and is important for the activation of various cell functions, the best-studied example of which is the immune responses (13). In contrast to the active role of the ER in Ca^{2+} signaling, mitochondria have been considered to act as a passive Ca^{2+} buffer (3). However, recent results suggest that they may also have an active role as a source of Ca^{2+} in the regulation of cytosolic Ca^{2+} concentration (15).

Although the importance of the ER and mitochondria as Ca^{2+}-handling organelles is unequivocal, the mechanism by which organellar Ca^{2+} concentrations regulate cellular processes remains elusive. New methods to dissect organellar Ca^{2+} dynamics are expected to facilitate such studies. While small molecular Ca^{2+} indicators cannot be precisely targeted to the organelles, limiting their use in living cells, genetically-encoded Ca^{2+} indicators (GECIs) can be targeted to organelles with the addition of appropriate tags (16). Making use of this capability, GFP-based GECIs (10,11,15,17-48) and aequorin (a Ca^{2+}-sensitive photoprotein) (49) have been used to measure intraorganellar Ca^{2+} concentrations. FRET-type GFP-based

GECIs were first used to measure intraluminal Ca^{2+} concentration in the ER and were applied to different cell types (15,17,22,23,25-28,30-32,36,47,48). This type of indicators uses wide visible wavelength bands for excitation and emission, often limiting the simultaneous use of other fluorescent molecules (50,51). Subsequently, innovative modifications of the GFP molecule have yielded single-wavelength-excitation GECIs with various affinities to Ca^{2+} for ER and mitochondrial Ca^{2+} imaging (18-21,24,33-35,39,41,42,45,46). Aequorin emits dim light, and simultaneous measurement with brighter fluorescence signals is not possible with most fluorescence microscopes. Although there are a wide variety of indicators, simultaneous Ca^{2+} imaging of the ER and mitochondria has not been carried out, and improvement in the spatiotemporal resolution of organellar Ca^{2+} is expected to enhance our understanding of intraorganellar Ca^{2+} dynamics. For these reasons, and to study the functional interaction between the ER and mitochondria, a new type of GECIs with higher spatiotemporal resolution was required.

This study reports on the generation of new organellar Ca^{2+} indicators that allow simultaneous imaging of two subcellular compartments with high spatiotemporal resolution. They are optimized in terms of Ca^{2+} affinity and dynamic range for organellar Ca^{2+} imaging and come in color variants for simultaneous measurement of multiple signals when they are used in appropriate combinations. Using them, intraorganellar Ca^{2+} concentrations can be imaged at unprecedented spatiotemporal resolution. To illustrate the utility of the approach, I demonstrate high spatiotemporal resolution imaging of ER and mitochondrial Ca^{2+} dynamics

in living cells; I show the quantitative relationship between the ER Ca^{2+} concentration and the extent of STIM1 puncta formation in the regulation of SOCE; and I show that inhomogeneity in mitochondrial Ca^{2+} responses can be observed during apparently homogenous ER and cytosolic Ca^{2+} changes, which suggests that there is a mechanism to regulate the influx of Ca^{2+} into mitochondria. The new indicators described in this work will be valuable for further study of the roles of the ER and mitochondria, and of their functional interactions.

Materials and Methods

Gene construction

For creating a CEPIA library, cfGCaMP2 (GCaMP2 with amino acid substitutions of M36L in CaM, and N105Y and E124V in circular permutated enhanced GFP (cpEGFP)) with ER retention signal sequence (SEKDEL) was cloned into a bacterial expression vector, pET19b (Novagen, USA), using primers 1 and 2 (Table 3). G-GECO1.1, R-GECO1 and GEM-GECO1 were also cloned into pET19b using primers 3 and 4. The CaM sequences in cfGCaMP2 variants were replaced with those in G-GECO1.1, R-GECO1 or GEM-GECO1 using primers 4–7. Site-directed mutagenesis was performed by PCR using primers 8–36.

For mammalian expression of CEPIA variants in the ER and mitochondria, CEPIA variants were cloned into pCMV/myc/ER and pCMV/myc/mito vector (Invitrogen, USA) using primers 3, 4 and 37–39. For mitochondrial Ca^{2+} imaging, the specificity of mitochondrial localization was enhanced by attaching the mitochondria targeting sequences in tandem (29) to CEPIA2–4*mt*, R-GECO1*mt* and GEM-GECO1*mt* using primers 40–47. To enhance protein expression, GEM-CEPIA1*er* was cloned into the CAG promoter-containing vector, pCIS, using primers 48 and 49. To express G-CEPIA1*er* in the Purkinje cells, G-CEPIA1*er* was cloned into pSinRep5 (Invitrogen) using primers 50–53. To localize EGFP and mCherry in the ER, EGFP and mCherry were cloned into the pcDNA3 D1ER (23) to attach calreticulin signal sequence and ER retention signal (KDEL) using primers 54–59. To

construct EYFP-*er*, EYFP was cloned from pcDNA3-YC4er (17) into pCMV/myc/ER vector using primers 60 and 61. To construct SypHer-dmito, an amino acid substitution of C199S (52) was added in pHyper-dmito (Evrogen, Russia) using primers 62 and 63. To construct mCherry-STIM1, STIM1 was cloned from pApuro-GFP-STIM1 (53) into pShuttle2 vector using primers 60 and 64–66.

Bacterial expression and in vitro spectroscopy

BL21-CodonPlus(DE3)-RIL bacteria (Stratagene, USA) was transformed with the plasmids and incubated for 16–36 h at 37°C in 2×YT medium containing ampicillin and chloramphenicol (20 μg ml^{-1}). The cells were resuspended in KCl/MOPS buffer (130 mM KCl, 50 mM MOPS, pH 7.2). After cell lysis with sonication, recombinant proteins were purified using TALON metal affinity resin (Clontech, USA) and dialyzed with Slide-A-Lyzer Dialysis Cassettes, 10K MWCO (Thermo Fisher Scientific, USA).

Ca^{2+} and Mg^{2+} titration curves of CEPIA variants were obtained by adding small aliquots of $CaCl_2$ or $MgCl_2$ to the recombinant indicators in a KCl/MOPS buffer containing 0 or 1 mM EGTA at pH 7.2. The Ca^{2+} concentration carried over from the recombinant protein samples was estimated as 2 μM. In the presence of 1 mM EGTA, the $[Ca^{2+}]_{free}$ at pH 7.2 was calculated as follows:

$$[Ca^{2+}]_{free} = [D + (4 \times K_d \times [Ca^{2+}]_{total} + D^2)^{1/2}] / 2,$$

$$D = [Ca^{2+}]_{total} - [EGTA]_{total} - K_d,$$

$$K_d = [EGTA]_{free} \times [Ca^{2+}]_{free} / [CaEGTA] = 150.5 \text{ nM},$$

where K_d is the dissociation constant of CaEGTA (54). To estimate properties of CEPIA variants in mitochondria, titration experiments were performed in a KCl/HEPES buffer at pH 8.0 to mimic the mitochondrial environment (55), containing 1 mM BAPTA assuming a K_d of 0.1 μM. Fluorescence intensity was measured with a spectrofluorometer (FP-750, Jasco, Japan) for each protein at excitation/emission wavelength; 488/512 nm for cfGCaMP2 and G-GECO1.1 variants, 562/584 nm for R-GECO1 variants, and 395/460 nm and 395/510 nm for GEM-GECO1 variants. The obtained Ca^{2+}-fluorescence intensity relationships were fitted by the following Hill equations using a least-square method in the Kaleidagraph software (Synergy Software, USA). For cfGCaMP2, G-GECO1.1 and R-GECO1 variants,

$$F = F_{min} + (F_{max} - F_{min}) \times ([Ca^{2+}]_{free})^n / [([Ca^{2+}]_{free})^n + (K_d)^n].$$

For GEM-GECO1 variants,

$$R = R_{min} + (R_{max} - R_{min}) \times ([Ca^{2+}]_{free})^n / [([Ca^{2+}]_{free})^n + (K_d)^n],$$

where R = (F at 460 nm) / (F at 510 nm). K_d represents an apparent dissociation constant, or the Ca^{2+} concentration at which half of the indicator molecules bind to Ca^{2+}. n represents Hill coefficient. The dynamic range of the indicator was calculated as the ratio of maximum and minimum fluorescence intensity or ratio (F_{max}/F_{min} or R_{max}/R_{min}). Fluorescence intensity at various Ca^{2+} concentrations was standardized by the following equation:

$$\theta = (F - F_{min}) / (F_{max} - F_{min}) \text{ or } (R - R_{min}) / (R_{max} - R_{min}).$$

The absorbance spectra were measured with a spectrophotometer (DU-640 UV/VIS, Beckman, USA). To determine the molar extinction coefficient (ε), absorbance spectrum was measured first for each protein in KCl/MOPS buffer with or without 5 mM $CaCl_2$. The extinction coefficient was calculated by dividing the peak absorbance by protein concentration. The protein concentrations for G-CEPIA1*er*, GEM-CEPIA1*er*, G-GECO1.1 and GEM-GECO1 were calculated by measuring the absorbance following alkaline denaturation, assuming ε = 44,000 M^{-1} cm^{-1} at 446 nm. For R-CEPIA1*er* and R-GECO1, ε = 38,000 M^{-1} cm^{-1} at 455 nm (24). Quantum yields (Φ) of CEPIA*er* were calculated by using G-GECO1.1, R-GECO1 and GEM-GECO1 as standards (24).

Animal experiments

All animal experiments were carried out in accordance with the regulations and guidelines for Institutional Animal Care and Use Committee at the University of Tokyo and were approved by the institutional review committees of the Graduate School of Medicine, the University of Tokyo.

Cell culture

HeLa cells, HEK293A cells, BHK cells and astrocytes were cultured on collagen-coated dishes in DMEM supplemented with 10% fetal bovine serum, penicillin (100 U ml^{-1}) and streptomycin (100 U ml^{-1}). Jurkat T cells (E6-1) were maintained in RPMI medium (Gibco,

USA) supplemented with 10% fetal bovine serum. An astrocytic culture with >95% purity was prepared by several replatings of the brain cell culture which was obtained by 2.5% trypsin treatment and gentle trituration of the neocortices or the hippocampi of embryonic day 18–19 or postnatal day 1–3 Sprague–Dawley rat fetuses (56). For Ca^{2+} imaging, the cells were plated on collagen type-I-coated glass-bottom dishes (MatTek, USA) or Cell-Tak-coated dishes (Corning, USA) before imaging.

Time-lapse Ca^{2+} imaging

Cultured cells were transfected using Lipofectamine 2000 (Invitrogen) two or three days before imaging. Jurkat T cells were electroporated using a MicroPorator (MP-100, Digital Bio, Korea) one day before imaging. For cytosolic Ca^{2+} imaging using fura-2, cells were loaded with 5 μM fura-2 AM (Molecular Probes, USA) at room temperature (RT; 22–24°C) for 40–60 min in 0.1% BSA-supplemented physiological salt solution (PSS) containing (in mM) 150 NaCl, 4 KCl, 2 $CaCl_2$, 1 $MgCl_2$, 5.6 glucose, and 25 HEPES (pH 7.4). Prior to imaging, the loading solution was replaced with PSS without BSA. The images were captured using an inverted microscope (IX81, Olympus, Japan) equipped with a 20× objective (numerical aperture (NA) = 0.75, UPlanSApo, Olympus) or a 40× objective (NA 0.90, UApo/340, Olympus), an electron multiplying cooled-coupled device (EM-CCD) camera (ImagEM, Hamamatsu photonics, Japan), a filter wheel (Lambda 10-3, Sutter Instrument, USA), a xenon lamp (ebx75) and a metal halide lamp (EL6000, Leica, Germany) at a rate of one frame per 2

or 3 s with the following excitation/emission filter settings: 472 ± 15 nm/520 ± 17.5 nm for CEPIA1*er*, G-CEPIA1*er*, CEPIA2–4*mt*, EYFP-*er* and G-GECO1.1, ; 562 ± 20 nm/641 ± 37.5 nm for R-CEPIA1*er*, R-GECO1 and mCherry-STIM1; 377 ± 25 nm/466 ± 20 nm and 377 ± 25 nm/520 ± 17.5 nm for GEM-CEPIA1*er* and GEM-GECO1; 340 ± 13 nm/510 ± 42 nm and 365 ± 6 nm/510 ± 42 nm for fura-2; 440 ± 10.5 nm/480 ± 15 nm and 440 ± 10.5 nm/535 ± 13 nm for D1ER (23,24). For analysis of the ratiometric indicators, the fluorescence ratio (F_{466}/F_{520} for GEM-GECO1 and GEM-CEPIA1*er*; F_{340}/F_{365} for fura-2; F_{535}/F_{480} for D1ER) was calculated. Photobleaching was corrected for using a linear fit to the fluorescence intensity change before agonist stimulation. All images were analyzed with ImageJ software.

To image subcellular ER Ca^{2+} dynamics during agonist-induced Ca^{2+} wave formation, HeLa cells expressing either G-CEPIA1*er* or R-CEPIA1*er* were used. Images were captured at a rate of one frame per 30–100 ms using a 60× objective (NA 1.45, PlanApo TIRF, Olympus) and the metal halide lamp or an LED lamp (pE-100, CoolLED, UK). To evaluate Ca^{2+} wave velocity in the ER and cytosol, images were normalized by the resting intensity, and a linear region of interest (ROI) was defined along the direction of wave propagation. A line-scan image was created by averaging 30 adjacent linear ROIs parallel to the original ROI, and time derivative was obtained to detect the time point which showed maximal change during the scan duration. Then the time points were plotted against the pixel, and the wave velocity was estimated by the slope of the least-squares regression line.

For mitochondrial Ca^{2+} imaging with ER and cytosolic Ca^{2+}, mitochondrial inner membrane potential or mitochondrial pH at subcellular resolution, HeLa cells were imaged with a confocal microscope (TCS SP8, Leica) equipped with a 63× objective (NA 1.40, HC PL APO, Leica) at a rate of one frame per 2 or 3 s with the following excitation/emission spectra: R-GECO1*mt* (552 nm/560– nm), G-CEPIA1*er* (488 nm/500–550 nm) and GEM-GECO1 (405 nm/500–550 nm); GEM-GECO1*mt* (405 nm/500–550 nm) and JC-1 (488 nm/500–550 nm and 488 nm/560– nm); R-GECO1*mt* (552 nm/560– nm) and SypHer-dmito (405 nm/500–550 nm and 488 nm/500–550 nm). For analysis of JC-1 and SypHer-dmito, the fluorescence ratio (488 nm/560– nm over 488 nm/500–550 nm for JC-1 (57); 488 nm/500–550 nm over 405 nm/500–550 nm for SypHer-dmito (52)) was calculated.

To perform in situ Ca^{2+} titration of CEPIA, the plasma membrane of HeLa cells was permeabilized with 150 μM β-escin (Nacalai Tesque, Japan) in a solution containing (in mM) 140 KCl, 10 NaCl, 1 $MgCl_2$ and 20 HEPES (pH 7.2). After 4 min treatment with β-escin, various Ca^{2+} concentrations were applied in the presence of 3 μM ionomycin and 3 μM thapsigargin, and estimated the maximum and minimum fluorescent intensity (R_{max} and R_{min}), dynamic range (R_{max} / R_{min}), K_d and n.

For the estimation of $[Ca^{2+}]_{ER}$ based on the ratiometric measurement using GEM-CEPIA1*er* (Figures 7c, 7d, 12f and 16), $[Ca^{2+}]_{ER}$ was obtained by the following equation:

$$[Ca^{2+}]_{free} = [(R - R_{min}) / (R_{max} - R)]^{1/n} \times K_d,$$

where R = (F at 466 nm)/(F at 510 nm), n = 1.37 and K_d = 558 μM.

To evaluate pH dynamics in the ER (Figures 9a–d), HeLa cells expressing EYFP-*er* were first stimulated with histamine. Subsequently the cells were stimulated in a PSS (adjusted to pH 6.8) containing monensin (10 μM, Wako, Japan) and nigericin (10 μM, Wako). Then, the cells were alkalinized with a solution containing (in mM) 120 NaCl, 30 NH_4Cl, 4 KCl, 2 $CaCl_2$, 1 $MgCl_2$, 5 HEPES and 5.6 Glucose (pH 7.4) (58).

Analysis of STIM1 dynamics

STIM1 dynamics were analyzed using the ImageJ software. To extract STIM1 puncta, the captured images were binarized after filtering (Gaussian Blur or Unsharp Mask). Then, particles greater than 2 pixels (corresponding to ~1.2 μm^2) were counted using the "Analyze Particles" tool in the ImageJ. The counts were normalized by the maximum values (N_{puncta}) and plotted against the ER Ca^{2+} levels (ERCa^{2+}) ($[Ca^{2+}]_{ER}$ for GEM-CEPIA1*er* and F/F_0 for G-CEPIA1*er*). Curve fitting was performed using the following Hill equation:

$$N_{puncta} = 1 - (ERCa^{2+})^n / [(ERCa^{2+})^n + (K_{1/2})^n],$$

where $K_{1/2}$ indicates the ER Ca^{2+} level at half maximal puncta formation and n represents Hill coefficient (59).

Imaging of subcellular localization of CEPIA

All images were captured with a confocal microscope (TCS SP8) equipped with a 63× objective at the following excitation/emission wavelengths: CEPIA1*er*, G-CEPIA1*er*, CEPIA2*mt*, EGFP-*er* and EYFP-*er* (488 nm/500–550 nm), R-CEPIA1*er*, mCherry-*er* and MitoTracker Red (Invitrogen) (552 nm/560– nm) and GEM-CEPIA1*er* (405 nm/420–550 nm). The obtained images were merged with ImageJ software.

ER Ca^{2+} imaging in cerebellar slices

For Purkinje cell-specific expression of G-CEPIA1*er*, a Sindbis virus vector (pSinRep5) encoding G-CEPIA1*er* was produced. The pSinRep5-G-CEPIA1*er* vector was then used as the template for in vitro transcription using SP6 RNA polymerase (Ambion, USA). The RNA transcript and the helper RNA from DH(26S) cDNA template (Invitrogen) were cotransfected into BHK cells by electroporation. Twenty-four hours after transfection, the culture medium containing the infectious particles was harvested. Sindbis virus vector encoding EYFP-*er* was also produced with the same procedure. C57BL/6 mice (postnatal day 21–27) were deeply anesthetized with pentobarbital, and the surface of cerebellar lobule 6 beside the midline was exposed by removing the cranium and dura. The tip of a glass pipette was backfilled with the viral solution. The glass pipette was then inserted into the cerebellum and 1 μL of viral solution was delivered at a rate of 200 nl min^{-1} using a micropump (Legato 130, KD scientific, USA). Twenty-four hours after virus injection, parasagittal cerebellar slices (250 μm

thickness) were prepared (60). Mice were anesthetized with diethyl ether and decapitated. The brain was removed and placed in ice-cold artificial cerebrospinal fluid (ACSF). Slices were cut using a microslicer (PRO 7, Dosaka EM, Japan). The slices were incubated in a holding chamber containing ACSF at 35°C for 1 h and then returned to 23°C. Slices were transferred to a recording chamber under microscope and continuously perfused with ACSF supplemented with 10 μM bicuculline (Tocris Bioscience, UK) and 10 μM NBQX (Tocris Bioscience) to block inhibitory postsynaptic potentials and accompanying Ca^{2+} influxes. ACSF contained (in mM) 125 NaCl, 2.5 KCl, 2 $CaCl_2$, 1 $MgSO_4$, 1.25 NaH_2PO_4, 26 $NaHCO_3$, and 20 glucose, and was bubbled with 95% O_2 and 5% CO_2.

Imaging was carried out with a two-photon microscope (TSC MP5, Leica) equipped with a water-immersion objective (25×, NA 0.95, HCS IR APO, Leica) and a Ti:sapphire laser (MaiTai DeepSee; Spectra Physics, USA). Excitation wavelength was 900–920 nm for both G-CEPIA1*er* and EYFP-*er*. Data were acquired with time-lapse XY-scan mode (8 Hz) and analyzed using ImageJ software. Fluorescence intensities were corrected for background fluorescence by measuring a non-fluorescent area. When necessary, photobleaching was corrected for using a linear fit to the fluorescence intensity change. For the focal stimulation of parallel fibers, square pulses (0.1 ms) were applied through stimulation pipettes (3–6 μm tip diameter) filled with ACSF. The stimulation intensity was adjusted within 4–5 V to induce G-CEPIA1*er* signals with a range of ~20 μm in diameter. For EYFP-*er*, the stimulation intensity was fixed at 5V. Experiments were carried out at RT.

Statistics

Two-tailed Student's *t*-tests were performed to determine the significance if not stated otherwise.

Results

Development of ER Ca^{2+} indicator

I began measuring ER Ca^{2+} dynamics based on a lead variant of GCaMP2 (cfGCaMP2, see Materials and Methods), whereby fluorescence intensity increased 5.1-fold upon binding of Ca^{2+} with an apparent dissociation constant (K_d) of 0.67 μM (Table 1a). Since ER Ca^{2+} concentration ($[Ca^{2+}]_{ER}$) is assumed to reach the sub-millimolar range, cfGCaMP2 was engineered to reduce its Ca^{2+} binding affinity by a factor of ~1,000. I searched for low Ca^{2+} affinity variants guided by extensive structure-function analyses based on site-directed mutagenesis in the calmodulin (CaM) domain of cfGCaMP2.

Ca^{2+} affinity of cfGCaMP2 is primarily determined by CaM, which has four EF-hand motifs. I first tried the amino acid substitutions that were used to reduce Ca^{2+} affinity of the FRET-type ER Ca^{2+} indicator, D1ER (23), but the K_d of cfGCaMP2 increased only to 14.5 μM (Figure 1a, gray circle). Amino acid substitutions at *–Z* position (12th amino acid residue) of the EF-hand motifs were previously shown to reduce the Ca^{2+} affinity of GFP-based Ca^{2+} indicators (15,17). When a non-acidic substitution (E31Q) at *–Z* in site I was introduced to cfGCaMP2, the K_d increased to 64.9 μM. However, its dynamic range (F_{max}/F_{min}) was reduced to 2.5 (Figure 1a, green circle). Another non-acidic substitution (E104Q) at *–Z* in site III produced no effect on the Ca^{2+} affinity (Figure 1a, light green circle). On the other hand, conservative E31D substitution in site I increased the K_d to 14.5 μM without reducing the

dynamic range. Therefore, I next systematically altered the glutamate residue at –*Z* positions (E31, E67, E104, and E140) to aspartate. The E67D variant had a K_d of 9.2 μM, while E104D and E140D variants had K_ds of 1.0 and 2.1 μM, respectively (Figure 1a, cyan circles). I then examined if combinations of multiple –*Z* substitutions would synergistically reduce the Ca^{2+} affinity. The K_d of E31D/E67D variant was strikingly increased to 470 μM, but its dynamic range was reduced to 2.6. Variants with other combinations of double substitutions had a K_d of ~25 μM, and retained a high dynamic range. Combinations of three –*Z* substitutions, (E31D or E67D)/E104D/E140D, produced variants with a K_d of some 130 μM (Figure 1a, blue circles). Thus I concluded that a different strategy for further improvement of the indicator was required.

Previous reports have shown that a combination of F92W/D133E substitutions can inhibit Ca^{2+} binding at site IV of CaM (61,62). Based on these reports, I found that a cfGCaMP2 variant with F92W/D133E substitutions had a K_d of 10.3 μM and a high dynamic range (Figure 1a, orange circles). I next examined whether combinations of F92W/D133E and –*Z* substitutions would synergistically reduce Ca^{2+} affinity. Indeed, combinations of F92W/D133E and one of the –*Z* substitutions generated variants with a K_d of 67–130 μM (Figure 1a, magenta circles). I further combined the F92W/D133E substitutions with double –*Z* substitutions, (E31D or E67D) plus (E104D or E140D), and obtained variants with a K_d of ~400 μM (Figure 1a, magenta circles). From among the 58 variants that were generated in this search, I finally selected one with E31D/F92W/E104D/D133E substitutions that had a

low Ca^{2+} affinity (K_d = 368 μM) and a large dynamic range (F_{max}/F_{min} = 4.2) (Table 1, Figures 1a and 1b). After attaching ER localization and retention signal sequences (Figure 1c), the low Ca^{2+} affinity variant was expressed in HeLa cells. The engineered indicator protein co-localized with an ER marker (63) (Figure 1d). Upon addition of thapsigargin, an inhibitor of SERCA, a large reduction in fluorescence intensity was noted (Figure 1e). Also, oscillatory fluorescence intensity was observed in response to histamine, which generates cytosolic Ca^{2+} oscillations due to release of Ca^{2+} from the ER via IP_3Rs (Figure 1f). Thus, the indicator successfully reports $[Ca^{2+}]_{ER}$ dynamics. I designated it Calcium-measuring organelle-Entrapped Protein IndicAtor 1 in the ER (CEPIA1*er*).

Multi-coloring of CEPIA

I next generated color variants of CEPIA, based on recently developed cytosolic Ca^{2+} indicators: R-GECO1 (red fluorescence), G-GECO1.1 (green fluorescence) and GEM-GECO1 (ratiometric blue/green fluorescence) (24). I first replaced the entire CaM domain of R-GECO1 with that of CEPIA1*er*, and obtained a variant with a K_d of 70.9 μM (Table 1b). Introduction of an additional –*Z* substitution (E67D) resulted in a variant with an optimal Ca^{2+} affinity (K_d = 565 μM) and a high dynamic range (8.8) (Table 1b and Figure 2a), which I designated R-CEPIA1*er*. Using the same strategy, I replaced the CaM domain of G-GECO1.1 with that of CEPIA1*er*, and obtained a variant with a K_d of 672 μM and a dynamic range of 4.7. This variant was designated as G-CEPIA1*er* (Table 1c and Figure 2a). I

next tried the same strategy in GEM-GECO1, but found that the dynamic range of the resulting indicator was markedly reduced (R_{max}/R_{min} = 1.1; Table 1d). Because several amino acid substitutions had been introduced to the CaM of GEM-GECO1 as compared with cfGCaMP2 (Figure 3), I concluded that these additional substitutions are essential. Accordingly, I created a variant where I reintroduced the GEM-GECO1 substitutions while maintaining the E31D/F92W/E104D/D133E substitutions, creating a variant with a low Ca^{2+} affinity and an increased dynamic range (K_d = 225 μM, R_{max}/R_{min} = 8.1; Table 1e). I further engineered the *–Z* positions, thus creating a variant with E31D/F92W/D133E/E140D substitutions with an optimal Ca^{2+} affinity and a high dynamic range (K_d = 558 μM, R_{max}/R_{min} = 21.7; Table 1e and Figure 2a). I designated this variant GEM-CEPIA1*er*. Substituted amino acids in each CEPIA*er* and genealogy of CEPIA variants were summarized in Figures 3 and 4, respectively. Spectral properties and in vitro characteristics of CEPIA*er*, compared with those of original GECO, were summarized in Table 2, Figures 5 and 6.

I expressed the color variants of CEPIA fused with ER-targeting signal sequences in HeLa cells. They localized to the ER (63,64) (Figures 2b–d), and detected ER Ca^{2+} signals including agonist-induced Ca^{2+} oscillation with a high signal-to-noise ratio (Figures 7a and 7b). In HeLa cells, G-CEPIA1*er* showed superior performance in signal amplitude over CEPIA1*er* (Figures 7a and 7b). To measure the Ca^{2+} affinity of CEPIA variants within the ER, I carried out Ca^{2+} titration experiments in permeabilized HeLa cells. Stepwise changes in Ca^{2+} concentration elicited dose-dependent fluorescence intensity changes in the presence of

ionomycin to make the ER membrane permeable to Ca^{2+} (Figure 8a). The K_d values determined within the ER were almost equivalent to those measured in vitro (Figure 8b). To examine whether pH changes had any effect on the signal of CEPIA indicators (Figure 6a), I monitored pH dynamics in the ER using a pH sensor, enhanced yellow fluorescent protein (EYFP, pK_a = 6.9) (65,66), because the pH value in the ER is estimated as 7.2 (55). There was no significant change in the fluorescence intensity of ER-localized EYFP (Figures 9a–d), verifying that the CEPIA responses are not due to pH changes in the ER. Thus, I succeeded in expanding the hues of CEPIA variants.

Estimation of $[Ca^{2+}]_{ER}$

Using ratiometric measurement with GEM-CEPIA1*er*, I estimated $[Ca^{2+}]_{ER}$ in intact resting cells as varying between 620 and 860 μM in HeLa cells, HEK293A cells, BHK cells and cultured astrocytes; these decreased to 310–570 μM upon stimulation with agonists (Figure 7d). The range of $[Ca^{2+}]_{ER}$ underlines the need to increase the indicator's K_d to >100 μM to provide faithful measurements of ER Ca^{2+} dynamics, and explains the difficulty in imaging ER Ca^{2+} dynamics using D1ER, which has a K_d of ~60 μM (23) (Figures 2a, 7a and 7b**)**. Although CEPIA indicators had relatively high Hill coefficients (n = 1.4–2.0, Table 2), the relationship between $\Delta F/F_{max}$ (or $\Delta R/R_{max}$) and changes in $[Ca^{2+}]$ is not highly distorted within the physiological $[Ca^{2+}]_{ER}$ range (Figure 6c).

Subcellular ER Ca^{2+} dynamics visualized with CEPIA

I next examined whether CEPIA indicators are capable of detecting ER Ca^{2+} dynamics at subcellular resolution. Agonists often induce Ca^{2+} waves, which propagate throughout the cell after initiation in focal regions (1,67). The wave is generated by the regenerative release of Ca^{2+} from the ER, and it has been predicted that this mechanism creates an "inverse Ca^{2+} wave" within the ER. However, this prediction has not been tested using GECIs in live cells. I used G-CEPIA1*er* imaging at a high frame rate (10–30 frames s^{-1}) to visualize inverse Ca^{2+} waves in the ER. Local decreases in $[Ca^{2+}]_{ER}$ were observed, initiating at the tips and propagating to the perinuclear region in HeLa cells (Figure 10a). The time courses measured at two subcellular locations indicated a wave-like propagation of decreasing $[Ca^{2+}]_{ER}$ (Figures 10b and 10c). The speed of these waves was 60.8 ± 3.2 μm s^{-1} (mean ± s.e.m.), which matches cytosolic Ca^{2+} waves with or without CEPIA expression (Figure 10d). Similar observations were made with R-CEPIA1*er* (Figure 10d). Thus, CEPIA indicators have high spatiotemporal resolution.

Next, it was examined whether CEPIA can be applied to intact tissue preparations. To do so, Ca^{2+} dynamics were elucidated in the neuronal ER in response to synaptic inputs to Purkinje cell dendrites in cerebellar slice preparations. G-CEPIA1*er* was expressed in Purkinje cells by Sindbis virus and was imaged with a two-photon microscope. G-CEPIA1*er* expression was observed throughout the dendrites and into spines, matching the distribution of the ER in Purkinje cells (Figure 11a). In response to parallel fiber (PF) stimulation, which

induces Ca^{2+} release from the ER through IP_3R by activating the metabotropic glutamate receptor 1 (mGluR1) (68), a long-lasting decrease in G-CEPIA1*er* fluorescence intensity was observed (Figure 11b). The ER Ca^{2+} dynamics could be visualized at the level of single spines (Figure 11c). This response was blocked by the application of LY367385, an mGluR1 antagonist (Figures 11d and 11e, blue), but not by the application of NBQX, an AMPA receptor antagonist (Figures 11d and 11e, magenta). The application of CPA, a SERCA inhibitor, induced slow depletion of ER Ca^{2+} (Figure 11f), followed by abolishment of the G-CEPIA1*er* response to PF stimulation (Figures 11d and 11e, orange). This response was not due to any pH change in the ER, because the PF stimulation had no effect on pH within the ER measured by ER-targeted EYFP (Figures 9e–g) (65,66). Thus, subcellular ER Ca^{2+} imaging using CEPIA is applicable to tissue preparations that have retained three-dimensional structure, which often requires two-photon excitation.

Simultaneous imaging of Ca^{2+} dynamics in the ER and cytosol

For simultaneous imaging of Ca^{2+} dynamics in the ER and cytosol, the ratiometric small-molecule Ca^{2+} indicator, fura-2 (excitation: 340–380 nm) was used together with G-CEPIA1*er* or R-CEPIA1*er*. ER Ca^{2+} signals were mirror images of the cytosolic Ca^{2+} oscillations (Figures 12a and 12b). Although G-CEPIA1*er* and R-CEPIA1*er* are weakly excited at the excitation wavelengths of fura-2 (Figures 5a and 13a), they had very little effect on the fura-2 fluorescence ratio (Figure 13b). Thus, it is possible to use G-CEPIA1*er* and

R-CEPIA1*er* with fura-2. Either G-CEPIA1*er* or GEM-CEPIA1*er* can be co-expressed with R-GECO1 for simultaneous imaging of the ER and cytosolic Ca^{2+} dynamics (Figures 12c–f). Reversal of the colors is also possible, and ER Ca^{2+} imaging using R-CEPIA1*er* can be simultaneously carried out with cytosolic Ca^{2+} imaging using G-GECO1.1 or GEM-GECO1 (Figures 12g and 12h). Spectral bleed-through was minimal (<3%, Figure 13a). These results show the versatility of CEPIA as ER Ca^{2+} indicators.

Imaging of store-operated Ca^{2+} entry

Store-operated Ca^{2+} entry (SOCE) is a ubiquitous process to replenish ER Ca^{2+} by inducing Ca^{2+} influx from the extracellular space (14), and has been shown to play an important role in the activation of immune cells (13). SOCE has been previously analyzed by measuring the increase in cytosolic Ca^{2+} concentration ($[Ca^{2+}]_{cyt}$) after store depletion by SERCA inhibitors, such as thapsigargin and cyclopiazonic acid (CPA). However, it remains unclear whether SOCE induces an increase in $[Ca^{2+}]_{cyt}$ under physiological conditions (69,70). Simultaneous Ca^{2+} imaging in the ER and cytosol using G-CEPIA1*er* and fura-2, respectively, provides a direct means to analyze Ca^{2+} dynamics during SOCE.

I found that stimulation of HeLa cells with histamine in the absence of extracellular Ca^{2+} induced an increase in $[Ca^{2+}]_{cyt}$ and concomitant partial depletion of $[Ca^{2+}]_{ER}$ (Figure 14a, black lines). Removal of histamine resulted in a shift of $[Ca^{2+}]_{cyt}$ to $[Ca^{2+}]_{ER}$ in the continued absence of extracellular Ca^{2+}. When Ca^{2+} was reintroduced to the extracellular space ("Ca^{2+}

add back"), a recovery of $[Ca^{2+}]_{ER}$ toward the pre-stimulation level was seen. During ER refilling with Ca^{2+}, the increase in $[Ca^{2+}]_{cyt}$ was extremely small ($\Delta[Ca^{2+}]_{cyt}$ = 4.8 ± 0.6 nM, Figures 14b–d) as compared with the large $[Ca^{2+}]_{cyt}$ increase (241 ± 14 nM) observed after SERCA blockade by CPA or thapsigargin (Figures 14a and 14e). ER refilling was blocked by Gd^{3+}, an Orai1 inhibitor (71) (Figure 14b, magenta lines). When STIM1 was extrinsically expressed in HeLa cells, the $[Ca^{2+}]_{cyt}$ and ER Ca^{2+} recovery rate during "Ca^{2+} add back" were significantly elevated (Figures 15a and 15d). These results indicate that, in HeLa cells, Ca^{2+} influx via SOCE is rapidly taken up by SERCA without forming a high-amplitude cytosolic Ca^{2+} signal unless STIM1 is overexpressed. I next examined Jurkat T cells stimulated with T cell receptor activation. In these cells, although Ca^{2+} influx via SOCE is partly taken up by SERCA as shown by the increase in $[Ca^{2+}]_{ER}$, there was a significant increase in the cytoplasmic Ca^{2+} concentration ($\Delta[Ca^{2+}]_{cyt}$ = 539 ± 38 nM, Figure 14f). Thus, unlike in HeLa cells, the rate of Ca^{2+} influx via SOCE surpasses the ER Ca^{2+} uptake rate in Jurkat T cells, and SOCE is capable of inducing an increase in $[Ca^{2+}]_{cyt}$.

CEPIA imaging simultaneous with other fluorescent molecules

Simultaneous time-lapse imaging of $[Ca^{2+}]_{ER}$ and other cellular processes should provide valuable information. I examined the possibility of simultaneously measuring $[Ca^{2+}]_{ER}$ and the subcellular distribution of STIM1, which senses the ER luminal Ca^{2+} concentration and, upon ER Ca^{2+} depletion, translocates to the subplasma membrane region to oligomerize (14).

Accumulating evidence suggests that the oligomerization of STIM1, which appears as a punctate structure of fluorescent protein-tagged STIM1, is a key determinant of SOCE (72).

I measured $[Ca^{2+}]_{ER}$ using GEM-CEPIA1*er* and simultaneously imaged STIM1 dynamics using mCherry-STIM1 (Figures 16a and 16b). Upon addition of histamine in the absence of extracellular Ca^{2+}, $[Ca^{2+}]_{ER}$ began to decrease in an almost linear fashion. The formation of STIM1 puncta was considerably delayed, being observed only after $[Ca^{2+}]_{ER}$ fell below 600 μM. Thereafter, puncta formation proceeded alongside further decreases in $[Ca^{2+}]_{ER}$. When Ca^{2+} was added back to the extracellular solution after histamine washout, $[Ca^{2+}]_{ER}$ refilling began and the mCherry-STIM1 puncta decomposed. The relationship between $[Ca^{2+}]_{ER}$ and puncta formation could be fitted by Hill plot, with a Hill coefficient of 7.9 and a $K_{1/2}$ of 350 μM for puncta formation, and 9.7 and 530 μM for dissociation (Figure 16c). Thus, the relationship between $[Ca^{2+}]_{ER}$ and puncta formation/dissociation exhibits considerable hysteresis. The difference of $K_{1/2}$ between puncta formation and dissociation was also observed using G-CEPIA1*er* and mCherry-STIM1 (Figures 15a–c). These observations indicate that, as far as $[Ca^{2+}]_{ER}$-dependent puncta formation of STIM1 is concerned, there is a threshold-like behavior, and suggest the existence of a mechanism that produces the delay in the dissociation of STIM1 puncta. Thus, CEPIA enables quantitative analysis of relationship between $[Ca^{2+}]_{ER}$ and STIM1 dynamics.

Intercellular heterogeneity of mitochondrial Ca^{2+} signaling

I examined whether CEPIA indicators can be utilized for Ca^{2+} imaging in mitochondria. To cover the broad range of mitochondrial Ca^{2+} concentrations (0.05–300 μM) (22,28,73), three CEPIA variants with different Ca^{2+} affinities were selected from the library: CEPIA2 (K_d = 0.16 μM), CEPIA3 (11 μM), and CEPIA4 (59 μM) (Table 1a, Figures 6d and 17a). These indicators were expressed in HeLa cells by adding the mitochondrial localization signal sequence (29) (CEPIA2*mt*, CEPIA3*mt* and CEPIA4*mt*) to their coding sequences. The expression colocalized with MitoTracker Red and was distinct from the ER (Figure 17b).

Histamine application to mobilize ER Ca^{2+} induced a rapid increase in mitochondrial Ca^{2+} levels followed by a slow decay (Figures 17c and 17d). This mitochondrial Ca^{2+} signal was abolished when the mitochondrial membrane potential was dissipated by carbonyl cyanide-p-trifluoromethoxyphenylhydrazone (FCCP) (Figures 17c and 17d).

Only a subpopulation of cells showed a mitochondrial Ca^{2+} response, and the fraction of responding cells decreased with the decreasing affinities of the CEPIA*mt* (Figures 17e–g). Enhancement of mitochondrial Ca^{2+}, either by extrinsic expression of MCU or by suppression of Na^+/Ca^{2+} exchanger-mediated mitochondrial Ca^{2+} clearance by CGP-37157, resulted in a striking increase in the fraction of cells displaying Ca^{2+} signals. Under these conditions, sustained or oscillatory mitochondrial responses were observed in a large fraction of cells, and obvious saturation of CEPIA*mt* was observed in many cells (Figures 17e and 17g). I concluded that CEPIA*mt* successfully reports mitochondrial Ca^{2+} signals, and that

mitochondrial Ca^{2+} dynamics during agonist stimulation have considerable cell-to-cell variation.

Subcellular heterogeneity of mitochondrial Ca^{2+} response

In a fraction of cells, agonist stimulation elicited a mitochondrial Ca^{2+} response throughout the cell. In the remaining cells, only a subpopulation of mitochondria responded with a Ca^{2+} increase. For example, in the cell shown in Figures 18a–c, mitochondrial Ca^{2+} concentration ($[Ca^{2+}]_{mt}$) measured with CEPIA3*mt* increased in region 2; the size of the increase was three times greater than that averaged over the entire cell. In contrast, there was no increase in $[Ca^{2+}]_{mt}$ in region 1. To exclude the possibility of regional variation in the CEPIA3*mt* response, I applied a Ca^{2+} ionophore, ionomycin. The same response was observed in both regions 1 and 2. Subcellular heterogeneity in mitochondrial Ca^{2+} dynamics was also visualized by CEPIA2*mt* (Figures 18d–f). These results indicate that there is a considerable subcellular variation in the capacity of mitochondria to take up Ca^{2+}.

I tested a possible role for the ER in this inhomogeneous mitochondrial Ca^{2+} response, since it has been postulated that ER Ca^{2+} release is important for mitochondrial Ca^{2+} responses (9). To this end, simultaneous Ca^{2+} imaging of the cytosol, ER and mitochondria was performed using GEM-GECO1, G-CEPIA1*er* and R-GECO1*mt*, respectively. Agonist stimulation induced a marked increase in $[Ca^{2+}]_{mt}$ in region 2 but not in adjacent mitochondria, including those in region 1. In contrast to the inhomogeneous mitochondrial response,

$[Ca^{2+}]_{ER}$ and $[Ca^{2+}]_{cyt}$ showed similar responses in regions 1 and 2 (Figure 19). I also examined the subcellular heterogeneity in mitochondrial pH or membrane potentials (Ψ_m) as a potential mechanism of heterogeneous mitochondrial Ca^{2+} responses (74-76). Simultaneous measurement of $[Ca^{2+}]_{mt}$ and pH_{mt} indicated that inhomogeneous Ca^{2+} responses are not due to pH changes (Figures 20a–d). Neither did I find any heterogeneity in Ψ_m, corresponding to mitochondrial Ca^{2+} responses (Figures 20e–f). These results suggest that the inhomogeneous mitochondrial Ca^{2+} response is generated by heterogeneity in the strength of ER-mitochondrial coupling or in the regulation of Ca^{2+} uptake protein rather than in the amount of Ca^{2+} released from the local ER or in pH or Ψ_m.

Discussion

Ca^{2+} concentrations within the ER and mitochondria control cytosolic Ca^{2+} dynamics and regulate cell functions including ER stress and cell death (3,8). Methods such as CEPIA that obtain direct information about intraorganellar Ca^{2+} dynamics are, therefore, of great importance. The merits of CEPIA indicators for imaging ER or mitochondrial Ca^{2+} concentrations can be summarized as follows. First, they have very high dynamic range and spatiotemporal resolution. This has allowed, for instance, the first imaging of an inverse Ca^{2+} wave and synaptic activity-dependent ER Ca^{2+} dynamics in neurons. Second, CEPIA allows simultaneous Ca^{2+} imaging in the ER, mitochondria and cytosol with subcellular resolution. Third, CEPIA indicators are applicable to many cell types including intact neurons. Fourth, ratiometric measurement is possible with GEM-CEPIA1*er*, whereby intraorganellar Ca^{2+} concentrations can be determined independent of the indicator's expression level. Fifth, the high signal-to-noise ratio and one-wave length measurement with G-CEPIA1*er* and R-CEPIA1*er* reduce the technical difficulty of organellar Ca^{2+} imaging and obviate the requirement for a special imaging apparatus. Thus, CEPIA-mediated imaging methods should have broad utility in many cell biological studies. Indeed, work described in this paper addresses important cell functions. Furthermore, in a recent study CEPIA is successfully used to prove that abnormal ER Ca^{2+} handling is associated with disease-related mutations of the RyR (77).

Influx of Ca^{2+} from the extracellular space to the cytoplasm through SOCE is found in many types of cells (13,78). The inhibition of SERCA (an ER Ca^{2+} pump) by pharmacological means, such as thapsigargin and CPA, to deplete ER Ca^{2+} has been the standard method to study the SOCE mechanism (13). Now, using CEPIA, I have studied SOCE under physiological conditions, without SERCA inhibition. This revealed that $[Ca^{2+}]_{cyt}$ is held constant during SOCE activation in HeLa cells, although $[Ca^{2+}]_{ER}$ is sufficiently low to induce significant $[Ca^{2+}]_{cyt}$ increase when SERCA is inhibited. These results indicate that the balance between the SOCE and SERCA activities is important for the capacity of SOCE to induce sustained increase in $[Ca^{2+}]_{cyt}$. In HeLa cells, SERCA activity is sufficiently high to take up Ca^{2+} influx through SOCE. However, the balance can differ between cell types, and if it favors Ca^{2+} influx there may be a large increase in $[Ca^{2+}]_{cyt}$ during SOCE activation. Indeed, I found that the balance favors Ca^{2+} influx in Jurkat T cells, being consistent with the importance of SOCE in immune cells (13).

SOCE is a remarkable mechanism, in which $[Ca^{2+}]_{ER}$ regulates the Ca^{2+} permeability in the plasma membrane. The ER Ca^{2+} transducer of SOCE is STIM1, which senses $[Ca^{2+}]_{ER}$ and translocates to the subplasmalemmal ER domain to form punctate structures and recruit Orai1 for Ca^{2+} influx through the plasma membrane. The steady-state $[Ca^{2+}]_{ER}$ dependence of the amplitude of ionic current carried by SOCE (I_{CRAC}) and the subplasmalemmal translocation of STIM1 has been quantified (79). I_{CRAC} and STIM1 translocation were found to be nonlinear functions of $[Ca^{2+}]_{ER}$ with a Hill coefficient of ~4

and a $K_{1/2}$ of ~200 μM. This is consistent with the dissociation constant of the Ca^{2+}-binding domain (EF-SAM) of STIM1 measured with a $^{45}Ca^{2+}$ binding assay (K_d = ~250 μM) (80). STIM1 deoligomerization for the termination of SOCE is thought to be mediated by ER Ca^{2+} refilling (14). Comparisons of the $[Ca^{2+}]_{ER}$ dependence of STIM1 puncta formation and dissociation have shown that the $K_{1/2}$ of STIM1 puncta dissociation is lower than that of formation (81,82). However, in these studies, STIM1 dynamics and $[Ca^{2+}]_{ER}$ had to be measured in separate cells, because both signals were measured using FRET between YFP and CFP. I found that extrinsic expression of STIM1 significantly increases both $[Ca^{2+}]_{cyt}$ and ER Ca^{2+} refilling rate during SOCE. Thus, the comparison between cells with and without STIM1 expression requires caution. To circumvent this problem, I simultaneously measured STIM1 puncta formation/dissociation and $[Ca^{2+}]_{ER}$ in the same cells. Both STIM1 puncta formation and dissociation were highly nonlinear functions of $[Ca^{2+}]_{ER}$. Furthermore, the $K_{1/2}$ of $[Ca^{2+}]_{ER}$ for puncta dissociation was greater than that for formation (530 and 350 μM for dissociation and formation, respectively). These results indicate that the STIM1 deoligomerization process is not a simple reversal reaction of STIM1 oligomerization.

Within neurons the ER forms a continuous network throughout the cell (described as “a neuron within a neuron” (2,83)) that produces slowly-propagating regenerative Ca^{2+} signals using a conduction system based on IP_3R and RyR. However, neuronal ER Ca^{2+} dynamics have previously been estimated only indirectly, by cytosolic Ca^{2+} imaging. In this study, G-CEPIA1*er* was successfully used to visualize Ca^{2+} dynamics in the neuronal ER, in

response to synaptic inputs to Purkinje cell dendrites in cerebellar slice preparations. Subsequent study using G-CEPIA1*er* indicated that Ca^{2+} diffusion within the ER (Ca^{2+} tunneling) is critical for the replenishment of ER Ca^{2+} after synaptic inputs in cerebellar Purkinje cells (84). Neuronal ER Ca^{2+} dynamics are important for physiological functions such as synaptic plasticity (83), but also for pathophysiological states including neurodegenerative diseases (8,85). Thus, the application of CEPIA to intact neurons should provide a new imaging modality to analyze brain function.

Accumulating evidence suggests that Ca^{2+} dynamics in mitochondria are involved in the regulation of cell physiology and pathology, including autophagy, cell death, ATP synthesis, mitochondrial morphology and neurodegenerative diseases (3,12). Mitochondria constantly undergo fusion and fission for the maintenance of functions (86). Thus, subcellular inhomogeneity in mitochondrial functions is of great importance. Intracellular inhomogeneity in mitochondrial Ca^{2+} dynamics was first proposed based on mitochondria-targeted aequorin measurements (87), although these measurements did not have spatial resolution, and the inhomogeneity was inferred from the partial consumption of aequorin. Later, mitochondria-targeted GECIs were used to image the subcellular mitochondrial Ca^{2+} response following agonist-induced ER Ca^{2+} release (21,22,26). These studies revealed that, after a rapid increase in $[Ca^{2+}]_{mt}$ in response to agonist stimulation, there is a considerable variation in the decay timecourse among the subpopulation of mitochondria within the cell, and a few minutes after the agonist stimulation only a minor subpopulation of mitochondria retained the

increase in $[Ca^{2+}]_{mt}$ (21,22,26). The results obtained in this study showed that there is considerable intercellular and intracellular inhomogeneity in mitochondrial Ca^{2+} responses after agonist-induced Ca^{2+} release from the ER through IP_3Rs, despite the fact that consistent cytosolic Ca^{2+} increases were observed. These results are consistent with the observation using a small molecular Ca^{2+} indicator (88). Furthermore, simultaneous Ca^{2+} imaging of the ER and mitochondria did not show any inhomogeneous ER Ca^{2+} release. The inhomogeneity of the resting Ψ_m did also not correlate with the inhomogeneity of Ca^{2+} signal. These findings indicate that mitochondrial Ca^{2+} responses involve more than simple, passive uptake of cytosolic Ca^{2+}; there must be a regulatory mechanism for Ca^{2+} uptake. One possibility is that recently-identified MCU (3,89,90) and its associate proteins such as mitochondrial calcium uptake 1 (MICU1) (57), Mitochondrial Calcium Uniporter Regulator 1 (MCUR1) (91), MCU regulatory subunit (MCUb) (92), and essential MCU regulator (EMRE) (93) as well as H^+/Ca^{2+} exchanger, Na^+/Ca^{2+} exchanger (3) are regulated in a subcellular region-specific manner. Another possibility is that ER-mitochondria tethering proteins such as mitofusin 2 (12) are inhomogeneously distributed allowing region-specific transfer of Ca^{2+} from the ER to mitochondria at the ER-mitochondrial junction (10,11). Further studies using CEPIA will provide clues to the mechanism coupling between the ER and mitochondria.

I created fifty-eight variants of cfGCaMP2 and studied how their fluorescence intensity related to Ca^{2+} levels. This work shed light on the structure-function relationship of CaM-based indicators. Previous studies have reported that highly conserved glutamate

residues at –*Z* position in each EF-hand motif are key determinants of the Ca^{2+} sensitivity of CaM-based Ca^{2+} indicators (15,17,94). Here I further established that the substitution of glutamate with a non-acidic amino acid (E31A or E31Q) reduces not only the Ca^{2+} binding affinity but also the dynamic range of the indicator. In contrast, conservative substitutions to aspartate reduced the Ca^{2+} binding affinity, while maintaining the dynamic range. In line with this observation, a previous report showed that charge-reversing substitutions (E31K or E67K) resulted in a reduction of the dynamic range of GCaMP (94). These results suggest that the acidic residue in –*Z* position is not only the key determinant of Ca^{2+} binding affinity, but is also important for the efficient conformational change upon Ca^{2+} binding (62). F92W and D133E substitutions that reduce Ca^{2+} binding affinity without affecting the dynamic range have been previously reported for proteins possessing CaM-dependent enzymatic activity (61). Combining these two types of substitutions synergistically reduced Ca^{2+} binding affinity, which led to the generation of CEPIA indicators. This strategy may be applicable for the generation of ER and mitochondrial Ca^{2+} indicators based on other CaM-based indicators.

Other groups also developed ER-targeted GECIs on the basis of GCaMP or GECO with amino acids substitutions different from CEPIA. ER-LAR-GECO1 was generated by combined strategies of random and site-directed mutagenesis on the CaM-M13 interaction sites in R-GECO1 (34). GCaMPer (10.19) was created by introducing multiple mutations in the Ca^{2+} binding sites of GCaMP3 (35). Both indicators are successfully used to detect ER Ca^{2+} signals similar with CEPIA. The amino acid substitutions used in these indicators may

have a potential to be used for further improvement of CEPIA by combined with mutations in CEPIA library.

In summary, CEPIA-based imaging will contribute to the understanding of intraorganellar dynamics of Ca^{2+}, and thus to elucidation of the functions of the ER and mitochondria in a variety of cells.

References

1. Berridge, M.J., Lipp, P. & Bootman, M.D. The versatility and universality of calcium signalling. *Nat. Rev. Mol. Cell Biol.* **1**, 11-21 (2000).

2. Berridge, M.J., Bootman, M.D. & Lipp, P. Calcium–a life and death signal. *Nature* **395**, 645-648 (1998).

3. Rizzuto, R., De Stefani, D., Raffaello, A. & Mammucari, C. Mitochondria as sensors and regulators of calcium signalling. *Nat. Rev. Mol. Cell Biol.* **13**, 566-578 (2012).

4. Alonso, M.T. & Garcia-Sancho, J. Nuclear Ca^{2+} signalling. *Cell Calcium* **49**, 280-289 (2011).

5. Miyawaki, A. & Niino, Y. Molecular spies for bioimaging—fluorescent protein-based probes. *Mol. Cell* **58**, 632-643 (2015).

6. Brini, M. & Carafoli, E. Calcium pumps in health and disease. *Physiol. Rev.* **89**, 1341-1378 (2009).

7. Berridge, M.J., Bootman, M.D. & Roderick, H.L. Calcium signalling: dynamics, homeostasis and remodelling. *Nat. Rev. Mol. Cell Biol.* **4**, 517-529 (2003).

8. Mekahli, D., Bultynck, G., Parys, J.B., De Smedt, H. & Missiaen, L. Endoplasmic-reticulum calcium depletion and disease. *Cold Spring Harb. Perspect. Biol.* **3** (2011).

9. Rowland, A.A. & Voeltz, G.K. Endoplasmic reticulum-mitochondria contacts: function of the junction. *Nat. Rev. Mol. Cell Biol.* **13**, 607-625 (2012).

10. Csordas, G., Varnai, P., Golenar, T., Roy, S., Purkins, G., Schneider, T.G., Balla, T. & Hajnoczky, G. Imaging interorganelle contacts and local calcium dynamics at the ER-mitochondrial interface. *Mol. Cell* **39**, 121-132 (2010).

11. Giacomello, M., Drago, I., Bortolozzi, M., Scorzeto, M., Gianelle, A., Pizzo, P. & Pozzan, T. Ca^{2+} hot spots on the mitochondrial surface are generated by Ca^{2+} mobilization from stores, but not by activation of store-operated Ca^{2+} channels. *Mol. Cell* **38**, 280-290 (2010).

12. de Brito, O.M. & Scorrano, L. Mitofusin 2 tethers endoplasmic reticulum to mitochondria. *Nature* **456**, 605-610 (2008).

13. Hogan, P.G., Lewis, R.S. & Rao, A. Molecular basis of calcium signaling in lymphocytes: STIM and ORAI. *Annu. Rev. Immunol.* **28**, 491-533 (2010).

14. Soboloff, J., Rothberg, B.S., Madesh, M. & Gill, D.L. STIM proteins: dynamic calcium signal transducers. *Nat. Rev. Mol. Cell Biol.* **13**, 549-565 (2012).

15. Ishii, K., Hirose, K. & Iino, M. Ca^{2+} shuttling between endoplasmic reticulum and mitochondria underlying Ca^{2+} oscillations. *EMBO Rep.* **7**, 390-396 (2006).

16. Palmer, A.E., Qin, Y., Park, J.G. & McCombs, J.E. Design and application of genetically encoded biosensors. *Trends Biotechnol.* **29**, 144-152 (2011).

17. Miyawaki, A., Llopis, J., Heim, R., McCaffery, J.M., Adams, J.A., Ikura, M. & Tsien, R.Y. Fluorescent indicators for Ca^{2+} based on green fluorescent proteins and calmodulin. *Nature* **388**, 882-887 (1997).

18. Tang, S., Wong, H.C., Wang, Z.M., Huang, Y., Zou, J., Zhuo, Y., Pennati, A., Gadda, G., Delbono, O. & Yang, J.J. Design and application of a class of sensors to monitor Ca^{2+} dynamics in high Ca^{2+} concentration cellular compartments. *Proc. Natl. Acad. Sci. USA* **108**, 16265-16270 (2011).

19. Rodriguez-Garcia, A., Rojo-Ruiz, J., Navas-Navarro, P., Aulestia, F.J., Gallego-Sandin, S., Garcia-Sancho, J. & Alonso, M.T. GAP, an aequorin-based fluorescent indicator for imaging Ca^{2+} in organelles. *Proc. Natl. Acad. Sci. USA* **111**, 2584-2589 (2014).

20. Zou, J., Hofer, A.M., Lurtz, M.M., Gadda, G., Ellis, A.L., Chen, N., Huang, Y., Holder, A., Ye, Y., Louis, C.F., Welshhans, K., Rehder, V. & Yang, J.J. Developing sensors for real-time measurement of high Ca^{2+} concentrations. *Biochemistry* **46**, 12275-12288 (2007).

21. Nagai, T., Sawano, A., Park, E.S. & Miyawaki, A. Circularly permuted green fluorescent proteins engineered to sense Ca^{2+}. *Proc. Natl. Acad. Sci. USA* **98**, 3197-3202 (2001).

22. Palmer, A.E., Giacomello, M., Kortemme, T., Hires, S.A., Lev-Ram, V., Baker, D. & Tsien, R.Y. Ca^{2+} indicators based on computationally redesigned calmodulin-peptide pairs. *Chem. Biol.* **13**, 521-530 (2006).

23. Palmer, A.E., Jin, C., Reed, J.C. & Tsien, R.Y. Bcl-2-mediated alterations in endoplasmic reticulum Ca^{2+} analyzed with an improved genetically encoded fluorescent sensor. *Proc. Natl. Acad. Sci. USA* **101**, 17404-17409 (2004).

24. Zhao, Y., Araki, S., Wu, J., Teramoto, T., Chang, Y.F., Nakano, M., Abdelfattah, A.S., Fujiwara, M., Ishihara, T., Nagai, T. & Campbell, R.E. An expanded palette of genetically encoded Ca^{2+} indicators. *Science* **333**, 1888-1891 (2011).

25. Rudolf, R., Magalhaes, P.J. & Pozzan, T. Direct in vivo monitoring of sarcoplasmic reticulum Ca^{2+} and cytosolic cAMP dynamics in mouse skeletal muscle. *J. Cell Biol.* **173**, 187-193 (2006).

26. Filippin, L., Magalhaes, P.J., Di Benedetto, G., Colella, M. & Pozzan, T. Stable interactions between mitochondria and endoplasmic reticulum allow rapid accumulation of calcium in a subpopulation of mitochondria. *J. Biol. Chem.* **278**, 39224-39234 (2003).

27. Griesbeck, O., Baird, G.S., Campbell, R.E., Zacharias, D.A. & Tsien, R.Y. Reducing the environmental sensitivity of yellow fluorescent protein. Mechanism and applications. *J. Biol. Chem.* **276**, 29188-29194 (2001).

28. Arnaudeau, S., Kelley, W.L., Walsh, J.V., Jr. & Demaurex, N. Mitochondria recycle Ca^{2+} to the endoplasmic reticulum and prevent the depletion of neighboring endoplasmic reticulum regions. *J. Biol. Chem.* **276**, 29430-29439 (2001).

29. Filippin, L., Abad, M.C., Gastaldello, S., Magalhaes, P.J., Sandona, D. & Pozzan, T. Improved strategies for the delivery of GFP-based Ca^{2+} sensors into the mitochondrial matrix. *Cell Calcium* **37**, 129-136 (2005).

30. Osibow, K., Malli, R., Kostner, G.M. & Graier, W.F. A new type of non-Ca^{2+}-buffering Apo(a)-based fluorescent indicator for intraluminal Ca^{2+} in the endoplasmic reticulum. *J. Biol. Chem.* **281**, 5017-5025 (2006).

31. Ravier, M.A., Daro, D., Roma, L.P., Jonas, J.C., Cheng-Xue, R., Schuit, F.C. & Gilon, P. Mechanisms of control of the free Ca^{2+} concentration in the endoplasmic reticulum of mouse pancreatic beta-cells: interplay with cell metabolism and $[Ca^{2+}]_c$ and role of SERCA2b and SERCA3. *Diabetes* **60**, 2533-2545 (2011).

32. Ai, H.W., Henderson, J.N., Remington, S.J. & Campbell, R.E. Directed evolution of a monomeric, bright and photostable version of Clavularia cyan fluorescent protein: structural characterization and applications in fluorescence imaging. *Biochem. J.* **400**, 531-540 (2006).

33. Haviland, S., Cleemann, L., Kettlewell, S., Smith, G.L. & Morad, M. Diversity of mitochondrial Ca^{2+} signaling in rat neonatal cardiomyocytes: evidence from a genetically directed Ca^{2+} probe, mitycam-E31Q. *Cell Calcium* **56**, 133-146 (2014).

34. Wu, J., Prole, D.L., Shen, Y., Lin, Z., Gnanasekaran, A., Liu, Y., Chen, L., Zhou, H., Chen, S.R., Usachev, Y.M., Taylor, C.W. & Campbell, R.E. Red fluorescent

genetically encoded Ca^{2+} indicators for use in mitochondria and endoplasmic reticulum. *Biochem. J.* **464**, 13-22 (2014).

35. Henderson, M.J., Baldwin, H.A., Werley, C.A., Boccardo, S., Whitaker, L.R., Yan, X., Holt, G.T., Schreiter, E.R., Looger, L.L., Cohen, A.E., Kim, D.S. & Harvey, B.K. A Low Affinity GCaMP3 Variant (GCaMPer) for Imaging the Endoplasmic Reticulum Calcium Store. *PloS one* **10**, e0139273 (2015).

36. Palmer, A.E. & Tsien, R.Y. Measuring calcium signaling using genetically targetable fluorescent indicators. *Nat. Ptoroc.* **1**, 1057-1065 (2006).

37. Zampese, E., Fasolato, C., Kipanyula, M.J., Bortolozzi, M., Pozzan, T. & Pizzo, P. Presenilin 2 modulates endoplasmic reticulum (ER)-mitochondria interactions and Ca^{2+} cross-talk. *Proc. Natl. Acad. Sci. USA* **108**, 2777-2782 (2011).

38. Waldeck-Weiermair, M., Alam, M.R., Khan, M.J., Deak, A.T., Vishnu, N., Karsten, F., Imamura, H., Graier, W.F. & Malli, R. Spatiotemporal correlations between cytosolic and mitochondrial Ca^{2+} signals using a novel red-shifted mitochondrial targeted cameleon. *PloS one* **7**, e45917 (2012).

39. Iguchi, M., Kato, M., Nakai, J., Takeda, T., Matsumoto-Ida, M., Kita, T., Kimura, T. & Akao, M. Direct monitoring of mitochondrial calcium levels in cultured cardiac myocytes using a novel fluorescent indicator protein, GCaMP2-mt. *Int. J. Cardiol.* **158**, 225-234 (2012).

40. Isshiki, M., Nishimoto, M., Mizuno, R. & Fujita, T. FRET-based sensor analysis reveals caveolae are spatially distinct Ca^{2+} stores in endothelial cells. *Cell Calcium* **54**, 395-403 (2013).

41. Li, H., Wang, X., Zhang, N., Gottipati, M.K., Parpura, V. & Ding, S. Imaging of mitochondrial Ca^{2+} dynamics in astrocytes using cell-specific mitochondria-targeted GCaMP5G/6s: mitochondrial Ca^{2+} uptake and cytosolic Ca^{2+} availability via the endoplasmic reticulum store. *Cell Calcium* **56**, 457-466 (2014).

42. Logan, C.V., Szabadkai, G., Sharpe, J.A., Parry, D.A., Torelli, S., Childs, A.M., Kriek, M., Phadke, R., Johnson, C.A., Roberts, N.Y., Bonthron, D.T., Pysden, K.A., Whyte, T., Munteanu, I., Foley, A.R., Wheway, G., Szymanska, K., Natarajan, S., Abdelhamed, Z.A., Morgan, J.E., Roper, H., Santen, G.W., Niks, E.H., van der Pol, W.L., Lindhout, D., Raffaello, A., De Stefani, D., den Dunnen, J.T., Sun, Y., Ginjaar, I., Sewry, C.A., Hurles, M., Rizzuto, R., Consortium, U.K., Duchen, M.R., Muntoni, F. & Sheridan, E. Loss-of-function mutations in MICU1 cause a brain and muscle disorder linked to primary alterations in mitochondrial calcium signaling. *Nat. Genet.* **46**, 188-193 (2014).

43. Lynes, E.M., Raturi, A., Shenkman, M., Ortiz Sandoval, C., Yap, M.C., Wu, J., Janowicz, A., Myhill, N., Benson, M.D., Campbell, R.E., Berthiaume, L.G., Lederkremer, G.Z. & Simmen, T. Palmitoylation is the switch that assigns calnexin to quality control or ER Ca^{2+} signaling. *J. Cell Sci.* **126**, 3893-3903 (2013).

44. Frieden, M., James, D., Castelbou, C., Danckaert, A., Martinou, J.C. & Demaurex, N. Ca^{2+} homeostasis during mitochondrial fragmentation and perinuclear clustering induced by hFis1. *J. Biol. Chem.* **279**, 22704-22714 (2004).

45. Kettlewell, S., Cabrero, P., Nicklin, S.A., Dow, J.A., Davies, S. & Smith, G.L. Changes of intra-mitochondrial Ca^{2+} in adult ventricular cardiomyocytes examined using a novel fluorescent Ca^{2+} indicator targeted to mitochondria. *J. Mol. Cell. Cardiol.* **46**, 891-901 (2009).

46. Chang, K.T., Niescier, R.F. & Min, K.T. Mitochondrial matrix Ca^{2+} as an intrinsic signal regulating mitochondrial motility in axons. *Proc. Natl. Acad. Sci. USA* **108**, 15456-15461 (2011).

47. Waldeck-Weiermair, M., Bischof, H., Blass, S., Deak, A.T., Klec, C., Graier, T., Roller, C., Rost, R., Eroglu, E., Gottschalk, B., Hofmann, N.A., Graier, W.F. & Malli, R. Generation of Red-Shifted Cameleons for Imaging Ca^{2+} Dynamics of the Endoplasmic Reticulum. *Sensors (Basel)* **15**, 13052-13068 (2015).

48. Tsai, F.C., Seki, A., Yang, H.W., Hayer, A., Carrasco, S., Malmersjo, S. & Meyer, T. A polarized Ca^{2+}, diacylglycerol and STIM1 signalling system regulates directed cell migration. *Nat. Cell Biol.* **16**, 133-144 (2014).

49. Bonora, M., Giorgi, C., Bononi, A., Marchi, S., Patergnani, S., Rimessi, A., Rizzuto, R. & Pinton, P. Subcellular calcium measurements in mammalian cells using jellyfish photoprotein aequorin-based probes. *Nat. Ptoroc.* **8**, 2105-2118 (2013).

50. Carlson, H.J. & Campbell, R.E. Genetically encoded FRET-based biosensors for multiparameter fluorescence imaging. *Curr. Opin. Biotechnol.* **20**, 19-27 (2009).

51. Wier, W.G., Rizzo, M.A., Raina, H. & Zacharia, J. A technique for simultaneous measurement of Ca^{2+}, FRET fluorescence and force in intact mouse small arteries. *J. Physiol.* **586**, 2437-2443 (2008).

52. Poburko, D., Santo-Domingo, J. & Demaurex, N. Dynamic regulation of the mitochondrial proton gradient during cytosolic calcium elevations. *J. Biol. Chem.* **286**, 11672-11684 (2011).

53. Baba, Y., Hayashi, K., Fujii, Y., Mizushima, A., Watarai, H., Wakamori, M., Numaga, T., Mori, Y., Iino, M., Hikida, M. & Kurosaki, T. Coupling of STIM1 to store-operated Ca^{2+} entry through its constitutive and inducible movement in the endoplasmic reticulum. *Proc. Natl. Acad. Sci. USA* **103**, 16704-16709 (2006).

54. Tsien, R. & Pozzan, T. Measurement of cytosolic free Ca^{2+} with quin2. *Methods Enzymol.* **172**, 230-262 (1989).

55. Casey, J.R., Grinstein, S. & Orlowski, J. Sensors and regulators of intracellular pH. *Nat. Rev. Mol. Cell Biol.* **11**, 50-61 (2010).

56. Kanemaru, K., Okubo, Y., Hirose, K. & Iino, M. Regulation of neurite growth by spontaneous Ca^{2+} oscillations in astrocytes. *J. Neurosci.* **27**, 8957-8966 (2007).

57. Perocchi, F., Gohil, V.M., Girgis, H.S., Bao, X.R., McCombs, J.E., Palmer, A.E. & Mootha, V.K. MICU1 encodes a mitochondrial EF hand protein required for Ca^{2+} uptake. *Nature* **467**, 291-296 (2010).

58. Kneen, M., Farinas, J., Li, Y. & Verkman, A.S. Green fluorescent protein as a noninvasive intracellular pH indicator. *Biophys. J.* **74**, 1591-1599 (1998).

59. Brandman, O., Liou, J., Park, W.S. & Meyer, T. STIM2 is a feedback regulator that stabilizes basal cytosolic and endoplasmic reticulum Ca^{2+} levels. *Cell* **131**, 1327-1339 (2007).

60. Edwards, F.A., Konnerth, A., Sakmann, B. & Takahashi, T. A thin slice preparation for patch clamp recordings from neurones of the mammalian central nervous system. *Pflugers Arch.* **414**, 600-612 (1989).

61. Wu, X. & Reid, R.E. Conservative D133E mutation of calmodulin site IV drastically alters calcium binding and phosphodiesterase regulation. *Biochemistry* **36**, 3608-3616 (1997).

62. Yang, J.J., Gawthrop, A. & Ye, Y. Obtaining site-specific calcium-binding affinities of calmodulin. *Protein Peptide Lett.* **10**, 331-345 (2003).

63. Alford, S.C., Ding, Y., Simmen, T. & Campbell, R.E. Dimerization-dependent green and yellow fluorescent proteins. *ACS Synth. Biol.* **1**, 569-575 (2012).

64. Calloway, N., Vig, M., Kinet, J.P., Holowka, D. & Baird, B. Molecular clustering of STIM1 with Orai1/CRACM1 at the plasma membrane depends dynamically on

depletion of Ca^{2+} stores and on electrostatic interactions. *Mol. Biol. Cell* **20**, 389-399 (2009).

65. Miyawaki, A., Griesbeck, O., Heim, R. & Tsien, R.Y. Dynamic and quantitative Ca^{2+} measurements using improved cameleons. *Proc. Natl. Acad. Sci. USA* **96**, 2135-2140 (1999).

66. Foyouzi-Youssefi, R., Arnaudeau, S., Borner, C., Kelley, W.L., Tschopp, J., Lew, D.P., Demaurex, N. & Krause, K.H. Bcl-2 decreases the free Ca^{2+} concentration within the endoplasmic reticulum. *Proc. Natl. Acad. Sci. USA* **97**, 5723-5728 (2000).

67. Bootman, M.D., Berridge, M.J. & Lipp, P. Cooking with calcium: the recipes for composing global signals from elementary events. *Cell* **91**, 367-373 (1997).

68. Okubo, Y., Kakizawa, S., Hirose, K. & Iino, M. Cross talk between metabotropic and ionotropic glutamate receptor-mediated signaling in parallel fiber-induced inositol 1,4,5-trisphosphate production in cerebellar Purkinje cells. *J. Neurosci.* **24**, 9513-9520 (2004).

69. Grimaldi, M. Astrocytes refill intracellular Ca^{2+} stores in the absence of cytoplasmic $[Ca^{2+}]$ elevation: a functional rather than a structural ability. *J. Neurosci. Res.* **84**, 1738-1749 (2006).

70. Hofer, A.M., Landolfi, B., Debellis, L., Pozzan, T. & Curci, S. Free $[Ca^{2+}]$ dynamics measured in agonist-sensitive stores of single living intact cells: a new look at the refilling process. *EMBO J.* **17**, 1986-1995 (1998).

71. Zhang, S.L., Yeromin, A.V., Hu, J., Amcheslavsky, A., Zheng, H. & Cahalan, M.D. Mutations in Orai1 transmembrane segment 1 cause STIM1-independent activation of Orai1 channels at glycine 98 and channel closure at arginine 91. *Proc. Natl. Acad. Sci. USA* **108**, 17838-17843 (2011).

72. Cahalan, M.D. STIMulating store-operated Ca^{2+} entry. *Nat. Cell Biol.* **11**, 669-677 (2009).

73. Montero, M., Alonso, M.T., Carnicero, E., Cuchillo-Ibanez, I., Albillos, A., Garcia, A.G., Garcia-Sancho, J. & Alvarez, J. Chromaffin-cell stimulation triggers fast millimolar mitochondrial Ca^{2+} transients that modulate secretion. *Nat. Cell Biol.* **2**, 57-61 (2000).

74. Santo-Domingo, J., Giacomello, M., Poburko, D., Scorrano, L. & Demaurex, N. OPA1 promotes pH flashes that spread between contiguous mitochondria without matrix protein exchange. *EMBO J.* **32**, 1927-1940 (2013).

75. Buckman, J.F. & Reynolds, I.J. Spontaneous changes in mitochondrial membrane potential in cultured neurons. *J. Neurosci.* **21**, 5054-5065 (2001).

76. Collins, T.J., Berridge, M.J., Lipp, P. & Bootman, M.D. Mitochondria are morphologically and functionally heterogeneous within cells. *EMBO J.* **21**, 1616-1627 (2002).

77. Murayama, T., Kurebayashi, N., Yamazawa, T., Oyamada, H., Suzuki, J., Kanemaru, K., Oguchi, K., Iino, M. & Sakurai, T. Divergent Activity Profiles of Type 1

Ryanodine Receptor Channels Carrying Malignant Hyperthermia and Central Core Disease Mutations in the Amino-Terminal Region. *PloS one* **10**, e0130606 (2015).

78. Lewis, R.S. Store-operated calcium channels: new perspectives on mechanism and function. *Cold Spring Harb. Perspect. Biol.* **3** (2011).

79. Luik, R.M., Wang, B., Prakriya, M., Wu, M.M. & Lewis, R.S. Oligomerization of STIM1 couples ER calcium depletion to CRAC channel activation. *Nature* **454**, 538-542 (2008).

80. Stathopulos, P.B., Zheng, L., Li, G.Y., Plevin, M.J. & Ikura, M. Structural and mechanistic insights into STIM1-mediated initiation of store-operated calcium entry. *Cell* **135**, 110-122 (2008).

81. Malli, R., Naghdi, S., Romanin, C. & Graier, W.F. Cytosolic Ca^{2+} prevents the subplasmalemmal clustering of STIM1: an intrinsic mechanism to avoid Ca^{2+} overload. *J. Cell Sci.* **121**, 3133-3139 (2008).

82. Shen, W.W., Frieden, M. & Demaurex, N. Local cytosolic Ca^{2+} elevations are required for stromal interaction molecule 1 (STIM1) de-oligomerization and termination of store-operated Ca^{2+} entry. *J. Biol. Chem.* **286**, 36448-36459 (2011).

83. Ross, W.N. Understanding calcium waves and sparks in central neurons. *Nat. Rev. Neurosci.* **13**, 157-168 (2012).

84. Okubo, Y., Suzuki, J., Kanemaru, K., Nakamura, N., Shibata, T. & Iino, M. Visualization of Ca^{2+} Filling Mechanisms upon Synaptic Inputs in the Endoplasmic Reticulum of Cerebellar Purkinje Cells. *J. Neurosci.* **35**, 15837-15846 (2015).

85. Stutzmann, G.E. & Mattson, M.P. Endoplasmic reticulum Ca^{2+} handling in excitable cells in health and disease. *Pharmacol. Rev.* **63**, 700-727 (2011).

86. Westermann, B. Mitochondrial fusion and fission in cell life and death. *Nat. Rev. Mol. Cell Biol.* **11**, 872-884 (2010).

87. Rizzuto, R., Bastianutto, C., Brini, M., Murgia, M. & Pozzan, T. Mitochondrial Ca^{2+} homeostasis in intact cells. *J. Cell Biol.* **126**, 1183-1194 (1994).

88. Collins, T.J., Lipp, P., Berridge, M.J. & Bootman, M.D. Mitochondrial Ca^{2+} uptake depends on the spatial and temporal profile of cytosolic Ca^{2+} signals. *J. Biol. Chem.* **276**, 26411-26420 (2001).

89. Baughman, J.M., Perocchi, F., Girgis, H.S., Plovanich, M., Belcher-Timme, C.A., Sancak, Y., Bao, X.R., Strittmatter, L., Goldberger, O., Bogorad, R.L., Koteliansky, V. & Mootha, V.K. Integrative genomics identifies MCU as an essential component of the mitochondrial calcium uniporter. *Nature* **476**, 341-345 (2011).

90. De Stefani, D., Raffaello, A., Teardo, E., Szabo, I. & Rizzuto, R. A forty-kilodalton protein of the inner membrane is the mitochondrial calcium uniporter. *Nature* **476**, 336-340 (2011).

91. Mallilankaraman, K., Cardenas, C., Doonan, P.J., Chandramoorthy, H.C., Irrinki, K.M., Golenar, T., Csordas, G., Madireddi, P., Yang, J., Muller, M., Miller, R., Kolesar, J.E., Molgo, J., Kaufman, B., Hajnoczky, G., Foskett, J.K. & Madesh, M. MCUR1 is an essential component of mitochondrial Ca^{2+} uptake that regulates cellular metabolism. *Nat. Cell Biol.* **14**, 1336-1343 (2012).

92. Raffaello, A., De Stefani, D., Sabbadin, D., Teardo, E., Merli, G., Picard, A., Checchetto, V., Moro, S., Szabo, I. & Rizzuto, R. The mitochondrial calcium uniporter is a multimer that can include a dominant-negative pore-forming subunit. *EMBO J.* **32**, 2362-2376 (2013).

93. Sancak, Y., Markhard, A.L., Kitami, T., Kovacs-Bogdan, E., Kamer, K.J., Udeshi, N.D., Carr, S.A., Chaudhuri, D., Clapham, D.E., Li, A.A., Calvo, S.E., Goldberger, O. & Mootha, V.K. EMRE is an essential component of the mitochondrial calcium uniporter complex. *Science* **342**, 1379-1382 (2013).

94. Ohkura, M., Matsuzaki, M., Kasai, H., Imoto, K. & Nakai, J. Genetically encoded bright Ca^{2+} probe applicable for dynamic Ca^{2+} imaging of dendritic spines. *Anal. Chem.* **77**, 5861-5869 (2005).

Acknowledgements

Foremost, I would like to express my gratitude to my advisor, Prof. Masamitsu Iino for the continuous support and kind encouragement throughout my Ph.D. study. Besides my advisor, I am grateful to Dr. Kazunori Kanemaru and Dr. Yohei Okubo for their constructive comments and continuous support on my work. Also I would like to express my thanks to my laboratory colleagues for their technical support and stimulating discussion. I thank the following researchers for providing the plasmid vectors: Dr. Daisuke Ino for pCIS and MCU; Dr. Masamichi Ohkura and Dr. Kuniaki Ishii for cfGCaMP2; Dr. Takeharu Nagai for G-GECO1.1, R-GECO1 and GEM-GECO1; and Dr. Roger Tsien for D1ER. This work was supported by grants from the Ministry of Education, Culture, Sports, Science and Technology, Japan, and Takeda Science Foundation. Most part of the work in this thesis has been published in *Nature Communications* (doi: 10.1038/ncomms5153) or in *The Journal of Neuroscience* (doi: 10.1523/JNEUROSCI.3487-15.2015).

Figure Legends

Figure 1. Construction of CEPIA1*er*.

(**a**) Scatter chart of cfGCaMP2 variants with respect to Ca^{2+} affinity (K_d) and dynamic range (F_{max}/F_{min}). Introduced amino acid substitutions are categorized by color: original cfGCaMP2 (black), substitutions of previously reported ER Ca^{2+} indicators (gray, green and light green), a substitution at single –*Z* position (cyan), substitutions in multiple –*Z* positions (blue), substitutions at F92W and/or D133E (orange), combinational substitutions at –*Z* positions and F92W/D133E (magenta). Data point for CEPIA1*er* is indicated by an arrow. Putative range of Ca^{2+} concentration in the ER is indicated (gray box).

(**b**) In vitro Ca^{2+} titration curves of the recombinant proteins of the original cfGCaMP2 (black) and its variants (gray or green, $n = 58$). For clarity, only the fitted Hill plot curves were shown except for CEPIA1*er*. Putative ranges of Ca^{2+} concentration in the cytosol and ER are indicated (gray boxes).

(**c**) Schematic domain structure of CEPIA1*er*. Four amino acid substitutions (E31D, F92W, E104D and D133E) were introduced to the CaM of cfGCaMP2 (black). ER signal sequence from immunoglobulin heavy-chain variable regions of the mouse and ER retention signal (SEKDEL) were attached at the N and C termini, respectively (gray).

(**d**) Subcellular distribution of CEPIA1*er* and ER-targeted mCherry (with calreticulin signal sequence) in a HeLa cell. Note that the ER-signal sequence in CEPIA1*er* is different from that of mCherry-*er*. The images within the white boxes were expanded.

(**e**) ER Ca^{2+} depletion induced by 3 μM thapsigargin in HeLa cells visualized with CEPIA1*er*. The fluorescence intensity was normalized by the resting value. Representative trace of 20 cells.

(**f**) Oscillatory ER Ca^{2+} dynamics in response to 10 μM histamine stimulation in HeLa cells visualized with CEPIA1*er*. The fluorescence intensity was normalized by the resting value. Representative trace of 49 cells.

Figure 2. Characterization of CEPIA*er*.

(**a**) In vitro Ca^{2+} titration curves of CEPIA1*er* (black solid), G-CEPIA1*er* (green solid), R-CEPIA1*er* (magenta solid), GEM-CEPIA1*er* (blue solid) compared with cfGCaMP2 (black dotted), G-GECO1.1 (green dotted), R-GECO1 (magenta dotted), GEM-GECO1 (blue dotted) and D1ER (orange). Fitted Hill plot curves are shown. Putative ranges of Ca^{2+} concentration in the cytosol and ER are indicated (gray boxes).

(**b–d**) Representative images of HeLa cells expressing G-CEPIA1*er* (**b**), R-CEPIA1*er* (**c**) or GEM-CEPIA1*er* (**b**). Images were compared with the co-expressed ER-targeted mCherry (**b** and **d**) or EGFP (**c**), which were targeted to the ER with calreticulin signal sequence and ER

retention signal. Note that the ER signal sequence in CEPIA*er* is different from that of mCherry-*er* and EGFP-*er*. The images within the white boxes were expanded.

Figure 3. Comparison of amino acid sequences in the CaM domains of CEPIA*er* with those of GCaMP2, cfGCaMP2 and GECOs.

CaM domains of GCaMP2, cfGCaMP2, CEPIA1*er*, G-GECO1.1, G-CEPIA1*er*, R-GECO1, R-CEPIA1*er*, GEM-GECO1 and GEM-CEPIA1*er* were described. The gray boxes indicate the four Ca^{2+} binding loops in the CaM. Amino acids substituted from GCaMP2 are highlighted with colors (magenta, substitutions at *–Z* positions of Ca^{2+} binding loops; orange, F92W or D133E substitutions; blue, substitutions to generate cfGCaMP2; green, substitutions to generate GECOs).

Figure 4. Genealogy of CEPIA variants.

CEPIA1*er*, CEPIA3*mt* and CEPIA4*mt* were generated by introducing amino acid substitutions into the CaM domain of cfGCaMP2. G-CEPIA1*er* was generated by replacing the CaM domain of G-GECO1.1 with that of CEPIA1*er*. For the generation of R-CEPIA1*er*, the CaM domain of R-GECO1 was first replaced with those of cfGCaMP2 variants, and subsequently amino acid substitutions were introduced into the CaM domains of the R-GECO1 variants. GEM-CEPIA1*er* was created by introducing amino acid substitutions into the CaM domain of GEM-GECO1.

Figure 5. Spectral properties of CEPIA*er*.

(**a**) Spectral titration curves of CEPIA*er* at various Ca^{2+} concentrations. The fluorescence intensity was normalized by the maximum intensity. For emission spectra, G-CEPIA1*er*, R-CEPIA1*er* and GEM-CEPIA1*er* were excited at 488, 562 and 395 nm, respectively. For excitation spectra, fluorescence intensity at 512 and 584 nm was obtained for G-CEPIA1*er* and R-CEPIA1*er*, respectively, and at 460 and 510 nm for GEM-CEPIA1*er*.

(**b**) Absorbance spectra of CEPIA*er* (upper panels) and original GECO (lower panels) in Ca^{2+}-containing (5 mM, magenta) or Ca^{2+}-free (1 mM EGTA, black) solution.

Figure 6. In vitro properties of CEPIA*er*.

(**a**) pH titration curves of CEPIA*er*. The fluorescence intensity or ratio was normalized within the maximum and minimum values. pK_a was evaluated by the pH titration in Ca^{2+}-containing (magenta) or Ca^{2+}-free (black) solution. The plots of G-CEPIA1*er*, G-GECO1.1 and R-GECO1 were fitted by a single Hill plot equation. The plots of R-CEPIA1*er*, GEM-CEPIA1*er* and GEM-GECO1 were fitted by a double Hill plot equation. All the extracted parameters are summarized in Table 2.

(**b**) Mg^{2+} titration curves of CEPIA*er* (magenta) compared with Ca^{2+} titration curves (black). The fluorescence intensity was normalized by the values in Mg^{2+} and Ca^{2+} free solution.

(**c**) Ca^{2+} titration of G-CEPIA1*er* (green), R-CEPIA1*er* (magenta) and GEM-CEPIA1*er* (blue) plotted against linear $[Ca^{2+}]_{ER}$ scale. Fitted Hill plot curves are also shown. Putative range of Ca^{2+} concentration in the ER is indicated (gray box).

(**d**) Ca^{2+} titration of CEPIA2–4*mt* plotted against linear Ca^{2+} concentration scale. Fitted Hill plot curves are also shown.

Figure 7. Visualization of ER Ca^{2+} dynamics using CEPIA*er*.

(**a**) Comparison of the responses of CEPIA1*er*, G-CEPIA1*er*, R-CEPIA1*er*, GEM-CEPIA1*er* and D1ER to thapsigargin (3 μM)-induced depletion of ER Ca^{2+} in HeLa cells (mean ± s.e.m., 12–31 cells; ***, $P < 0.001$). Amplitude is defined as the extent of maximum decrease in the fluorescence intensity or ratio after thapsigargin application normalized by the resting value ($\Delta F/F_0$ or $\Delta R/R_0$). For comparison, the response of CEPIA1*er* displayed in Figure 1e is shown (gray).

(**b**) ER Ca^{2+} dynamics in response to histamine (10 μM) measured with CEPIA1*er*, G-CEPIA1*er*, R-CEPIA1*er*, GEM-CEPIA1*er* and D1ER (mean ± s.e.m., 14–103 cells; ***, $P < 0.001$). Amplitude is defined as the maximum decrease in $\Delta F/F_0$ or $\Delta R/R_0$ within 30-s time window after histamine application. For comparison, the response of CEPIA1*er* displayed in Figure 1f is shown (gray).

(**c**) Representative traces of the histamine-induced ER Ca^{2+} dynamics visualized with GEM-CEPIA1*er* in HeLa cells. Absolute $[Ca^{2+}]_{ER}$ (upper) was estimated from the ratio of the green to blue fluorescence intensities (middle and bottom).

(**d**) Cell type-specific variations of absolute $[Ca^{2+}]_{ER}$ measured with GEM-CEPIA1*er*. Box plots for $[Ca^{2+}]_{ER}$ in a variety of cell types before and after agonist stimulation (10 μM histamine for HeLa cells, 30 μM ATP for HEK cells and cultured astrocytes, and 100 nM bradykinin for BHK cells; 4–19 cells) were shown. $[Ca^{2+}]_{ER}$ after agonist stimulation indicated the minimum value reached within 30 s after agonist application. The horizontal line within the box represents the median value, the upper and lower edges of the box represent 75% and 25% values and the whiskers represent the total range.

Figure 8. in situ Ca^{2+} titration of CEPIA*er*.

(**a** and **b**) To determine the Ca^{2+} affinity of CEPIA*er* within the ER, HeLa cells expressing one of CEPIA*er* (G-CEPIA1*er*, R-CEPIA1*er* or GEM-CEPIA1*er*) were permeabilized with 150 μM β-escin in a solution containing 3 μM thapsigargin and 3 μM ionomycin. Then Ca^{2+} concentration in the bathing solution was increased in a stepwise manner. Plots are fitted with a Hill equation. For comparison, the in vitro properties of CEPIA*er* displayed in Table 2 are shown.

Figure 9. CEPIA*er* responses are independent of ER pH dynamics.

(**a**) Representative images of HeLa cells expressing EYFP-*er* (upper), R-CEPIA1*er* (middle) and the merged image (lower). The images within the white boxes were expanded.

(**b**) Simultaneous measurement of EYFP-*er* (green) and R-CEPIA1*er* (gray) in HeLa cells stimulated with 10 μM histamine.

(**c**) pH-dependent change of EYFP-*er* fluorescence intensity in HeLa cells. The cells were first bathed in an acidic solution (pH 6.8) containing monensin (10 μM) and nigericin (10 μM), and subsequently in an alkalinization solution (30 mM NH_4Cl).

(**d**) Summary of EYFP-*er* and R-CEPIA1*er* responses (mean ± s.e.m., 14 cells).

(**e**) Dendrites of EYFP-*er*-expressing Purkinje cells. The magenta circle (10 μm diameter, under the stimulation pipette) indicates the region of interest for panel **f**.

(**f**) The time course of fluorescence intensity change of EYFP-*er* (green) upon PF inputs (ten stimuli at 100 Hz, gray vertical line). For comparison, the fluorescence intensity change of G-CEPIA1*er* displayed in Figure 11b is shown (gray).

(**g**) Summary of PF-induced responses of G-CEPIA1*er* and EYFP-*er*. Amplitude is defined as the maximum decrease in $\Delta F/F_0$ within the 3-s time window after PF stimulation (mean ± s.e.m., eight cells for both G-CEPIA1*er* and EYFP-*er*).

Figure 10. Wave-like propagation of ER Ca^{2+} release visualized with G-CEPIA1*er*.

(**a**) Time-lapse images of wave-like decrease in the ER Ca^{2+} concentration visualized with G-CEPIA1*er*. Perfusion of 10 μM histamine was started at 0 s.

(**b**) Time course of ER Ca^{2+} dynamics along the white line in **a**.

(**c**) Comparison of ER Ca^{2+} dynamics in two regions of interest indicated in **a**. The fluorescence intensity was normalized by the initial intensity. Black line: region 1; green line: region 2.

(**d**) The velocity of ER Ca^{2+} wave measured with G-CEPIA1*er* (mean ± s.e.m., 23 cells) or R-CEPIA1*er* (20 cells). For comparison, the velocity of cytosolic Ca^{2+} wave measured with fluo-4 in cells without (Fluo-4; eight cells) or with R-CEPIA1*er* expression (Fluo-4 + R-CEPIA1*er*; six cells). There was no significant statistical difference among these values (P = 0.93, one-way ANOVA).

Figure 11. Activity-dependent ER Ca^{2+} dynamics in cerebellar Purkinje cells visualized with G-CEPIA1*er*.

(**a**) Representative images of G-CEPIA1*er*-expressing Purkinje cells in the cerebellar slice.

(**b**) PF-induced ER Ca^{2+} dynamics in the dendrites of Purkinje cells. Representative time course of mean $\Delta F/F_0$ within the white circle (indicated in the left image) indicates fluorescence decrease upon PF inputs (ten stimuli at 100 Hz, gray vertical line). The

pseudo-color image that is the average of 10 consecutive frames (indicated as magenta in the time course of $\Delta F/F_0$) shows local dynamics of luminal Ca^{2+}.

(**c**) PF-induced response in a single spine of Purkinje cells. Representative time course of $\Delta F/F_0$ within a spine indicated by the arrow. PF inputs (ten stimuli at 100 Hz, gray vertical line) elicited ER Ca^{2+} release within the spine.

(**d**) Pharmacological characterization of PF-induced ER Ca^{2+} dynamics. G-CEPIA1*er* responses are shown upon PF inputs (five stimuli at 100 Hz, gray vertical line) in the control condition (black); in the presence of LY367385 (100 μM, blue) or NBQX (10 μM, magenta); or after the ER Ca^{2+} depletion with CPA (50 μM, orange).

(**e**) Summary of PF-induced ER Ca^{2+} dynamics. Amplitude is defined as the maximum decrease in $\Delta F/F_0$ within the 3-s time window after PF stimulation (mean ± s.e.m., 7–12 cells).

(**f**) CPA-induced ER Ca^{2+} depletion. The application of 50 μM CPA decreased G-CEPIA1*er* fluorescence with the $\Delta F/F_0$ amplitude of 0.43 ± 0.021 (mean ± s.e.m., six cells).

Figure 12. Simultaneous measurement of Ca^{2+} signals in the ER and cytosol using CEPIA*er* and cytosolic Ca^{2+} indicators.

(**a** and **b**) Simultaneous measurement of Ca^{2+} signals in the ER (G-CEPIA1*er* or R-CEPIA1*er*) and cytosol (fura-2) in HeLa cells stimulated with 10 μM histamine.

(**c**–**f**) Simultaneous Ca^{2+} imaging in the ER (G-CEPIA1*er* or GEM-CEPIA1*er*) and cytosol (R-GECO1) in a HeLa cell (**c**), an astrocyte (**d**), a BHK cell (**e**) or a HEK293A cell (**f**), stimulated with 10 μM histamine (**c**), 30 μM ATP (**d** and **f**) or 100 nM bradykinin (**e**), respectively.

(**g** and **h**) Simultaneous Ca^{2+} imaging in the ER (R-CEPIA1*er*) and cytosol using G-GECO1.1 (**g**) or GEM-GECO1 (**h**) in HeLa cells stimulated with 10 μM histamine.

Figure 13. Evaluation of bleed-through of CEPIA, GECO and fura-2.

(**a**) Representative traces of fluorescence intensity changes in response to histamine application at six pairs of excitation and emission wavelengths (472/520, 562/641, 377/466, 377/520, 340/510 and 365/510 nm) in HeLa cells expressing one of the genetically encoded indicators or loaded with fura-2. Autofluorescence was subtracted.

(**b**) Comparisons of the resting and agonist-induced peak fura-2 ratios among the cells expressing G-CEPIA1*er* (green; mean ± s.e.m., 18 cells), R-CEPIA1*er* (magenta; 25 cells), CEPIA2*mt* (light green; 16 cells) and cells without CEPIA expression (gray; 68 cells). There were no significant differences in the resting and peak fura-2 ratios. $P = 0.51$ and 0.40, one-way ANOVA.

Figure 14. Visualization of ER and cytosolic Ca^{2+} dynamics during store-operated Ca^{2+} entry (SOCE).

(**a** and **b**) Ca^{2+} dynamics in the ER (lower panels) and cytosol (upper panels) during SOCE. After histamine (10 μM)-induced Ca^{2+} release in the absence of extracellular Ca^{2+}, SOCE was induced by "Ca^{2+} add back", the reintroduction of Ca^{2+} in the extracellular solution (black). To evaluate the contribution of SERCA-dependent Ca^{2+} uptake by the ER, CPA was applied as indicated to the extracellular solution (**a**, magenta). The ER Ca^{2+} refilling was inhibited by Gd^{3+} (10 μM), an inhibitor of Orai1, during "Ca^{2+} add back" (**b**, magenta).

(**c**) Magnified $[Ca^{2+}]_{cyt}$ traces during "Ca^{2+} add back" in the upper panel of **b**.

(**d**) Changes in the ER Ca^{2+} refilling rate and $[Ca^{2+}]_{cyt}$ in response to "Ca^{2+} add back" with or without Gd^{3+} application. Left, the slope of linear fitting to the G-CEPIA1*er* fluorescence change during the intervals T_1 to T_3 in **b** (lower panel) was obtained, and the indicated differences are shown. Right, the average $[Ca^{2+}]_{cyt}$ during the intervals T_1 to T_3 in **b** (upper panel) and **c** was obtained, and the indicated differences are shown (mean ± s.e.m., 35 cells for control and 42 cells for Gd^{3+}; ***, $P < 0.001$.)

(**e**) Time courses of cytosolic (upper panel) and ER (lower panel) Ca^{2+} responses to thapsigargin (3 μM) treatment in HeLa cells in the absence of extracellular Ca^{2+}, and to subsequent "Ca^{2+} add back" in the extracellular solution.

(**f**) Time courses of cytosolic (upper panel) and ER (lower panel) Ca^{2+} responses to anti-human CD3ε monoclonal antibody (1 μg/ml, R&D systems, USA) treatment in Jurkat T

cells in the absence of extracellular Ca^{2+}, and to subsequent "Ca^{2+} add back" in the extracellular solution.

Figure 15. Simultaneous imaging of STIM1 localization and Ca^{2+} concentration in the ER and cytosol.

(**a**) Simultaneous imaging of STIM1 dynamics, ER Ca^{2+} level and cytosolic Ca^{2+} concentration using mCherry-STIM1, G-CEPIA1*er* and fura-2, respectively. Time courses of cytosolic Ca^{2+} concentration (blue), ER Ca^{2+} dynamics (green) and the number of mCherry-STIM1 puncta normalized with the minimum and maximum (magenta). As $[Ca^{2+}]_{ER}$ was depleted with histamine stimulation in the Ca^{2+}-free solution, mCherry-STIM1 formed puncta. After Ca^{2+} addback in the external solution, $[Ca^{2+}]_{ER}$ gradually recovered and mCherry-STIM1 puncta disappeared. The slope of linear fitting to the G-CEPIA1*er* fluorescence change and the average $[Ca^{2+}]_{cyt}$ change during the time interval between T_1 to T_2 (shown in **a**) were calculated.

(**b**) The images of fura-2 (upper), G-CEPIA1*er* (middle) and mCherry-STIM1 (lower) at four time points indicated in **a** as gray dotted lines. The expanded images of mCherry-STIM1within the white boxes were shown.

(**c**) The normalized number of mCherry-STIM1 puncta was plotted against normalized G-CEPIA1*er* fluorescence (F/F_0) during puncta formation (black) and dissociation (magenta). The relationship between $[Ca^{2+}]_{ER}$ and puncta formation can be fitted by a Hill equation with

a Hill coefficient of 8.7 ± 1.1 and a $K_{1/2}$ of 0.37 ± 1.1 for puncta formation, and 6.8 ± 0.6 and 0.60 ± 0.04 for puncta dissociation (mean ± s.e.m., six cells).

(**d**) Comparison of the ER Ca^{2+} refilling rate and $[Ca^{2+}]_{cyt}$ in response to "Ca^{2+} add back" between STIM1-expressing cells and control cells. Left, the slope of linear fitting to the G-CEPIA1*er* fluorescence change during the time interval between T_1 to T_2 in **a** (middle panel) was shown. Right, the average $[Ca^{2+}]_{cyt}$ change during the time interval between T_1 to T_2 in **a** (upper panel) was shown. Mean ± s.e.m., 35 cells for control and six cells for STIM1-expressing cells; ***, $P < 0.001$.

Figure 16. Simultaneous imaging of STIM1 localization and absolute ER Ca^{2+} concentration.

(**a**) The images of GEM-CEPIA1*er* (upper) and mCherry-STIM1 (middle) at three time points indicated in **b** as gray dotted lines (T_1, T_2 and T_3). The expanded images of mCherry-STIM1within the white boxes were shown in the lower panels.

(**b**) Time courses of ER Ca^{2+} concentration (blue) and the number of mCherry-STIM1 puncta normalized with the minimum and maximum (magenta). As $[Ca^{2+}]_{ER}$ was depleted with histamine stimulation in the Ca^{2+}-free solution, mCherry-STIM1 formed puncta (T_2). After Ca^{2+} addback in the external solution, $[Ca^{2+}]_{ER}$ gradually recovered and mCherry-STIM1 puncta disappeared (T_3).

(**c**) The normalized number of mCherry-STIM1 puncta was plotted against ER Ca^{2+} concentration during puncta formation (black) and dissociation (magenta). The plots obtained from three independent experiments were overlaid. The relationship between $[Ca^{2+}]_{ER}$ and puncta formation can be fitted by a Hill equation with a Hill coefficient of 7.9 and a $K_{1/2}$ of 350 μM for puncta formation, and 9.7 and 530 μM for puncta dissociation.

Figure 17. Intercellular heterogeneity of mitochondrial Ca^{2+} signal visualized with CEPIA.

(**a**) Ca^{2+} titration curves of three mitochondria-targeted CEPIA variants (CEPIA2*mt*, K_d = 160 nM, F_{max}/F_{min} = 1.7; CEPIA3*mt*, 11 μM, 1.6; CEPIA4*mt*, 56 μM, 1.5). The measurements were performed at pH 8.0.

(**b**) Representative images of HeLa cells expressing CEPIA2*mt* (left) co-stained with MitoTracker Red (middle). The merged images are shown in the right panels. The areas within the white boxes were expanded (lower).

(**c**) Representative traces of CEPIA2*mt* fluorescence upon histamine (10 μM) application in HeLa cells pre-stimulated with DMSO (gray) or FCCP (magenta, 500 nM; Abcam, USA).

(**d**) Summary of CEPIA2*mt* response. Amplitude is defined as the extent of maximum increase in the fluorescence intensity after histamine application normalized by the resting value ($\Delta F/F_0$). Mean ± s.e.m.; 11 cells for vehicle only (DMSO) and 15 cells for FCCP.

(**e**) Representative traces of mitochondrial Ca^{2+} dynamics upon stimulation with histamine (10 μM) in HeLa cells. To enhance mitochondrial Ca^{2+} signal, rat MCU was extrinsically expressed (+MCU, blue), or the inhibitor of Na^{+}/Ca^{2+} exchanger CGP-37157 (10 μM; Enzo Life Sciences, USA) was applied (+CGP, magenta).

(**f**) The percentage of cells showing mitochondrial Ca^{2+} responses upon histamine application measured with CEPIA2–4*mt* among control HeLa cells, MCU-expressing cells (+MCU) and CGP-37157-pretreated cells (+CGP).

(**g**) Mitochondrial Ca^{2+} responses measured with CEPIA2–4*mt* during histamine (10 μM) stimulation were compared among control HeLa cells (67, 45 and 35 cells), MCU-expressing cells (26, 28 and 22 cells) and CGP-37157-pretreated cells (19, 24 and 16 cells). The response patterns were classified into five groups: rapid increase followed by slow decay (green), saturated response (magenta), sustained increase without saturation (orange), oscillatory response (blue) and no response (gray).

Figure 18. Subcellular heterogeneity of mitochondrial Ca^{2+} signal visualized with CEPIA*mt*.

Mitochondrial Ca^{2+} signals visualized with subcellular resolution using CEPIA3*mt* (**a–c**) or CEPIA2*mt* (**d–f**). (**a** and **d**) Upper, fluorescence images of HeLa cell expressing CEPIA3*mt* (**a**) or CEPIA2*mt* (**d**). Lower, the areas within the white boxes were expanded.

(**b** and **e**) Time courses of mitochondrial Ca^{2+} signal during histamine (10 μM) application and subsequent ionomycin (3 μM) stimulation within the two regions of interest shown in **a** and **d**. Time courses averaged over the entire cell were also shown (Global).

(**c** and **f**) Upper, averaged fluorescence images at resting state (left), after histamine application (middle) and after ionomycin application (right) were indicated. Lower, time-dependent changes in the fluorescence intensity were shown in pseudo-color.

Figure 19. Simultaneous Ca^{2+} imaging in the ER, mitochondria and cytosol during heterogeneous mitochondrial Ca^{2+} signal.

(**a**) Fluorescence images of a HeLa cell expressing G-CEPIA1*er* (green) and mitochondria-localized R-GECO1 (R-GECO1*mt*, magenta). The area within the white box was expanded (right).

(**b**) Time courses of Ca^{2+} signal in the mitochondria, ER and cytosol in a HeLa cell stimulated with 10 μM histamine within the two regions of interest indicated in **a**. Time courses averaged over the entire cell were also shown (Global).

(**c**) The images of R-GECO1*mt* (magenta) and G-CEPIA1*er* (green) at three time points were shown. Perfusion of 10 μM histamine was started at 0 s. Representative images of six cells.

Figure 20. Evaluation of heterogeneity in mitochondrial matrix pH and mitochondrial inner membrane potential during heterogeneous mitochondrial Ca^{2+} signal.

(**a**) Representative images of HeLa cells expressing R-GECO1*mt* (upper) and a mitochondria-targeted pH indicator SypHer-dmito (lower). The regions within the white boxes were expanded (right).

(**b**) Time courses of R-GECO1*mt* (upper) and SypHer-dmito (lower) upon histamine (10 μM) stimulation within the two regions of interest indicated in **a**.

(**c**) Representative trace of pH dependent change of SypHer-dmito fluorescence ratio in the region 1 indicated in **a**. The cells expressing SypHer-dmito were alkalinized with a solution containing 30 mM NH_4Cl.

(**d**) Summary of SypHer-dmito responses. Mitochondria showing Ca^{2+} signal upon histamine stimulation were analyzed. $\Delta R/R_0$ after histamine and NH_4Cl stimulation were indicated (mean ± s.e.m., 89 and 365 mitochondria, respectively).

(**e**) Representative images of HeLa cells expressing mitochondria-localized GEM-GECO1 (GEM-GECO1*mt*, upper) co-stained with JC-1 (Cayman Chemical, UK), an indicator of mitochondrial membrane potential (lower). The regions within the white boxes were expanded (right).

(**f**) Time courses of GEM-GECO1*mt* (upper) and JC-1 (lower) upon histamine (10 μM) stimulation within the two regions of interest indicated in **e**.

(**g**) Summary of JC-1 ratio in the mitochondria responding with (mean ± s.d., 69 mitochondria) or without (327 mitochondria) an increase in Ca^{2+} concentration upon histamine stimulation. The values within 6-s time window before (gray, Resting) and after (black, +His) histamine application were analyzed.

Table 1. CEPIA library.

a. cfGCaMP2 variants

Mutated amino acids	Dynamic range	Hill coeff.	K_d (μM)
Original (CEPIA2*mt*)	5.1	2.5	0.67
■ Substitutions used in previously reported ER Ca^{2+} indicators			
E11K/E84R/E87K (D1ER)	2.6	0.9	14.5
E31Q (YC4er)	2.5	0.5	64.9
E104Q (YC3er)	3.4	3.7	1.2
■ Single substitution at *–Z* position			
E31D (split-YC7.3er, CEPIA3*mt*)	5.0	1.5	14.5
E67D	4.7	1.4	9.2
E104D	3.8	4.2	0.99
E140D	4.4	3.7	2.1
■ Double substitutions at *–Z* positions			
E31D/E67D	2.6	1.3	470
E31D/E104D	4.1	1.5	20.7
E31D/E140D	4.7	2.0	23.5
E67D/E104D	4.3	1.5	17.9
E67D/E140D	4.7	2.1	23.9
E104D/E140D	4.2	1.2	24.4
■ Triple substitutions at *–Z* positions			
E31D/E104D/E140D	3.2	1.9	135
E67D/E104D/E140D	3.6	2.2	129
■ Substitutions at F92W and/or D133E			
F92W	4.5	3.3	0.90
D133E	4.3	4.7	2.1
F92W/D133E	4.6	3.0	10.3
■ F92W/D133E and single substitutions at *–Z* positions			
E31D/F92W/D133E (CEPIA4*mt*)	4.9	1.7	90.2
E67D/F92W/D133E	4.9	2.3	75.2
F92W/E104D/D133E	3.5	1.3	130
F92W/D133E/E140D	4.5	0.9	67.4
■ F92W/D133E and double substitutions at *–Z* positions			
E31D/F92W/E104D/D133E (CEPIA1*er*)	4.2	1.3	368
E31D/F92W/D133E/E140D	3.5	1.8	411
E67D/F92W/D104D/D133E	4.1	1.9	344
E67D/F92W/D133E/D140D	4.4	1.7	276
F92W/E104D/D133E/E140D*	1.3,2.7	1.9, 1.4	3.7, 1,540
■ D133E and single substitutions at *–Z* positions			
E31D/D133E	5.0	2.2	33.2
E67D/D133E	5.0	2.4	31.1
E104D/D133E	3.5	1.2	43.8
D133E/E140D	4.5	2.2	8.2
■ D133E and double substitutions at *–Z* positions			
E31D/E104D/D133E	4.2	2.0	201
E31D/D133E/E140D	4.7	1.8	92.2
E67D/E104D/D133E	4.1	2.2	154
E67D/D133E/E140D	4.4	1.9	93.4
E104D/D133E/E140D*	1.3, 3.1	1.7, 1.3	4.8, 661
■ Other substitutions			
E11K	2.1	3.6	1.4
E84R/E87K	3.3	2.8	1.2
E31A	1.9	0.8	15.2
E31Q/D133E	2.2	0.6	109
E67D/E104Q	4.2	1.4	43.7
E104Q/E140D	3.1	0.8	23.8
E31Q/F92W/D133E	2.1	0.3	1,730
F92W/E104Q/D133E*	1.5, 1.4	2.0, 0.9	4.3, 6,100
E31D/F92W/E104Q/D133E	1.8	0.6	13,400
E67D/F92W/E104Q/D133E	2.4	0.7	2,330
F92W/S101D/D133E	5.1	3.2	7.0
F92W/D95N/N97D/D133E	4.9	3.2	8.2
F92W/D95N/S101D/D133E	4.3	2.7	11.1
E31D/L36M	4.0	1.1	22.4
E31D/L36M/E67D	2.8	1.2	873
E31D/L36M/E104D	4.0	1.5	25.0
E31D/L36M/E140D	4.9	2.0	26.1
E31D/L36M/E104Q	3.8	1.5	45.2
T26G/E31D/L36M	4.6	0.9	2.4
E31D/L36M/Q41L	3.9	1.3	15.1
E31D/L36M/K75I	3.7	1.2	9.2
E31D/L36M/Q41L/K75I	3.1	1.1	8.9

b. R-GECO1 variants with cfGCaMP2 CaM

Mutated amino acids	Dynamic range	Hill coeff.	K_d (μM)
E31D/E67D	17.6	1.2	152
E31D/F92W/D133E	21.9	2.3	16.6
E31D/E104D/D133E	19.8	2.7	26.3
E104D/D133E/E140D	12.5	1.4	50.8
E31D/E67D/F92W/D133E	17.2	1.2	211
E31D/F92W/E104D/D133E	16.9	2.3	70.9
E67D/F92W/D133E/E140D	17.6	2.1	20.0
F92W/E104D/D133E/E140D	14.9	1.0	123
E31D/E67D/F92W/E104D/D133E (R-CEPIA1*er*)	8.8	1.7	565

c. G-GECO1.1 variants with cfGCaMP2 CaM

Mutated amino acids	Dynamic range	Hill coeff.	K_d (μM)
E31D/F92W/D133E	10.2	1.5	209
E31D/F92W/E104D/D133E (G-CEPIA1*er*)	4.7	1.9	672
E31D/E67D/F92W/E104D/D133E	3.8	0.5	3,860

d. GEM-GECO1 variants with cfGCaMP2 CaM

Mutated amino acids	Dynamic range	Hill coeff.	K_d (μM)
E31D/F92W/E104D/D133E	1.1	n.d.	n.d.
E31D/E67D/F92W/E104D/D133E	1.2	n.d.	n.d.

e. GEM-GECO1 variants with original CaM

Mutated amino acids	Dynamic range	Hill coeff.	K_d (μM)
Original	67.5	2.6	0.31
E31D	23.7	1.2	7.2
E31D/E67D	13.0	1.2	97.1
E31D/D133E	41.3	2.4	36.4
E31D/E140D	43.6	2.2	24.2
E31D/F92W/D133E	11.2	1.9	90.0
E31D/E104D/D133E	20.8	1.7	89.7
E31D/D133E/E140D	24.8	1.6	147
E31D/F92W/E104D/D133E	8.1	2.1	225
E31D/F92W/D133E/E140D (GEM-CEPIA1*er*)	21.7	1.4	558
E31D/E104D/D133E/E140D	34.8	1.5	483
E31D/E67D/F92W/D133E/E140D	1.4	1.1	602
E31D/F92W/E104D/D133E/E140D	2.3	1.0	2,010

CEPIA library generated in the present study. The properties of CEPIA variants that were used in the intraorganellar Ca^{2+} imaging are highlighted (magenta). cDNAs were confirmed by sequencing.

*Ca^{2+} titration curves were obtained by fitting with a double Hill plot equation.

Table 2. Properties of CEPIA variants.

Probe	Ca^{2+}	ε (mM^{-1} cm^{-1}) (λ_{ABS}*)	λ_{Ex}*	Φ (λ_{Em}*)	Brightness† (mM^{-1} cm^{-1})	pK_a‡	Dynamic range§	K_d for Ca^{2+}	Hill coefficient
G-CEPIA1*er*	−	36 (402), 3 (498)	499	0.19 (512)	0.5	8.7	4.7 ± 0.3‖	672 ± 23 μM‖	1.95 ± 0.07‖
	+	33 (401), 10 (497)	498	0.40 (511)	3.4	8.0			
G-GECO1.1	−	35 (401), 2 (500)	499	0.20 (514)	0.4	8.8	14.7 ± 1.6	363 ± 4 nM	3.38 ± 0.10
	+	24 (397), 26 (497)	498	0.46 (513)	10.5	7.4			
R-CEPIA1*er*	−	25 (445), 5 (576)	570	0.09 (593)	0.5	8.9	8.8 ± 0.7	565 ± 58 μM	1.70 ± 0.04
	+	15 (448), 35 (562)	561	0.18 (584)	6.2	6.5, 9.0			
R-GECO1	−	27 (445), 7 (576)	565	0.06 (594)	0.4	8.9	15.6 ± 4.1	142 ± 17 nM	2.05 ± 0.12
	+	58 (562)	560	0.20 (584)	11.6	6.4			
GEM-CEPIA1*er*	−	36 (401)	381, 395	0.26 (510)	9.4	6.1	21.7 ± 0.6	558 ± 14 μM	1.37 ± 0.01
	+	36 (391)	381, 394	0.21 (462)	7.6	6.5, 10.6			
GEM-GECO1	−	34 (395)	387, 395	0.31 (510)	10.7	6.1	67.5 ± 10.9	306 ± 0.4 nM	2.55 ± 0.02
	+	35 (391)	387, 390	0.18 (462)	6.2	6.1, 10.1			

*λ_{ABS}, λ_{Ex}, λ_{Em} are the maximum wavelength of absorption, fluorescence excitation and fluorescence emission spectra, respectively.

†Brightness is the product of molar extinction coefficient (ε) and quantum yield (Φ).

‡pK_a is determined as the pH at half-maximal fluorescence intensity calculated by fitting each plots to Hill equations. As for R-CEPIA1*er*, GEM-GECO1 and GEM-CEPIA1*er*, pK_a is calculated by a double Hill equation (See Materials and Methods).

§Dynamic range indicates the ratio of the maximum to minimum fluorescence intensity (F_{max}/F_{min}) or fluorescence ratio (R_{max}/R_{min}) (See Materials and Methods).

‖Mean ± s.e.m.

Table 3. The list of primers and oligonucleotides.

Primer number		Sequence
1		ATAAGCATATGCAGGTCCAACTGCAGGGAT
2		ATTAGATCTCTACAGCTCGTCCTTCTCGCT
3		AGAGGATCCATGGTCGACTCTTCACGTCGT
4		TAGCGGCCGCCTTCGCTGTCATCATTTGTA
5		GAGACCAACTGACTGAAGAGCAGATCGCAG
6		GAGTAGCCTCCCAGCCCATGGTCTTCTTCT
7		GCAACACTCGAGACCAACTGACTGAAGAGC
8	(E11K)	GCTGACTGAAGAGCAGATCGCAAAATTTAA
9	(E11K)	TGGTCACGCGTGTTGTACTCCAGCTT
10	(E31D)	GGGCAGAACCCCACAGAAGCAGAGCTCCAG
11	(E31D)	CAGAGACCGCAGCACCGTCCCCAGATCCTT
12	(E31D)	CAGAGACCGCATCACCGTCCCCAGATCCTT
13	(E31Q)	CTGGGGACGGTGCTGCGGTCTCT
14	(E31Q)	CTGCTTGGTTGTTATTGTCCCATCCCCGTC
15	(E67D)	GACAATGATGGCAAGAAAAATGAAAGACAC
16	(E67D)	GACGATGATGGCAAGAAAAATGAATGACAC
17	(E67D)	GACAATGATGGCACCTAAAATGCAGGACAC
18	(E67D)	AGGAAATCAGGGAAGTCGATTGTGCCATTA
19	(E67D)	AGGAAATCAGGGAAGTCGAAGGTACCGTCA
20	(E67D)	AGGAAATCAGGGAAGTCGATGGTACCGTCA
21	(E84R/E87K)	AATTCGAAAAGCGTTCCGTGTGTTTGATAA
22	(E84R/E87K)	CTTTCTTCACTGTCTGTGTCTTTCATTTTT
23	(F92W)	GGGATAAGGATGGCAATGGCTACATCAGT
24	(F92W)	ACACACGGAACGCTTCGCGAATTTCTTCT
25	(F92W)	GGGATAAGGATGGCAATGGCTACATCGGC
26	(E104D)	AGCAGACCTTCGCCACGTGATGACAAACCT
27	(E104D)	AGCAGATCTTCGCCACGTGATGACAAACCT
28	(E104D)	AGCAGATCTTCGCCACGTGATGACAGACCT
29	(E104D)	GCGCCGATGTAGCCATTGCCGTCCTTATC
30	(E104Q)	GCAGAGATGTAGCCATTGCCATCCTTATC
31	(E104Q)	AGCACAGCTTCGCCACGTGATGACAAACCT
32	(D133E)	ATCGATGGAGAAGGTCAGGTAAACTACGAA
33	(D133E)	ATCTGCTTCCCTGATCATTTCATCAACCTC
34	(D133E)	GTCTGCTACCCTGATCATTTCATCAACCTC
35	(E140D)	ATGATGACAGCGAAGGCGGCCGCAGAACAA
36	(E140D)	TTGTACAAAGTCTTCGTAGTTTACCTGACC
37		AGGGATCCATGCGGGGTTCTCATCATCATC
38		GGGATCCATCATCATCATCG
39		TCGACGATGATGATGATGGATCCCTGCA
40		CGCGCCAAAATTCATTCACTGGGGGACCCC
41		ATGAGCGTGCTCACCCCACTCCTGCTGCGGGGGCTGACCG
42		GCAGCGCTAGGCGGCTGCCAGTCCCGCGG
43		GCCAAGATCCACAGTCTCGGCGATCCCG
44		TCATGGGGTCCCCCAGTGAATGAATTTTGG
45		CTGCCGGTCAGCCCCCGCAGCAGGAGTGGGGTGAGCACGC
46		TGGCCCGCGGGACTGGCAGCCGCCTAGCG
47		GATCCGGGATCGCCGAGACTGTGGATCT
48		ATAAGCTTGCCACCATGGGATGGAGCTGTA
49		AGAACTAGTCTACAGCTCGTCCTTCTCGCT
50		GATCCATGCTGCTGCCCGTCCCCCTGCTGC
51		TGGGCCTGCTGGGCGCCGCCGCCGACATGG
52		CCCAGCAGCAGGGGGACGGGCAGCAGCATG
53		TCGACCATGTCGGCGGCGGCGCCCAGCAGG
54		AAACCGCGGACATGGTGAGCAAGGGCGAGG
55		GACGAATTCTTACAGCTCGTCCTTCTTGTACAGCTCGTCCATGC
56		AAGCCGCGGACATGGTGAGCAAGGGCGAGG
57		GCCGAATTCTTACAGCTCGTCCTTCTTGTACAGCTCGTCCATGC
58		CCGGGCGAATTCGGCAGATATCCATCACAC
59		GATGATGATGGGATCCTCTCATGTCCGCGG
60		CTCGGATCCATGGTGAGCAAGGGCGAGGAG
61		TTAATGCGGCCGCGCCGAGAGTGATCCCGG
62		TGTCTGCAGGCTACAACAGCGACAACGTCT
63		TTGCCTGATCGCGCAAAGAGTGACCATCTT
64		ATATCTAGAGCCACCATGGATGTGTGCGCC
65		CGCCTCTAGACTACTTCTTAAGAGGCTTCT
66		CTTGTACAGCTCGTCCATGCCGCCGGTGGA

The primers and oligonucleotides used in the present study are listed. For the primers used for site-directed mutagenesis, the target mutation sites are indicated in parentheses.

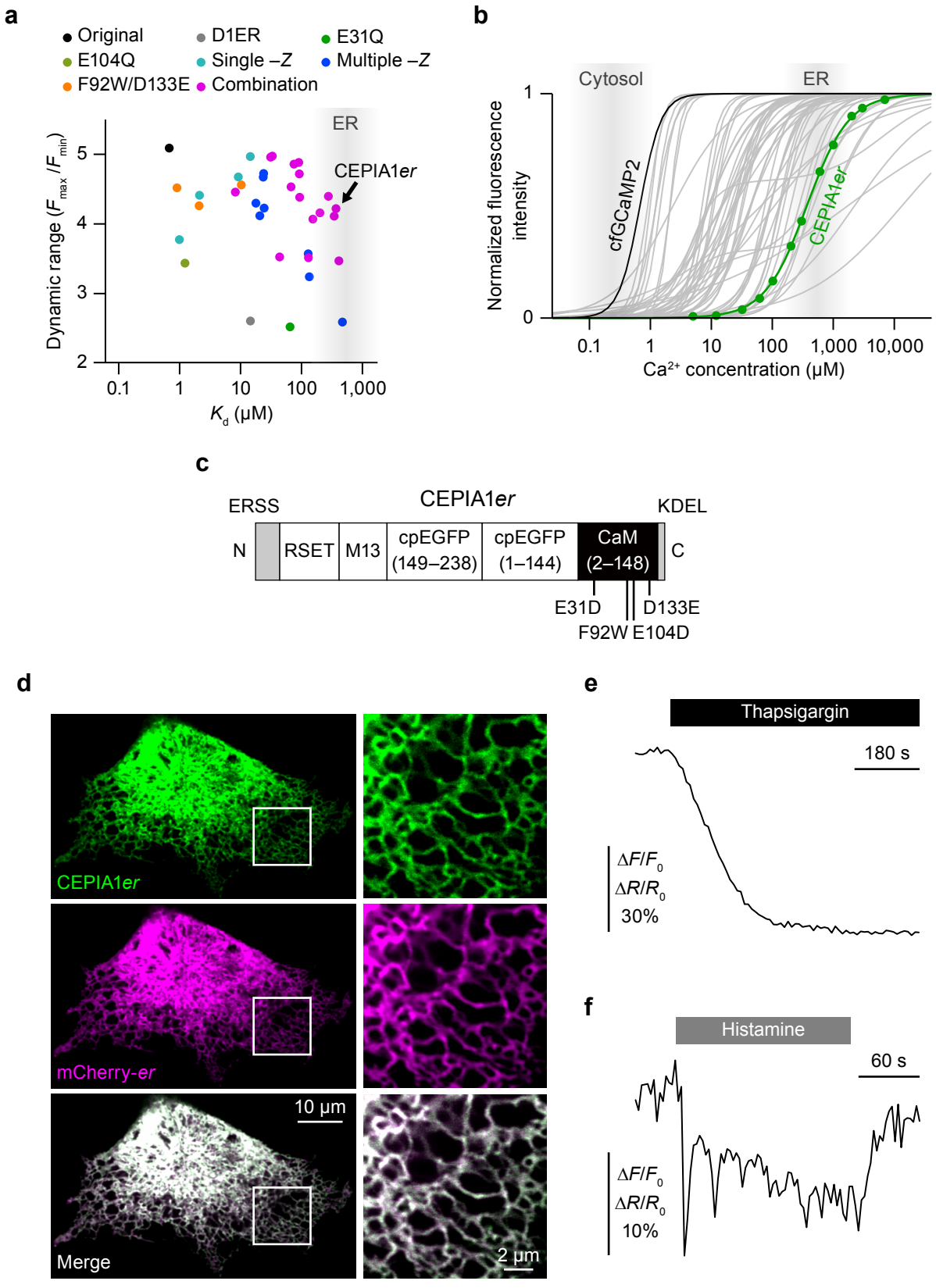
a
Original
D1ER
E31Q
E104Q
Single –Z
Multiple –Z
F92W/D133E
Combination
ER
CEPIA1er
Dynamic range (F_{max}/F_{min})
K_d (μM)
b
Cytosol
ER
Normalized fluorescence intensity
cfGCaMP2
CEPIA1er
Ca2+ concentration (μM)
c
CEPIA1er
ERSS
KDEL
N
RSET
M13
cpEGFP (149–238)
cpEGFP (1–144)
CaM (2–148)
C
E31D
D133E
F92W
E104D
d
CEPIA1er
mCherry-er
Merge
10 μm
2 μm
e
Thapsigargin
180 s
ΔF/F0
ΔR/R0
30%
f
Histamine
60 s
ΔF/F0
ΔR/R0
10%

Figure 1

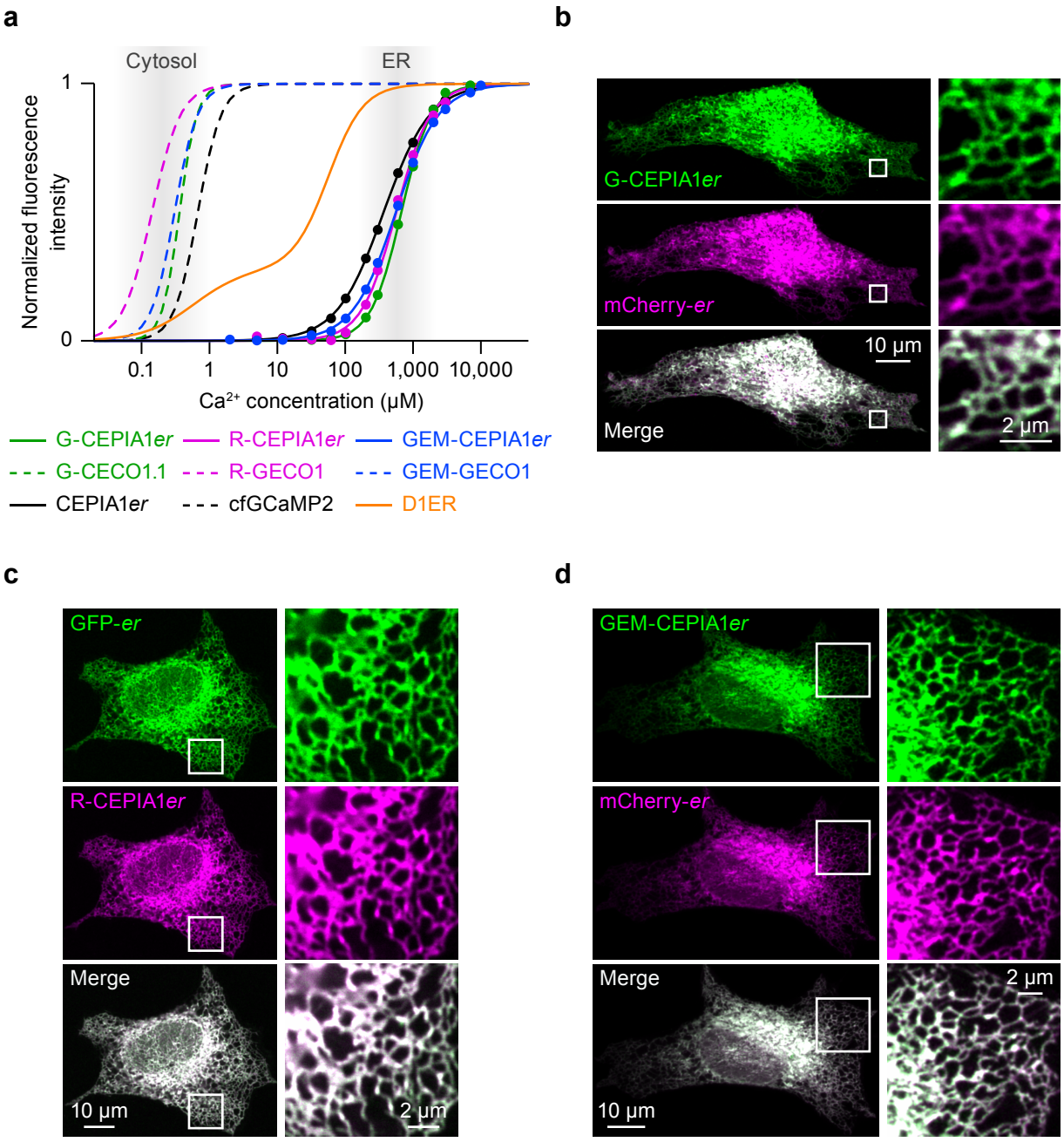
a
Cytosol
ER
Normalized fluorescence intensity
1
0
0.1
1
10
100
1,000
10,000
Ca²⁺ concentration (μM)
G-CEPIA1er
R-CEPIA1er
GEM-CEPIA1er
G-CECO1.1
R-GECO1
GEM-GECO1
CEPIA1er
cfGCaMP2
D1ER
b
G-CEPIA1er
mCherry-er
Merge
10 μm
2 μm
c
GFP-er
R-CEPIA1er
Merge
10 μm
2 μm
d
GEM-CEPIA1er
mCherry-er
Merge
10 μm
2 μm

Figure 2

Substitutions at –Z positions | F92W/D133E substitutions | Derived from cfGCaMP2 | Derived from GECOs

																				Ca²⁺ binding Loop I									
																				+X		+Y		+Z		–Y		–X		
	1	2	3	4	5	6	7	8	9	10	11	12	13	14	15	16	17	18	19	20	21	22	23	24	25	26	27	28	29	30
GCaMP2		D	Q	L	T	E	E	Q	I	A	E	F	K	E	A	F	S	L	F	D	K	D	G	D	G	T	I	T	T	K
cfGCaMP2		D	Q	L	T	E	E	Q	I	A	E	F	K	E	A	F	S	L	F	D	K	D	G	D	G	T	I	T	T	K
CEPIA1*er*		D	Q	L	T	E	E	Q	I	A	E	F	K	E	A	F	S	L	F	D	K	D	G	D	G	T	I	T	T	K
G-GECO1.1		D	Q	L	T	E	E	Q	I	A	E	F	K	E	A	F	S	L	F	D	K	D	G	D	G	T	I	T	T	K
G-CEPIA1*er*		D	Q	L	T	E	E	Q	I	A	E	F	K	E	A	F	S	L	F	D	K	D	G	D	G	T	I	T	T	K
R-GECO1		D	Q	L	T	E	E	Q	I	A	E	F	K	E	A	F	S	L	F	D	K	D	G	D	G	T	I	T	T	K
R-CEPIA1*er*		D	Q	L	T	E	E	Q	I	A	E	F	K	E	A	F	S	L	F	D	K	D	G	D	G	T	I	T	T	K
GEM-GECO1		D	Q	L	T	E	E	Q	I	A	E	F	K	E	A	F	S	L	F	D	K	D	G	D	G	T	I	T	T	K
GEM-CEPIA1*er*		D	Q	L	T	E	E	Q	I	A	E	F	K	E	A	F	S	L	F	D	K	D	G	D	G	T	I	T	T	K

																										Ca²⁺ binding Loop II				
	–Z																									+X		+Y		+Z
	31	32	33	34	35	36	37	38	39	40	41	42	43	44	45	46	47	48	49	50	51	52	53	54	55	56	57	58	59	60
GCaMP2	E	L	G	T	V	M	R	S	L	G	Q	N	P	T	E	A	E	L	Q	D	M	I	N	E	V	D	A	D	G	N
cfGCaMP2	E	L	G	T	V	L	R	S	L	G	Q	N	P	T	E	A	E	L	Q	D	M	I	N	E	V	D	A	D	G	N
CEPIA1*er*	D	L	G	T	V	L	R	S	L	G	Q	N	P	T	E	A	E	L	Q	D	M	I	N	E	V	D	A	D	G	N
G-GECO1.1	E	L	G	T	V	M	R	S	L	G	Q	N	P	T	E	A	E	L	Q	D	M	I	N	E	V	D	A	D	G	D
G-CEPIA1*er*	D	L	G	T	V	L	R	S	L	G	Q	N	P	T	E	A	E	L	Q	D	M	I	N	E	V	D	A	D	G	N
R-GECO1	E	L	G	T	V	M	R	S	L	G	Q	N	P	T	E	A	E	L	Q	D	M	I	N	E	V	D	A	D	G	D
R-CEPIA1*er*	D	L	G	T	V	L	R	S	L	G	Q	N	P	T	E	A	E	L	Q	D	M	I	N	E	V	D	A	D	G	N
GEM-GECO1	E	L	G	T	V	M	R	S	L	G	Q	N	P	T	E	A	E	L	Q	D	M	I	N	E	V	D	A	D	G	D
GEM-CEPIA1*er*	D	L	G	T	V	M	R	S	L	G	Q	N	P	T	E	A	E	L	Q	D	M	I	N	E	V	D	A	D	G	D

		–Y		–X			–Z																							
	61	62	63	64	65	66	67	68	69	70	71	72	73	74	75	76	77	78	79	80	81	82	83	84	85	86	87	88	89	90
GCaMP2	G	T	I	D	F	P	E	F	L	T	M	M	A	R	K	M	K	D	T	D	S	E	E	E	I	R	E	A	F	R
cfGCaMP2	G	T	I	D	F	P	E	F	L	T	M	M	A	R	K	M	K	D	T	D	S	E	E	E	I	R	E	A	F	R
CEPIA1*er*	G	T	I	D	F	P	E	F	L	T	M	M	A	R	K	M	K	D	T	D	S	E	E	E	I	R	E	A	F	R
G-GECO1.1	G	T	I	D	F	P	E	F	L	T	M	M	A	R	K	M	N	D	T	D	S	E	E	E	I	R	E	A	F	R
G-CEPIA1*er*	G	T	I	D	F	P	E	F	L	T	M	M	A	R	K	M	K	D	T	D	S	E	E	E	I	R	E	A	F	R
R-GECO1	G	T	F	D	F	P	E	F	L	T	M	M	A	R	K	M	N	D	T	D	S	E	E	E	I	R	E	A	F	R
R-CEPIA1*er*	G	T	I	D	F	P	D	F	L	T	M	M	A	R	K	M	K	D	T	D	S	E	E	E	I	R	E	A	F	R
GEM-GECO1	G	T	I	D	F	P	E	F	L	T	M	M	A	P	K	M	Q	D	T	D	S	E	E	E	I	R	E	A	F	R
GEM-CEPIA1*er*	G	T	I	D	F	P	E	F	L	T	M	M	A	P	K	M	Q	D	T	D	S	E	E	E	I	R	E	A	F	R

			Ca²⁺ binding Loop III																											
			+X		+Y		+Z		–Y		–X			–Z																
	91	92	93	94	95	96	97	98	99	100	101	102	103	104	105	106	107	108	109	110	111	112	113	114	115	116	117	118	119	120
GCaMP2	V	F	D	K	D	G	N	G	Y	I	S	A	A	E	L	R	H	V	M	T	N	L	G	E	K	L	T	D	E	E
cfGCaMP2	V	F	D	K	D	G	N	G	Y	I	S	A	A	E	L	R	H	V	M	T	N	L	G	E	K	L	T	D	E	E
CEPIA1*er*	V	W	D	K	D	G	N	G	Y	I	S	A	A	D	L	R	H	V	M	T	N	L	G	E	K	L	T	D	E	E
G-GECO1.1	V	F	D	K	D	G	N	G	Y	I	G	A	A	E	L	R	H	V	M	T	N	L	G	E	K	L	T	D	E	E
G-CEPIA1*er*	V	W	D	K	D	G	N	G	Y	I	S	A	A	D	L	R	H	V	M	T	N	L	G	E	K	L	T	D	E	E
R-GECO1	V	F	D	K	D	G	N	G	Y	I	G	A	A	E	L	R	H	V	M	T	D	L	G	E	K	L	T	D	E	E
R-CEPIA1*er*	V	W	D	K	D	G	N	G	Y	I	S	A	A	D	L	R	H	V	M	T	N	L	G	E	K	L	T	D	E	E
GEM-GECO1	V	F	D	K	D	G	N	G	Y	I	G	A	A	E	L	R	H	V	M	T	N	L	G	E	K	L	T	D	E	E
GEM-CEPIA1*er*	V	W	D	K	D	G	N	G	Y	I	G	A	A	E	L	R	H	V	M	T	N	L	G	E	K	L	T	D	E	E

									Ca²⁺ binding Loop IV																			
									+X		+Y		+Z		–Y		–X			–Z									
	121	122	123	124	125	126	127	128	129	130	131	132	133	134	135	136	137	138	139	140	141	142	143	144	145	146	147	148		
GCaMP2	V	D	E	M	I	R	E	A	D	I	D	G	D	G	Q	V	N	Y	E	E	F	V	Q	M	M	T	A	K		
cfGCaMP2	V	D	E	M	I	R	E	A	D	I	D	G	D	G	Q	V	N	Y	E	E	F	V	Q	M	M	T	A	K		
CEPIA1*er*	V	D	E	M	I	R	E	A	D	I	D	G	E	G	Q	V	N	Y	E	E	F	V	Q	M	M	T	A	K		
G-GECO1.1	V	D	E	M	I	R	V	A	D	I	D	G	D	G	Q	V	N	Y	E	E	F	V	Q	M	M	T	A	K		
G-CEPIA1*er*	V	D	E	M	I	R	E	A	D	I	D	G	E	G	Q	V	N	Y	E	E	F	V	Q	M	M	T	A	K		
R-GECO1	V	D	E	M	I	R	V	A	D	I	D	G	D	G	Q	V	N	Y	E	E	F	V	Q	M	M	T	A	K		
R-CEPIA1*er*	V	D	E	M	I	R	E	A	D	I	D	G	E	G	Q	V	N	Y	E	E	F	V	Q	M	M	T	A	K		
GEM-GECO1	V	D	E	M	I	R	V	A	D	I	D	G	D	G	Q	V	N	Y	E	E	F	V	Q	M	M	T	A	K		
GEM-CEPIA1*er*	V	D	E	M	I	R	V	A	D	I	D	G	E	G	Q	V	N	Y	E	D	F	V	Q	M	M	T	A	K		

Figure 3

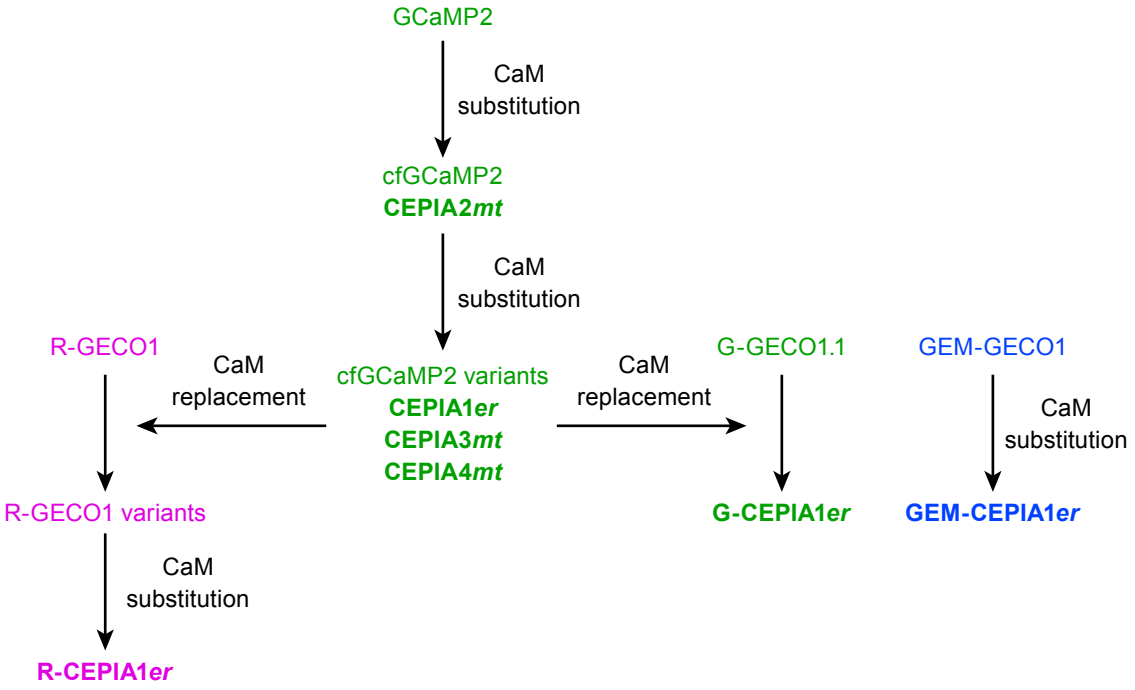
GCaMP2
CaM substitution
cfGCaMP2
CEPIA2mt
CaM substitution
R-GECO1
CaM replacement
cfGCaMP2 variants
CEPIA1er
CEPIA3mt
CEPIA4mt
CaM replacement
G-GECO1.1
GEM-GECO1
CaM substitution
R-GECO1 variants
G-CEPIA1er
GEM-CEPIA1er
CaM substitution
R-CEPIA1er

Figure 4

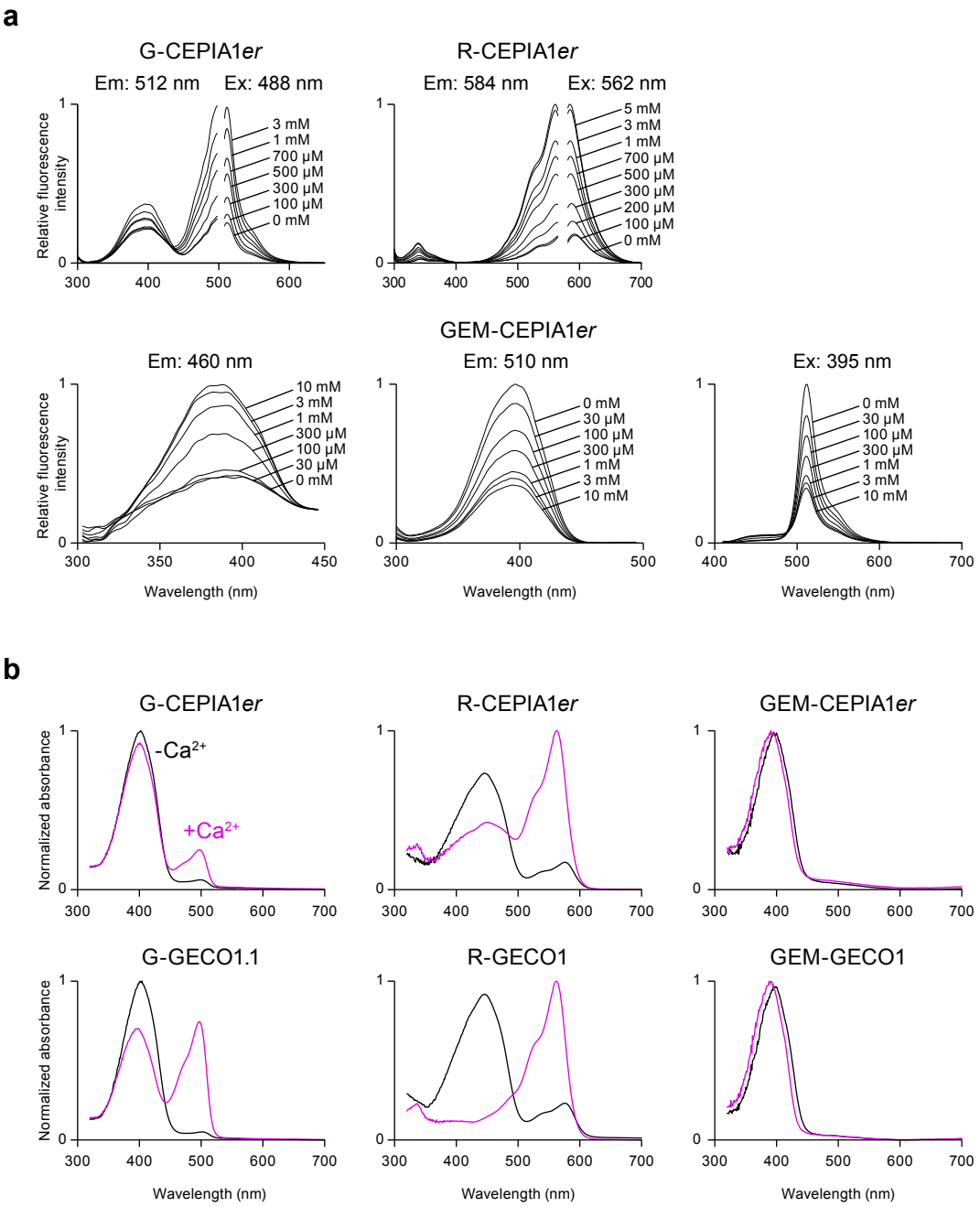
a
G-CEPIA1er
Em: 512 nm Ex: 488 nm
3 mM
1 mM
700 µM
500 µM
300 µM
100 µM
0 mM
R-CEPIA1er
Em: 584 nm Ex: 562 nm
5 mM
3 mM
1 mM
700 µM
500 µM
300 µM
200 µM
100 µM
0 mM
GEM-CEPIA1er
Em: 460 nm
10 mM
3 mM
1 mM
300 µM
100 µM
30 µM
0 mM
Em: 510 nm
0 mM
30 µM
100 µM
300 µM
1 mM
3 mM
10 mM
Ex: 395 nm
0 mM
30 µM
100 µM
300 µM
1 mM
3 mM
10 mM
Relative fluorescence intensity
Wavelength (nm)
b
G-CEPIA1er
R-CEPIA1er
GEM-CEPIA1er
-Ca2+
+Ca2+
G-GECO1.1
R-GECO1
GEM-GECO1
Normalized absorbance
Wavelength (nm)

Figure 5

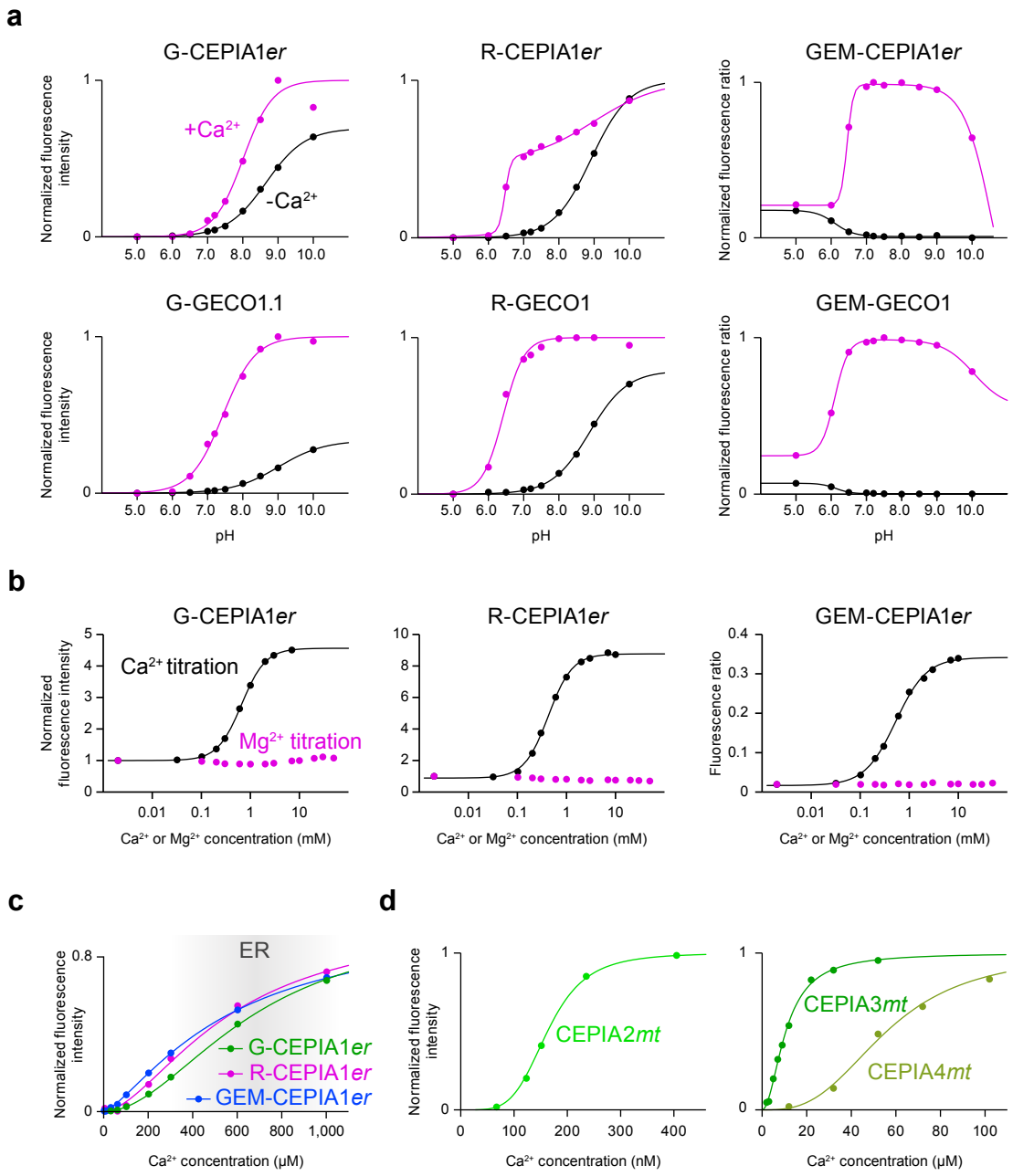
a
G-CEPIA1er
R-CEPIA1er
GEM-CEPIA1er
G-GECO1.1
R-GECO1
GEM-GECO1
Normalized fluorescence intensity
Normalized fluorescence ratio
+Ca2+
-Ca2+
pH
b
Ca2+ titration
Mg2+ titration
Normalized fluorescence intensity
Fluorescence ratio
Ca2+ or Mg2+ concentration (mM)
c
ER
G-CEPIA1er
R-CEPIA1er
GEM-CEPIA1er
Ca2+ concentration (μM)
d
CEPIA2mt
CEPIA3mt
CEPIA4mt
Ca2+ concentration (nM)
Ca2+ concentration (μM)

Figure 6

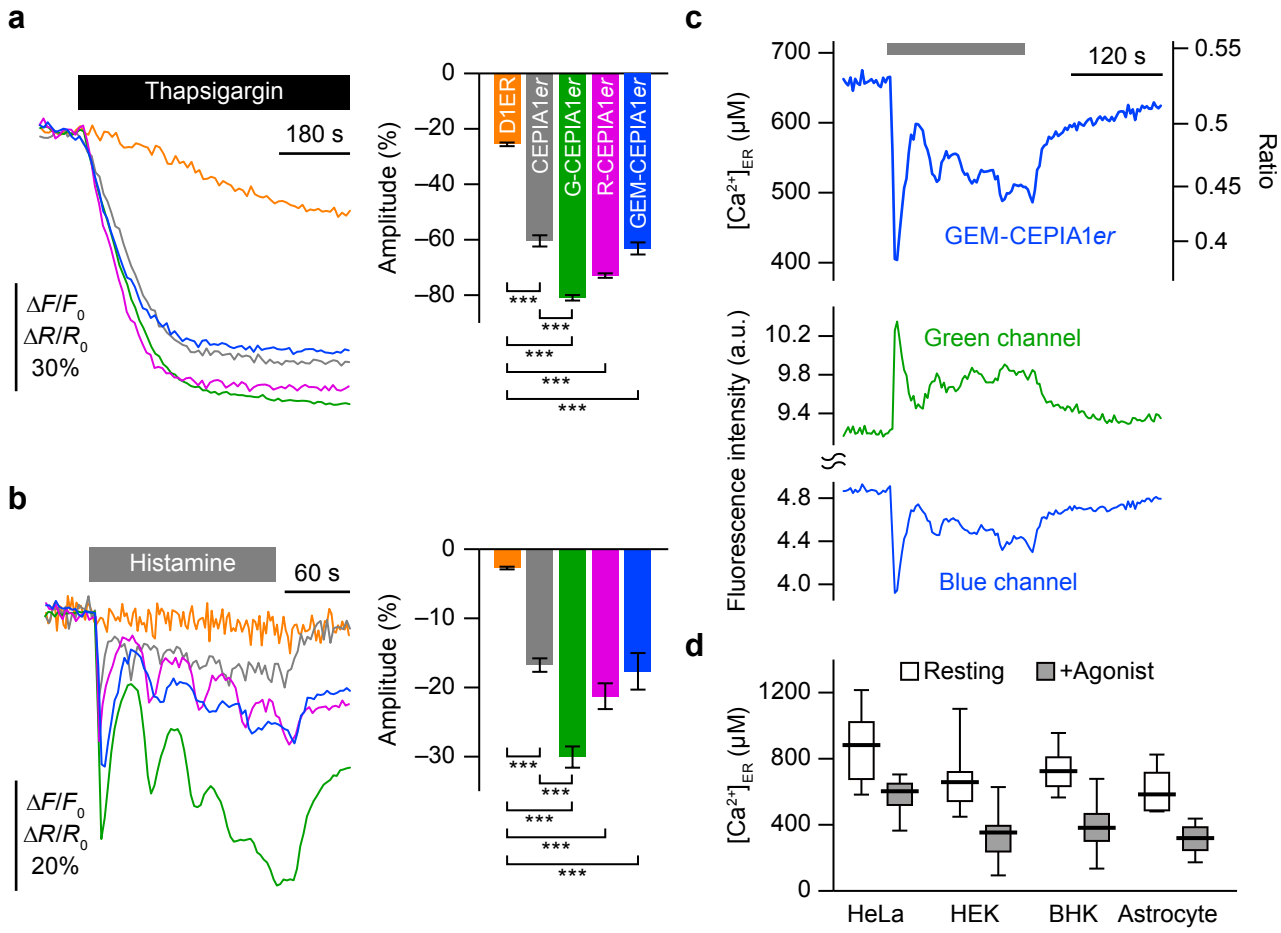
a
Thapsigargin
180 s
ΔF/F0
ΔR/R0
30%
Amplitude (%)
D1ER
CEPIA1er
G-CEPIA1er
R-CEPIA1er
GEM-CEPIA1er
b
Histamine
60 s
ΔF/F0
ΔR/R0
20%
Amplitude (%)
c
120 s
[Ca2+]ER (μM)
GEM-CEPIA1er
Ratio
Fluorescence intensity (a.u.)
Green channel
Blue channel
d
Resting
+Agonist
[Ca2+]ER (μM)
HeLa
HEK
BHK
Astrocyte

Figure 7

a

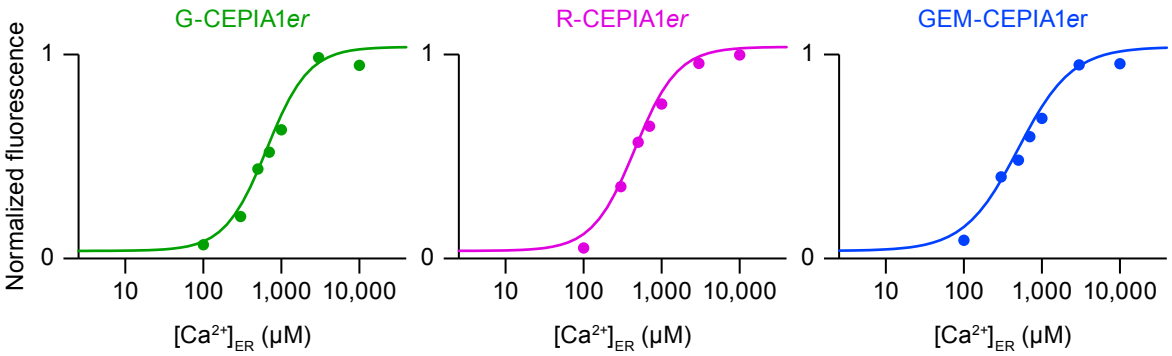

b

	in situ			in vitro		
	Dynamic range	K_d for Ca^{2+} (μM)	Hill coefficient	Dynamic range	K_d for Ca^{2+} (μM)	Hill coefficient
G-CEPIA1*er*	5.1 ± 0.3	650 ± 17	1.62 ± 0.04	4.7 ± 0.3	672 ± 23	1.95 ± 0.07
R-CEPIA1*er*	4.7 ± 0.2	455 ± 10	1.59 ± 0.04	8.8 ± 0.7	565 ± 58	1.70 ± 0.04
GEM-CEPIA1*er*	10.1 ± 1.6	496 ± 11	1.26 ± 0.02	21.7 ± 0.6	558 ± 14	1.37 ± 0.01

Figure 8

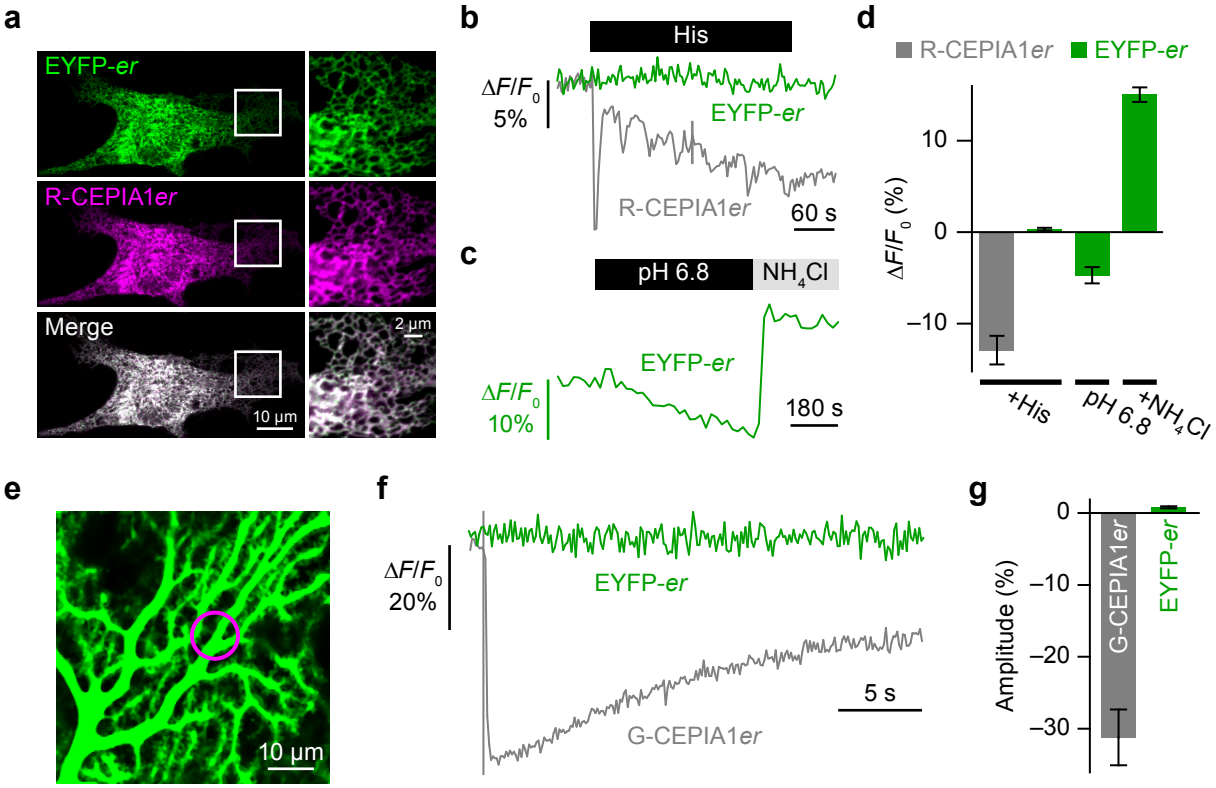
a
EYFP-er
R-CEPIA1er
Merge
10 µm
2 µm
b
His
ΔF/F0
5%
EYFP-er
R-CEPIA1er
60 s
c
pH 6.8
NH4Cl
EYFP-er
ΔF/F0
10%
180 s
d
R-CEPIA1er
EYFP-er
ΔF/F0 (%)
10
0
–10
+His
pH 6.8
+NH4Cl
e
10 µm
f
ΔF/F0
20%
EYFP-er
5 s
G-CEPIA1er
g
Amplitude (%)
0
–10
–20
–30
G-CEPIA1er
EYFP-er

Figure 9

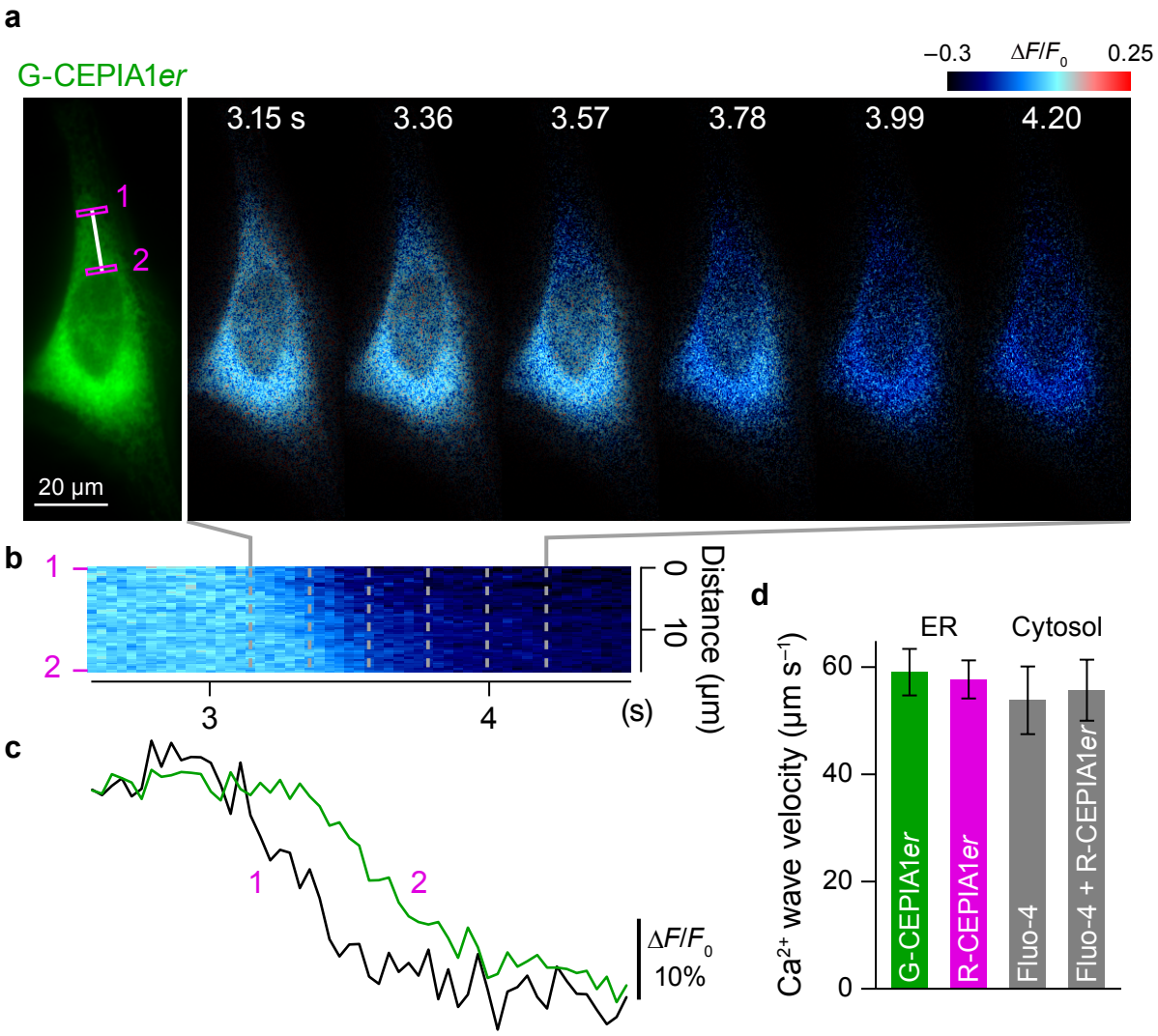
a
G-CEPIA1er
−0.3 ΔF/F0 0.25
3.15 s
3.36
3.57
3.78
3.99
4.20
1
2
20 μm
b
1
2
3
4
(s)
0
10
Distance (μm)
c
1
2
ΔF/F0
10%
d
ER
Cytosol
Ca2+ wave velocity (μm s−1)
60
40
20
0
G-CEPIA1er
R-CEPIA1er
Fluo-4
Fluo-4 + R-CEPIA1er

Figure 10

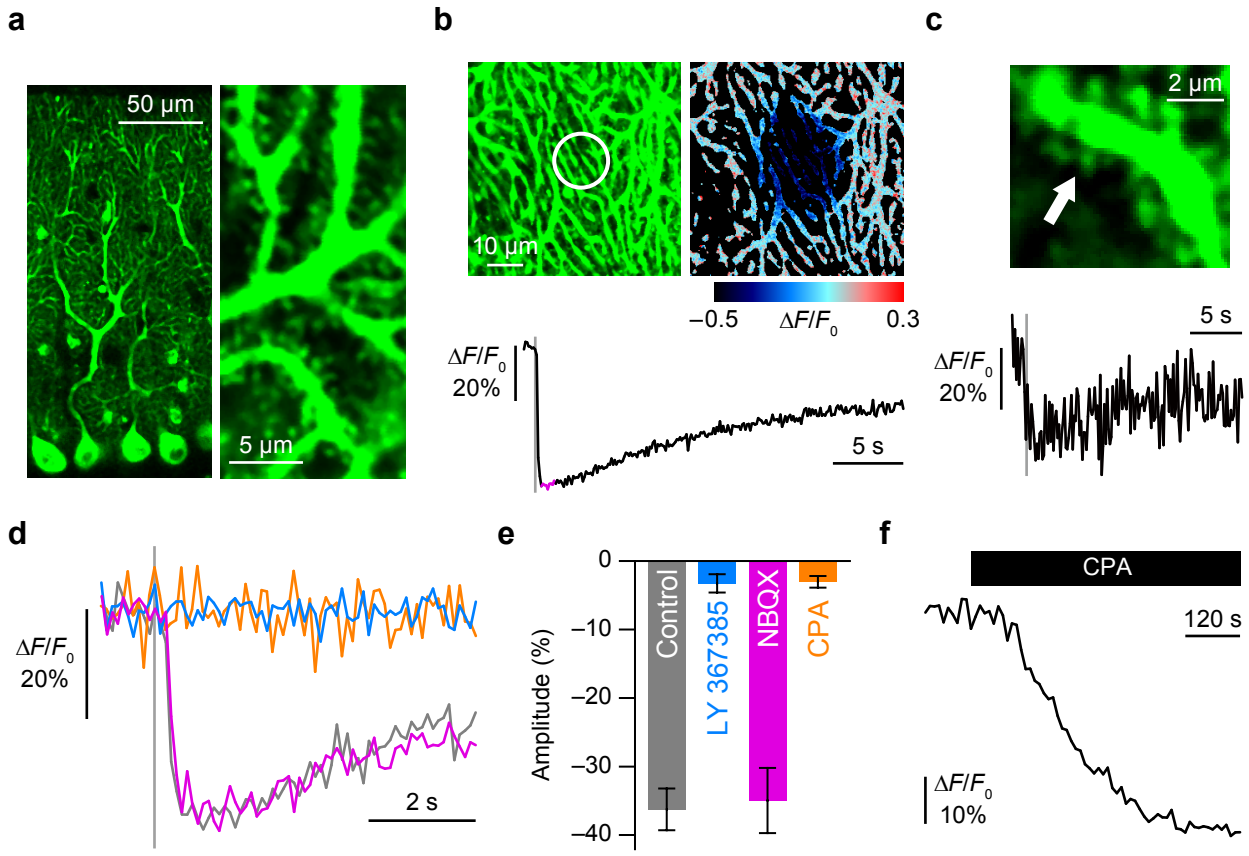
a
50 µm
5 µm
b
10 µm
−0.5
ΔF/F0
0.3
ΔF/F0
20%
5 s
c
2 µm
5 s
ΔF/F0
20%
d
ΔF/F0
20%
2 s
e
0
−10
−20
−30
−40
Amplitude (%)
Control
LY 367385
NBQX
CPA
f
CPA
120 s
ΔF/F0
10%

Figure 11

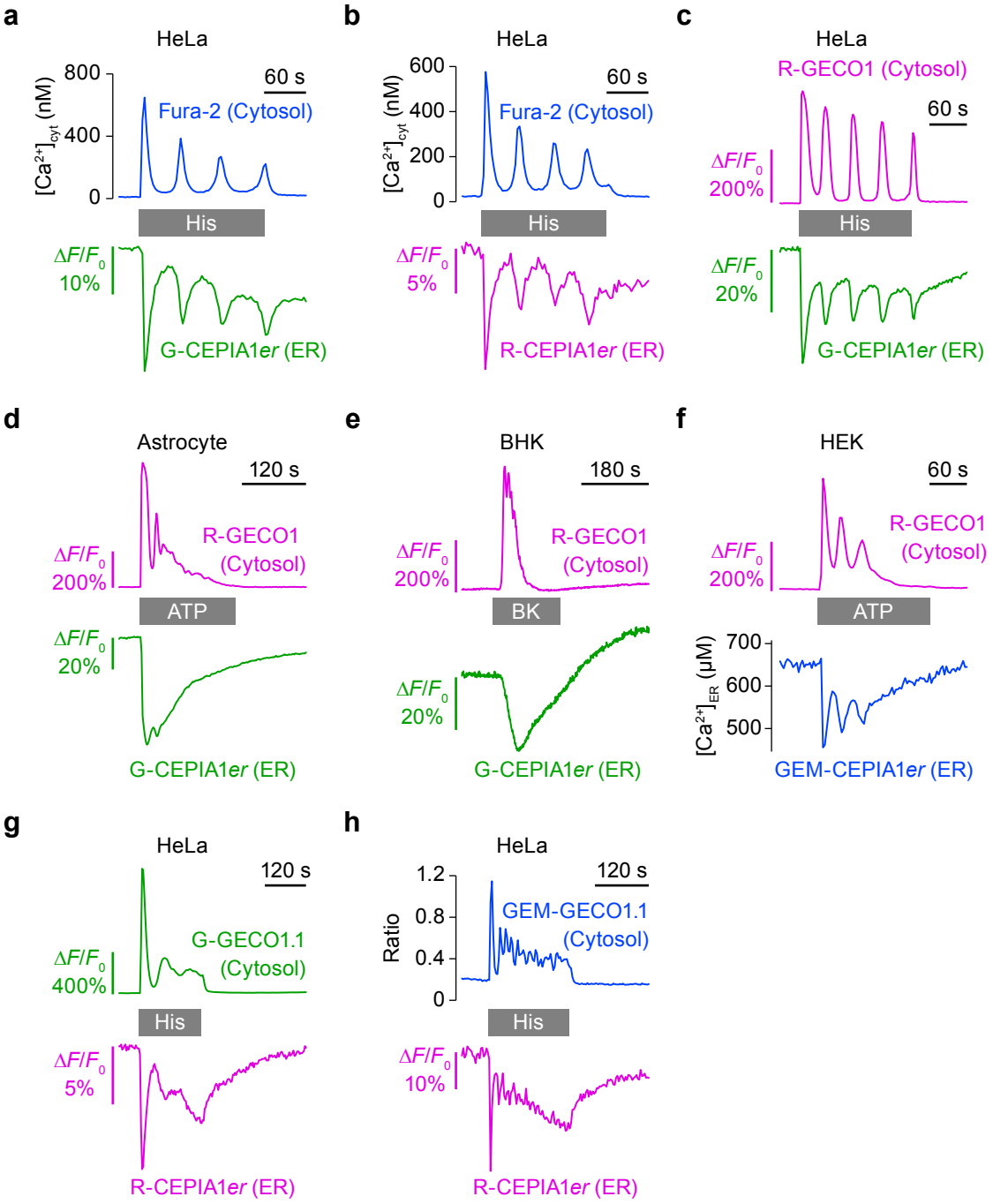
a
HeLa
800
400
0
[Ca2+]cyt (nM)
60 s
Fura-2 (Cytosol)
His
ΔF/F0
10%
G-CEPIA1er (ER)
b
HeLa
600
400
200
0
[Ca2+]cyt (nM)
60 s
Fura-2 (Cytosol)
His
ΔF/F0
5%
R-CEPIA1er (ER)
c
HeLa
R-GECO1 (Cytosol)
60 s
ΔF/F0
200%
His
ΔF/F0
20%
G-CEPIA1er (ER)
d
Astrocyte
120 s
ΔF/F0
200%
R-GECO1
(Cytosol)
ATP
ΔF/F0
20%
G-CEPIA1er (ER)
e
BHK
180 s
ΔF/F0
200%
R-GECO1
(Cytosol)
BK
ΔF/F0
20%
G-CEPIA1er (ER)
f
HEK
60 s
ΔF/F0
200%
R-GECO1
(Cytosol)
ATP
700
600
500
[Ca2+]ER (μM)
GEM-CEPIA1er (ER)
g
HeLa
120 s
ΔF/F0
400%
G-GECO1.1
(Cytosol)
His
ΔF/F0
5%
R-CEPIA1er (ER)
h
HeLa
1.2
0.8
0.4
0
Ratio
120 s
GEM-GECO1.1
(Cytosol)
His
ΔF/F0
10%
R-CEPIA1er (ER)

Figure 12

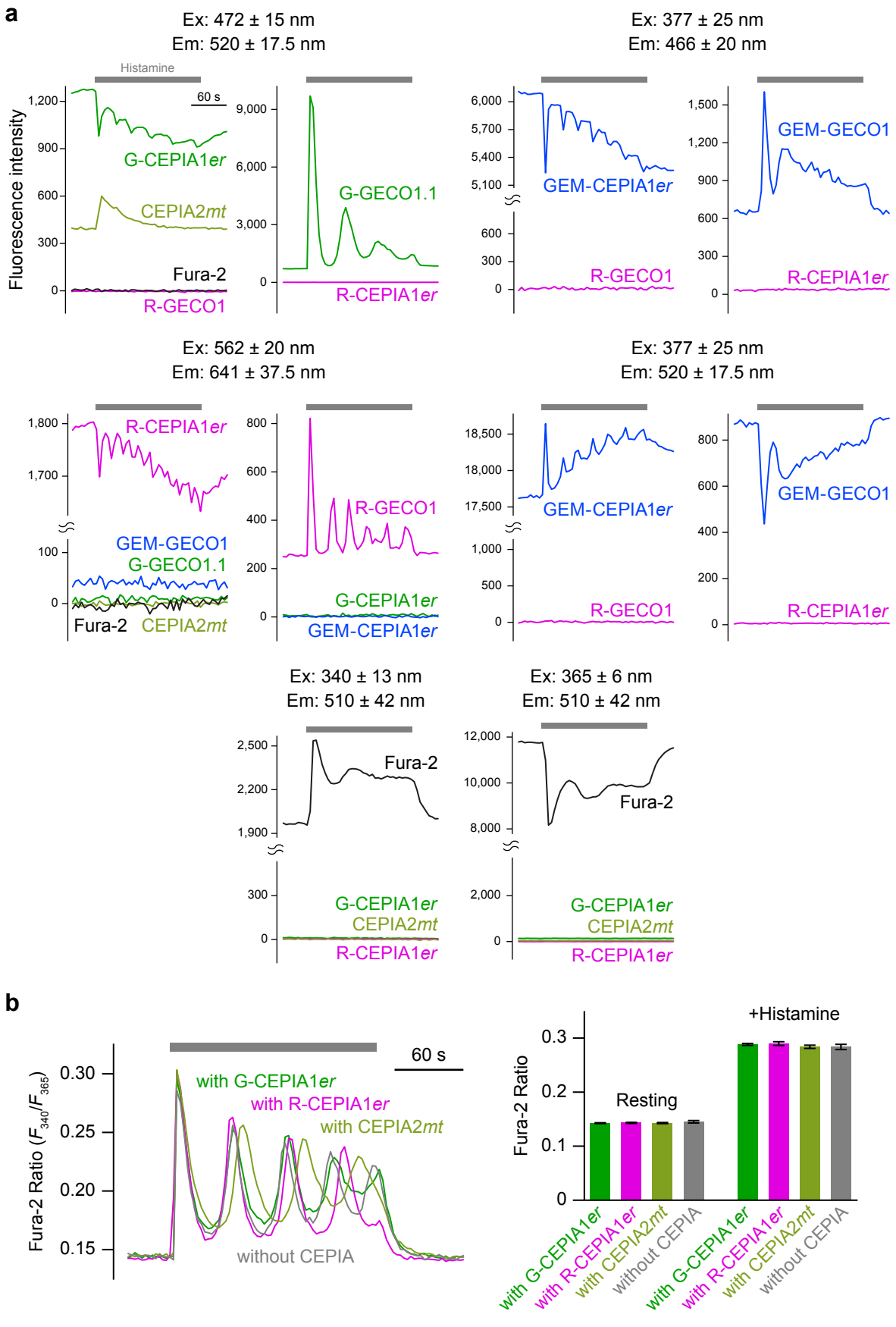
a
Ex: 472 ± 15 nm
Em: 520 ± 17.5 nm
Histamine
60 s
Fluorescence intensity
G-CEPIA1er
CEPIA2mt
Fura-2
R-GECO1
G-GECO1.1
R-CEPIA1er
Ex: 377 ± 25 nm
Em: 466 ± 20 nm
GEM-CEPIA1er
R-GECO1
GEM-GECO1
R-CEPIA1er
Ex: 562 ± 20 nm
Em: 641 ± 37.5 nm
R-CEPIA1er
GEM-GECO1
G-GECO1.1
Fura-2
CEPIA2mt
R-GECO1
G-CEPIA1er
GEM-CEPIA1er
Ex: 377 ± 25 nm
Em: 520 ± 17.5 nm
GEM-CEPIA1er
R-GECO1
GEM-GECO1
R-CEPIA1er
Ex: 340 ± 13 nm
Em: 510 ± 42 nm
Fura-2
G-CEPIA1er
CEPIA2mt
R-CEPIA1er
Ex: 365 ± 6 nm
Em: 510 ± 42 nm
Fura-2
G-CEPIA1er
CEPIA2mt
R-CEPIA1er
b
Fura-2 Ratio (F_{340}/F_{365})
60 s
with G-CEPIA1er
with R-CEPIA1er
with CEPIA2mt
without CEPIA
Fura-2 Ratio
+Histamine
Resting
with G-CEPIA1er
with R-CEPIA1er
with CEPIA2mt
without CEPIA
with G-CEPIA1er
with R-CEPIA1er
with CEPIA2mt
without CEPIA

Figure 13

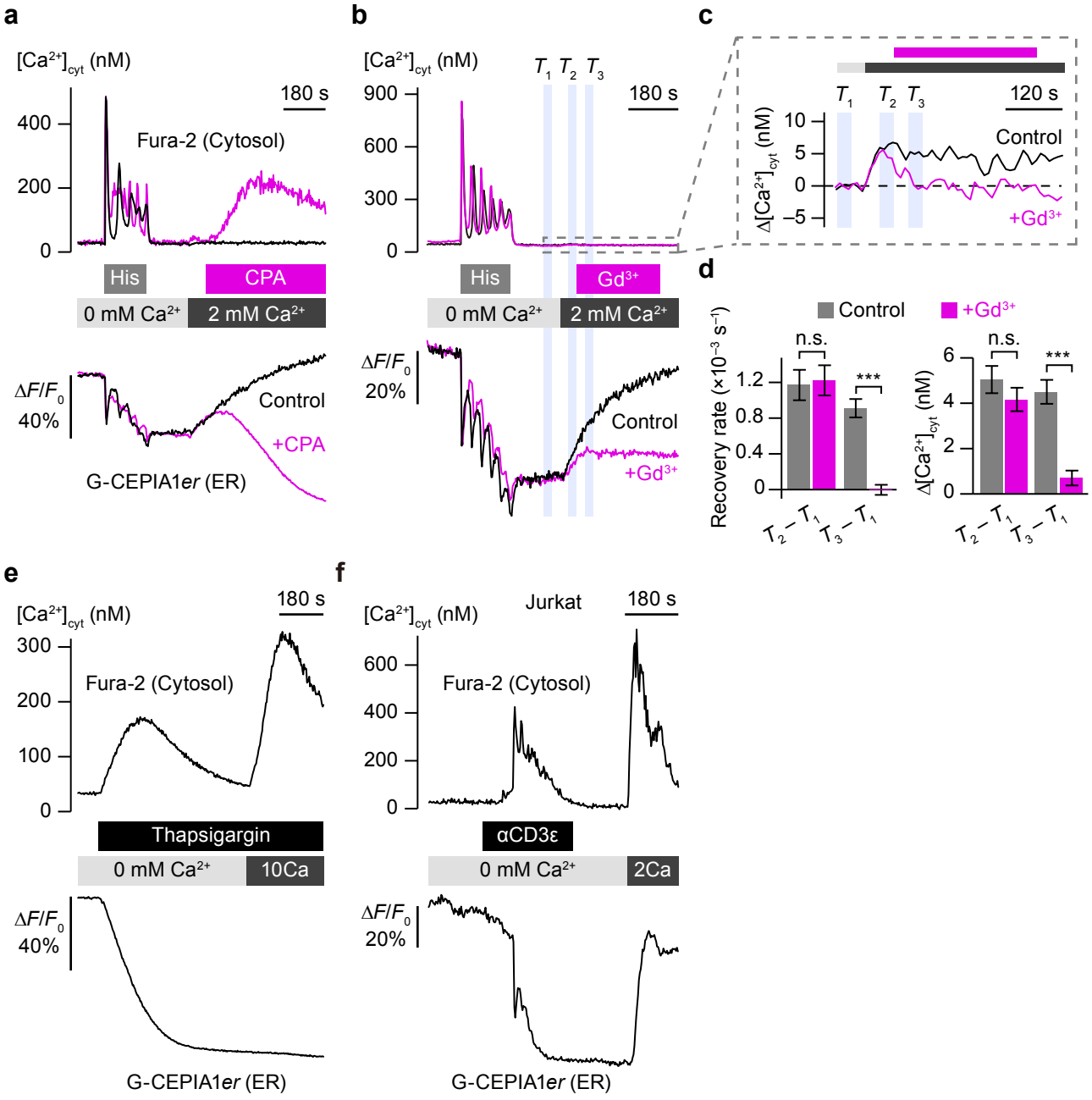
a
[Ca2+]cyt (nM)
180 s
400
200
0
Fura-2 (Cytosol)
His
CPA
0 mM Ca2+
2 mM Ca2+
ΔF/F0
40%
Control
+CPA
G-CEPIA1er (ER)
b
[Ca2+]cyt (nM)
T1 T2 T3
180 s
900
600
300
0
His
Gd3+
0 mM Ca2+
2 mM Ca2+
ΔF/F0
20%
Control
+Gd3+
c
T1 T2 T3
120 s
Δ[Ca2+]cyt (nM)
10
5
0
−5
Control
+Gd3+
d
Control
+Gd3+
Recovery rate (×10−3 s−1)
n.s.
***
1.2
0.8
0.4
0
T2 − T1
T3 − T1
Δ[Ca2+]cyt (nM)
n.s.
***
6
4
2
0
T2 − T1
T3 − T1
e
[Ca2+]cyt (nM)
180 s
300
200
100
0
Fura-2 (Cytosol)
Thapsigargin
0 mM Ca2+
10Ca
ΔF/F0
40%
G-CEPIA1er (ER)
f
[Ca2+]cyt (nM)
Jurkat
180 s
600
400
200
0
Fura-2 (Cytosol)
αCD3ε
0 mM Ca2+
2Ca
ΔF/F0
20%
G-CEPIA1er (ER)

Figure 14

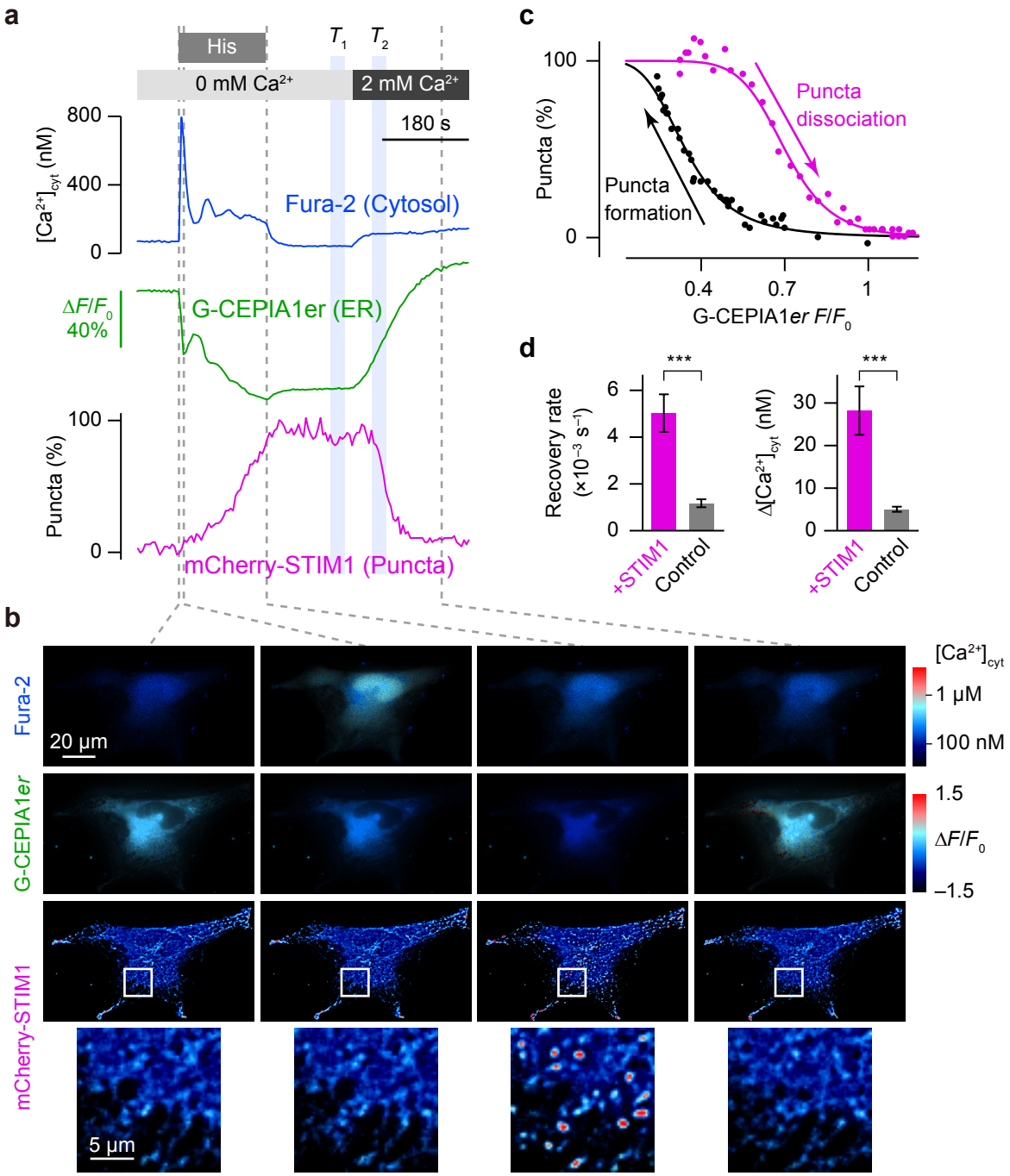
a
His
T_1
T_2
0 mM Ca2+
2 mM Ca2+
180 s
[Ca2+]cyt (nM)
800
400
0
Fura-2 (Cytosol)
ΔF/F0
40%
G-CEPIA1er (ER)
Puncta (%)
100
0
mCherry-STIM1 (Puncta)
c
Puncta (%)
100
0
Puncta dissociation
Puncta formation
0.4
0.7
1
G-CEPIA1er F/F0
d
Recovery rate (×10−3 s−1)
6
4
2
0
***
+STIM1
Control
Δ[Ca2+]cyt (nM)
30
20
10
0
***
+STIM1
Control
b
Fura-2
20 μm
G-CEPIA1er
mCherry-STIM1
5 μm
[Ca2+]cyt
1 μM
100 nM
1.5
ΔF/F0
–1.5

Figure 15

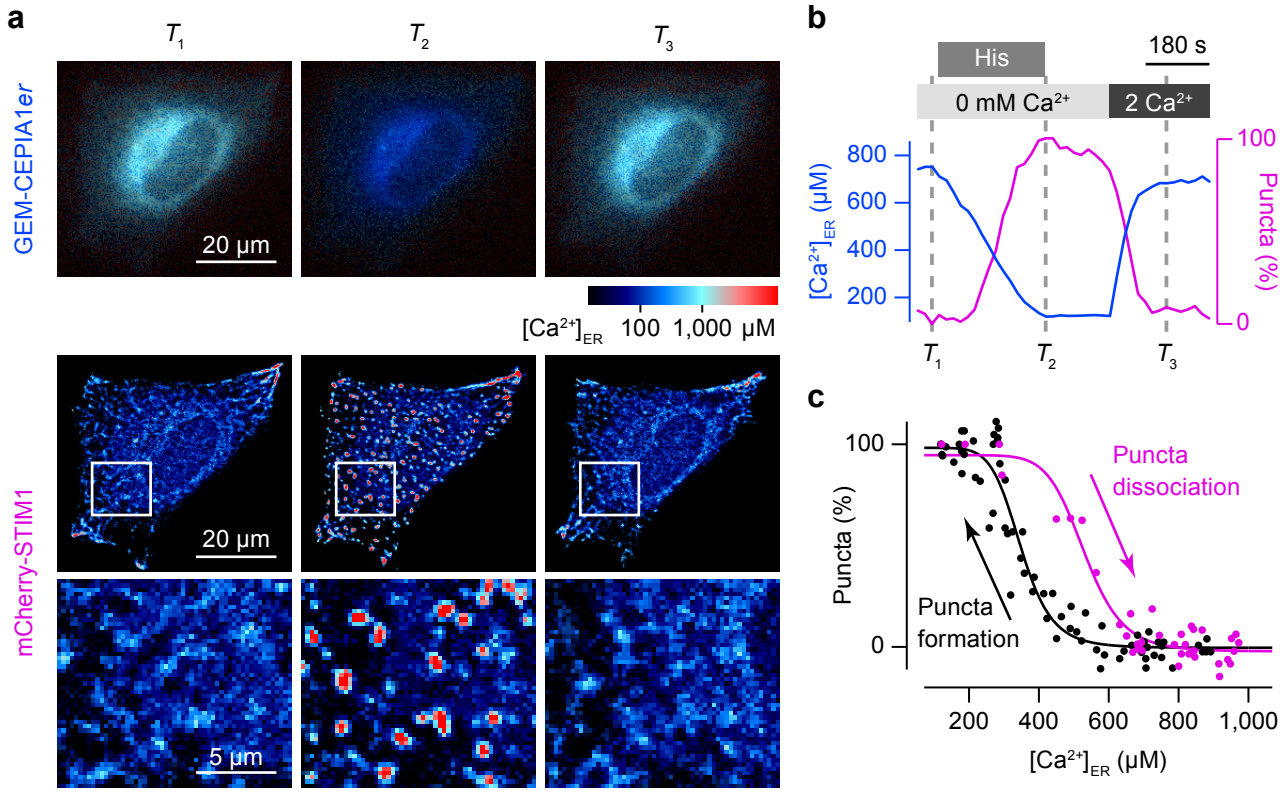
a
T1
T2
T3
GEM-CEPIA1er
20 μm
[Ca2+]ER 100 1,000 μM
mCherry-STIM1
20 μm
5 μm
b
His
180 s
0 mM Ca2+
2 Ca2+
800
600
400
200
[Ca2+]ER (μM)
100
0
Puncta (%)
T1
T2
T3
c
100
0
Puncta (%)
Puncta dissociation
Puncta formation
200
400
600
800
1,000
[Ca2+]ER (μM)

Figure 16

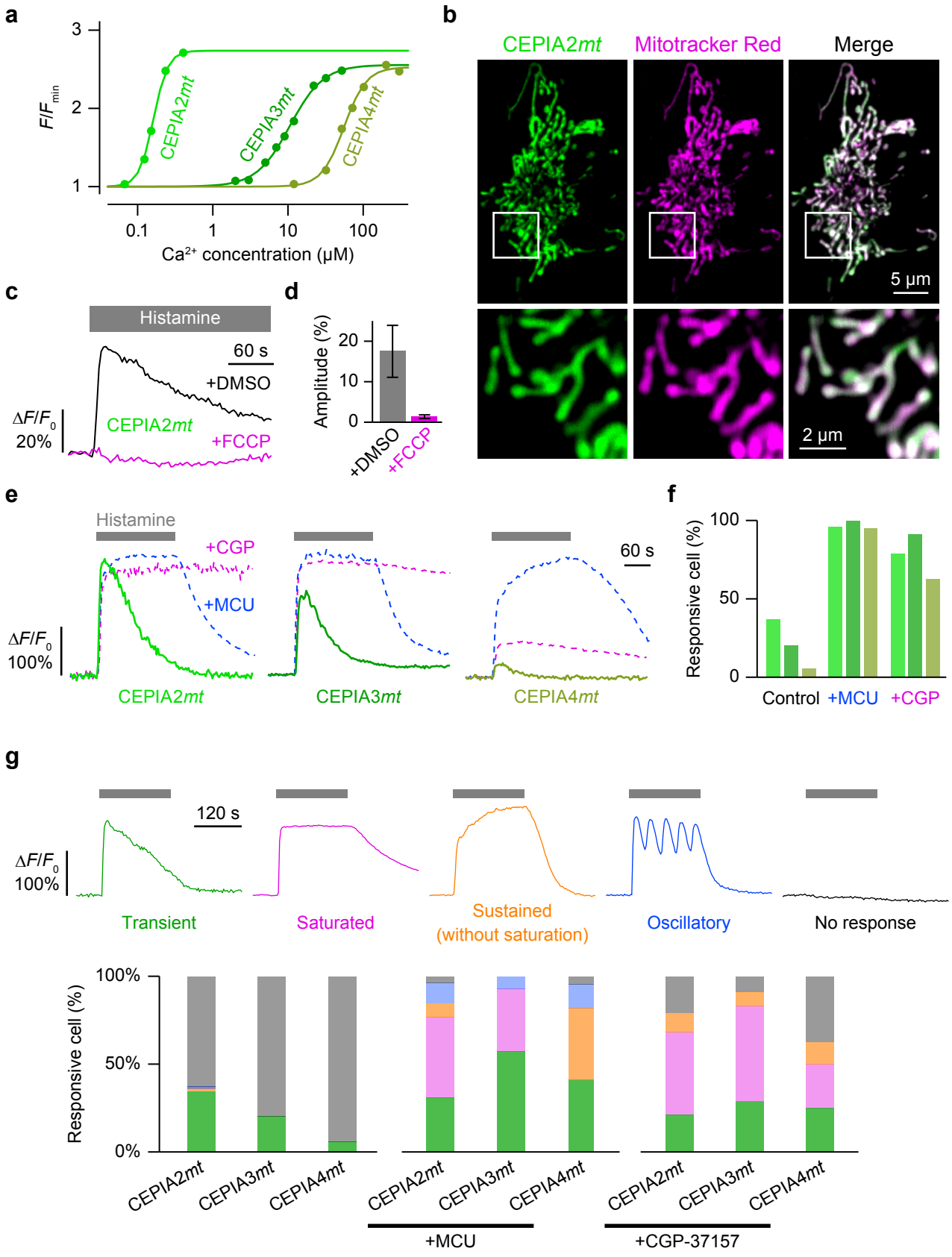
a
F/F_min
3
2
1
CEPIA2mt
CEPIA3mt
CEPIA4mt
0.1
1
10
100
Ca2+ concentration (μM)
b
CEPIA2mt
Mitotracker Red
Merge
5 μm
2 μm
c
Histamine
60 s
+DMSO
ΔF/F0
20%
CEPIA2mt
+FCCP
d
Amplitude (%)
20
10
0
+DMSO
+FCCP
e
Histamine
+CGP
+MCU
60 s
ΔF/F0
100%
CEPIA2mt
CEPIA3mt
CEPIA4mt
f
Responsive cell (%)
100
50
0
Control
+MCU
+CGP
g
120 s
ΔF/F0
100%
Transient
Saturated
Sustained
(without saturation)
Oscillatory
No response
Responsive cell (%)
100%
50%
0%
CEPIA2mt
CEPIA3mt
CEPIA4mt
+MCU
+CGP-37157

Figure 17

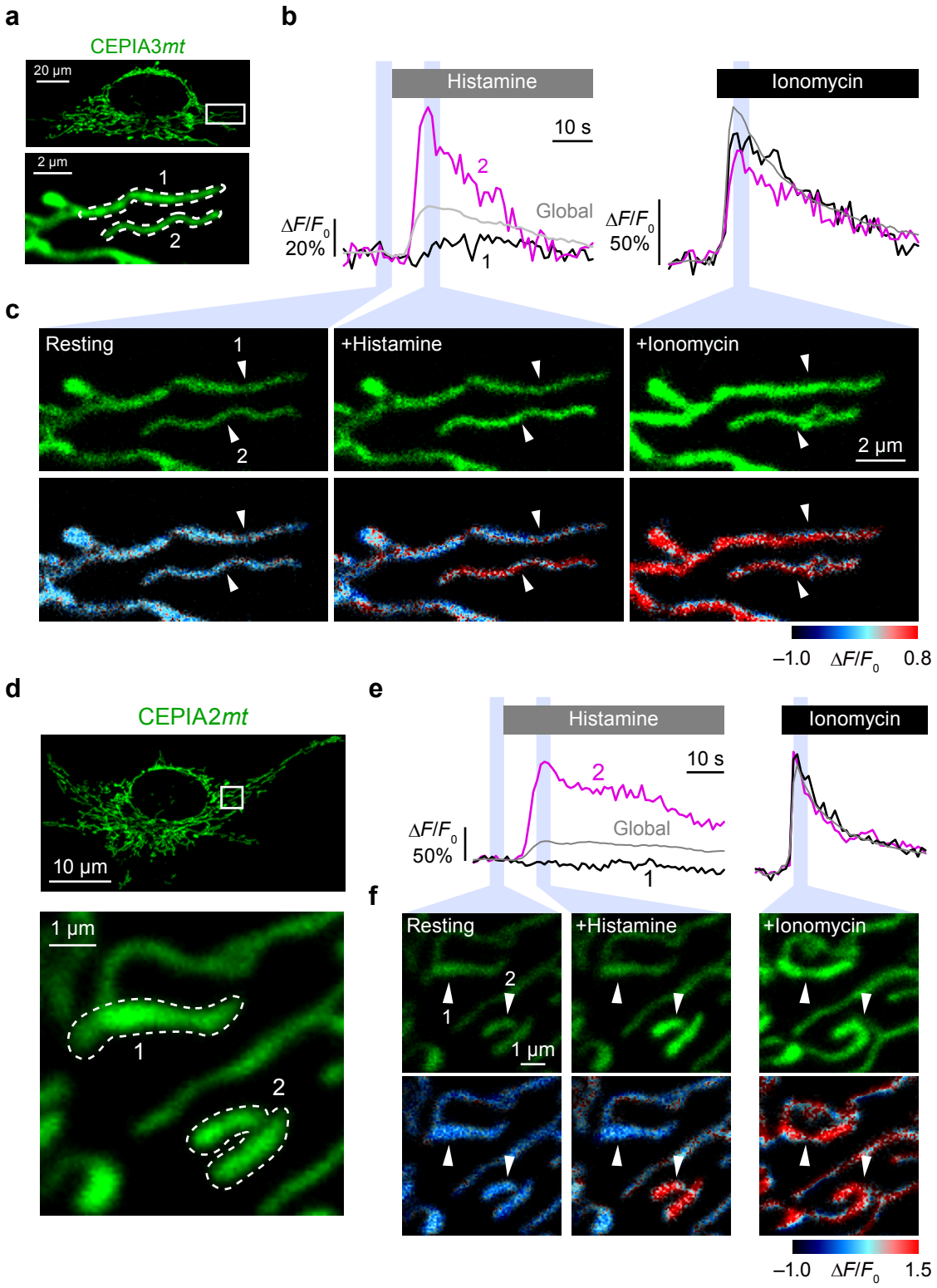
a
CEPIA3mt
20 μm
2 μm
1
2
b
Histamine
Ionomycin
10 s
2
Global
1
ΔF/F0
20%
ΔF/F0
50%
c
Resting
1
2
+Histamine
+Ionomycin
2 μm
–1.0 ΔF/F0 0.8
d
CEPIA2mt
10 μm
1 μm
1
2
e
Histamine
Ionomycin
10 s
2
Global
1
ΔF/F0
50%
f
Resting
+Histamine
+Ionomycin
1
2
1 μm
–1.0 ΔF/F0 1.5

Figure 18

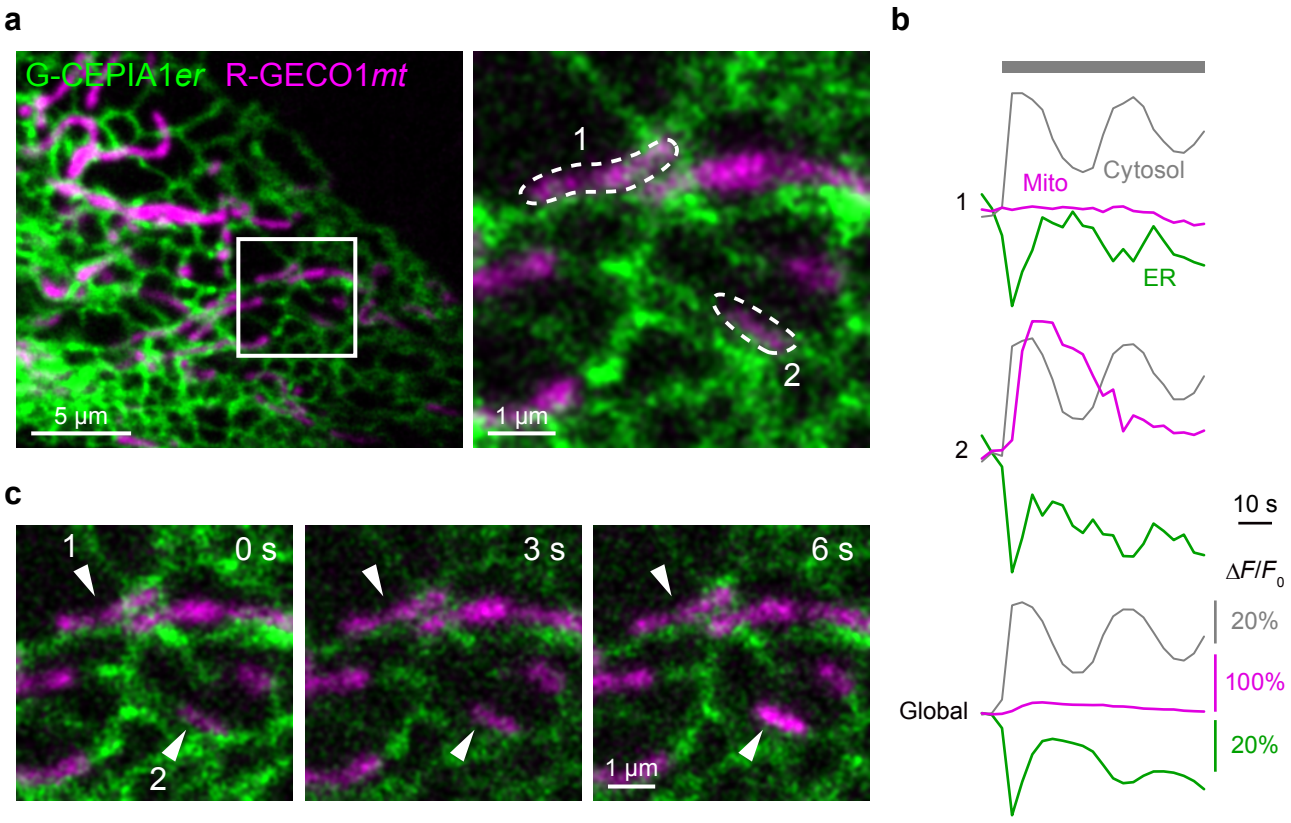
a
G-CEPIA1er R-GECO1mt
5 µm
1
2
1 µm
b
Mito
Cytosol
ER
1
2
10 s
ΔF/F0
20%
100%
20%
Global
c
1
0 s
2
3 s
6 s
1 µm

Figure 19

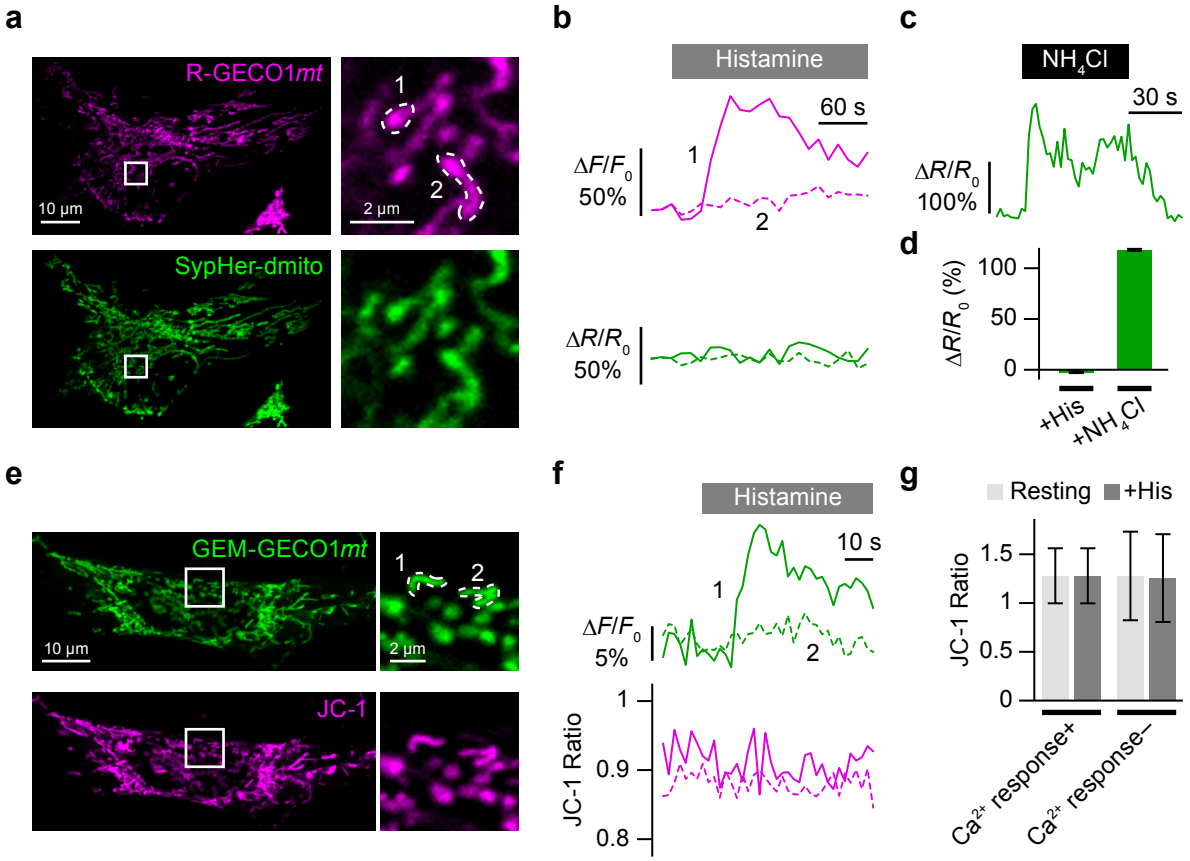
a
R-GECO1mt
10 µm
1
2
2 µm
SypHer-dmito
b
Histamine
60 s
ΔF/F0
50%
1
2
ΔR/R0
50%
c
NH4Cl
30 s
ΔR/R0
100%
d
ΔR/R0 (%)
100
50
0
+His
+NH4Cl
e
GEM-GECO1mt
10 µm
1
2
2 µm
JC-1
f
Histamine
10 s
ΔF/F0
5%
1
2
JC-1 Ratio
1
0.9
0.8
g
Resting
+His
JC-1 Ratio
1.5
1
0.5
0
Ca2+ response+
Ca2+ response–

Figure 20